Argonne
NATIONAL LABORATORY

ANL-MCS-CPH-06/56

Heights Integrated Model as Instrument for Simulation of Hydrodynamic, Radiation Transport, and Heat Conduction Phenomena of Laser-Produced Plasma in EUV Applications

Mathematics and Computer Science Division

About Argonne National Laboratory

Argonne is a U.S. Department of Energy laboratory managed by UChicago Argonne, LLC under contract DE-AC02-06CH11357. The Laboratory's main facility is outside Chicago, at 9700 South Cass Avenue, Argonne, Illinois 60439. For information about Argonne, see www.anl.gov.

Availability of This Report

This report is available, at no cost, at http://www.osti.gov/bridge. It is also available on paper to the U.S. Department of Energy and its contractors, for a processing fee, from:

U.S. Department of Energy
Office of Scientific and Technical Information
P.O. Box 62
Oak Ridge, TN 37831-0062
phone (865) 576-8401
fax (865) 576-5728
reports@adonis.osti.gov

ANL-MCS-CPH-06/56

Heights Integrated Model as Instrument for Simulation of Hydrodynamic, Radiation Transport, and Heat Conduction Phenomena of Laser-Produced Plasma in EUV Applications

by
V. Sizyuk, A. Hassanein, V. Morozov, and T. Sizyuk
Mathematics and Computer Science Division, Argonne National Laboratory

November 2006

List of Acronyms

3D	Three dimensional
CE	Coefficient efficiency
DOF	Depth of focus
DRT	Direct radiation transport
DPP	Discharge produced plasma
ENO	Essentially Non Oscillatory
EUV	Extreme ultraviolet
IC	Integrated circuit
LPP	Laser-produced plasma
MCRT	Monte Carlo radiation transport
MHD	Magnetohydrodynamics
RTE	Radiation transport equation
TVD-LF	Total variation diminishing in Lax-Friedrich formulation

CONTENTS

Figures

Tables

Heights Integrated Model as Instrument for Simulation of Hydrodynamic, Radiation Transport, and Heat Conduction Phenomena of Laser-Produced Plasma in EUV Applications

V. Sizyuk, A. Hassanein, V. Morozov, and T. Sizyuk

Abstract

The HEIGHTS integrated model has been developed as an instrument for simulation and optimization of laser-produced plasma (LPP) sources relevant to extreme ultraviolet (EUV) lithography. The model combines three general parts: hydrodynamics, radiation transport, and heat conduction. The first part employs a total variation diminishing scheme in the Lax-Friedrich formulation (TVD-LF); the second part, a Monte Carlo model; and the third part, implicit schemes with sparse matrix technology. All model parts consider physical processes in three-dimensional geometry. The influence of a generated magnetic field on laser plasma behavior was estimated, and it was found that this effect could be neglected for laser intensities relevant to EUV (up to ~10^{12} W/cm^2). All applied schemes were tested on analytical problems separately. Benchmark modeling of the full EUV source problem with a planar tin target showed good correspondence with experimental and theoretical data. Preliminary results are presented for tin droplet- and planar-target LPP devices. The influence of three-dimensional effects on EUV properties of source is discussed.

Introduction

Ever since the invention of the transistor in 1947 and the integrated circuit (IC) in the late 1950s, semiconductor technology has undergone rapid advances. From a basic technical point of view, developments have been straightforward. They have mainly involved putting more and smaller transistors on integrated circuits. More transistors allow increased functionality, and smaller size allows increased switching speed and less power consumption for each transistor. The whole process has conformed to Moore's law, formulated by Gordon Moore in 1965 [1].

Moore stated that the number of components per IC roughly doubles every second year. In recent decades, the single most important driver of Moore's law has been the inventions of microlithography. This lithographic process generates a semiconductor wafer partially covered with photoresist so that the uncovered regions are available for different kinds of processing, such as etching, ion implantation, or metallization. One of the most important lithographic processes is exposure, when light shines on select parts of the resist and microelectronic elements are formed [2]. Resolution of an optical system, such as projection-lithography system, is traditionally determined by the Rayleigh criterion,

$$Resolution = 0.61\frac{\lambda}{NA}, \tag{1}$$

where λ is the wavelength of the light and NA is the numerical aperture of the optical system ($NA = \sin\theta_{\max}$ for vacuum). However, the Rayleigh criterion treats the ability to resolve two point sources and not the printability of semiconductor structures. In this case, the object size is

$$Object\ size = k\frac{\lambda}{NA}, \tag{2}$$

where the "*k*-factor" is introduced [2]. According to Eq. (2) minimal component size can be achieved by increasing the numerical aperture or decreasing the wavelength or *k*-factor. Until about 1993-1994, k was stable at 0.8; it has since been decreased to almost 0.4 by using binary masks [3]. As illustrated in Table 1, there has been a continuous increase in *NA* and decrease in wavelength over the years.

Table 1. Progress with lithography instruments [2]

Wavelength, nm	*NA*	Year	Light Source
436	0.30	1982	Hg arc lamp (g-line)
365	0.45	1990	Hg arc lamp (i-line)
365	0.60	1994	Hg arc lamp (i-line)
248	0.50	1994	Hg arc lamp or KrF eximer laser
248	0.60	1997	KrF eximer laser
248	0.70	1999	KrF eximer laser
193	0.60	1999	ArF eximer laser
193	0.75	2001	ArF eximer laser

Increasing the *NA* causes problems with the depth of focus (DOF), as illustrated in Fig. 1. The DOF should be larger than the photoresist coating thickness for optimal performance. Alignment difficulties arise when the distance over which the image is sharp is only slightly larger than the resist thickness. Several ways exist for further improvement in semiconductor technology. The two most important are utilizing the smallest wavelength available with projection lithography and utilizing ion- and electron-beam lithography. Figure 2 shows present-day limitations on line thickness as a function of used radiation wavelength. Both ion- and electron-beam projection have the inherent drawback that they cannot fulfill resolution and throughput demands at the same time, because of the repelling nature of similarly charged particles. Application of noncharged photons has no such limitation. Use of extreme ultraviolet light (wavelength between 10 and 15 nm) is a promising solution for this reason.

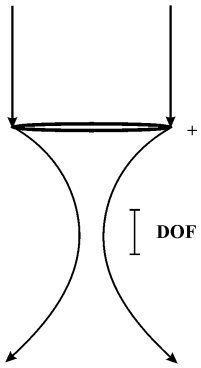

Fig. 1. Schematic of depth of focus (defined as the distance over which the focus is smallest).

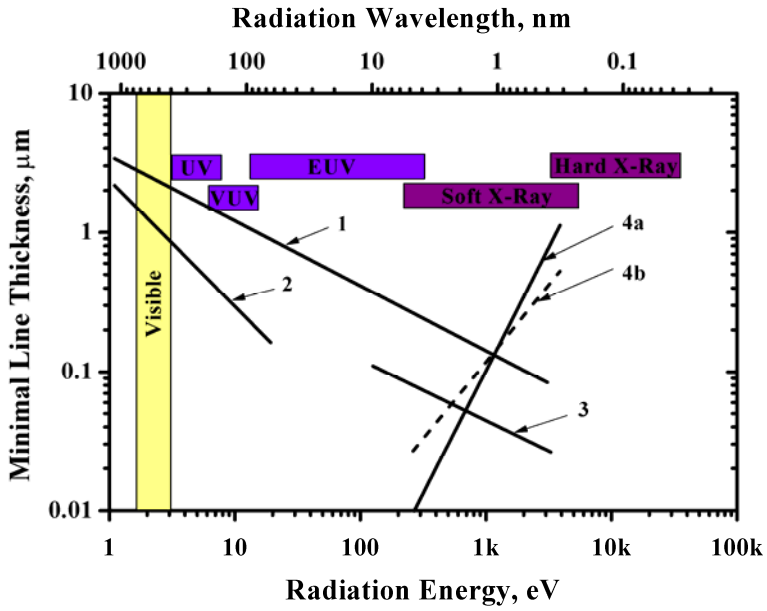

Fig. 2. Minimal reproducible line thickness: 1 – diffraction limit for proximity lithography with gap of 10 μm; 2 – diffraction limit for projection lithography for NA = 0.4; 3 – diffraction limit for proximity lithography with gap of 1 μm; 4a and 4b - photoelectron scattering limit for electron-beam lithography (theory and experiment, respectively).

EUV light is absorbed very strongly in most materials, including gases; thus, all optics and the source should be placed into a vacuum. For the same reason lenses cannot be used: optical systems should consist of mirrors. Because reflection of a single surface is very low (about 4%), stacked multilayers are used, for which the reflection adds up. The EUV light can be generated in several methods: discharge produced plasma (DPP), laser produced plasma (LPP), or synchrotron radiation. Each method has benefits and problems. In order to meet the requirements of the Intel Lithography Roadmap goals for high-volume manufacturing [4] and International SEMATECH's EUV Source Program goal [5], the EUV source is required to have a power of 80-120 W at a wavelength of 13.5 nm (2% bandwidth). Various LPP and DPP devices are under investigation by different research groups. At present, several of the EUV sources come close to the power level demanded by commercial chip manufacturers. The coefficient of efficiency (CE) of generating EUV radiation is the key factor in successful development of the source. Many additional factors are important to the EUV device efficiency: plasma material, form and size of the radiated area, collectable solid angle, debris amount, etc. Because many physical processes are involved and many technical problems need to be solved when optimizing

a particular EUV device, a laboratory experiment would be very expensive, and only computer modeling can generate a complete picture within a reasonable time and at a reasonable cost. Ideally, an integrated physical model should be developed specifically for simulating plasma behavior in DPP and LPP devices. The model should include the atomic physics, hydrodynamics, radiation transport, heat conduction and EUV analysis. The EUV source should be modeled completely: from the energy input mechanism and plasma formation, to EUV output from the pinch or laser target and the collector system reflection. Each physical process should be described adequately, and each physical problem should be solved by the most advanced numerical scheme. The intermediate focus of a manufacturer's EUVL stepper can be predicted in that case most correctly.

This report describes a three-dimensional integrated model, called HEIGHTS, for modeling of LPP devices. The model is based on previous work in simulating of DPP devices by the HEIGHTS team [6-8]. This report describes the general model construction, derivation of initial equations, development of numerical schemes, organization of computer code, results from test samples, and parallel version implementation. The influence of a generated magnetic field is discussed. Results of modeling are presented for a spherical tin target and a three-laser-beam assembly.

1. General Laws of Plasma Motion

To construct a flexible integrated physical model, one must to minimize (as much as possible) the number of general laws, develop a hierarchy of physical processes, and construct a simple mechanism for the incorporation of new processes. For this reason, the HEGHTS model was created from first principles and does not include final results from other projects. The conservation law of any parameter q can be given in differential form:

$$\frac{\partial q}{\partial t} + \nabla \cdot \mathbf{F}_q = 0, \qquad (1.1)$$

where $\mathbf{F}_q$ is the flux of this parameter. By considering plasma matter as a continuous, compressible medium, we expanded Eq. (1.1) and obtained the following expressions for conservation of mass, pulse, and total energy:

$$\begin{aligned} &\frac{\partial \rho}{\partial t} + \nabla \cdot (\rho \mathbf{v}) = 0, \\ &\frac{\partial}{\partial t} \rho \mathbf{v} + \nabla \cdot (\rho \mathbf{v}\mathbf{v} + p_h) = 0, \\ &\frac{\partial e_h}{\partial t} + \nabla \cdot [\mathbf{v}(e_h + p_h)] = 0, \end{aligned} \qquad (1.2)$$

where,

ρ - density of plasma,

$\mathbf{v}$ - velocity of plasma,

p_h - hydrodynamic pressure, and

$e_h = \frac{\rho v^2}{2} + e_{\text{int}}$ - sum of kinetic and internal energy densities of plasma.

The equation set (1.2) describes convective motion of a compressible homogeneous medium. Later, this basic set will be expanded to consider the plasma as a mixture of electron and ion gases. Additional external forces and sources will be added, and dissipative terms will be taken into account. All physical expressions and all transformation use Gaussian units, unless stated otherwise.

In laboratory plasma experiments, any electromagnetic sources can have an external influence on the plasma, and electric currents can be generated spontaneously by intensive heating of local plasma areas. Any current can be the source of a magnetic field in the plasma, and this magnetic field is the source of forces that disturb the initial plasma. This self-consistent process should be included in the hydrodynamic equation set (1.2). Moreover, the conservative form of the set should not be changed. For this reason, it is appropriate to introduce an additional conservative variable: magnetic field **B**. An additional equation for the introduced variable should be written and the corresponding forces added into the equation set (1.2). The HEIGHTS general equation set does not operate with currents directly because of the conservative form of the initial equation. Any external force $\mathbf{F}_{ex}$ can be added into (1.2) as follows:

$$\frac{\partial \rho}{\partial t} + \nabla \cdot (\rho \mathbf{v}) = 0,$$
$$\frac{\partial}{\partial t} \rho \mathbf{v} + \nabla \cdot (\rho \mathbf{v}\mathbf{v} + p_h) = \mathbf{F}_{ex}, \tag{1.3}$$
$$\frac{\partial e_h}{\partial t} + \nabla \cdot [\mathbf{v}(e_h + p_h)] = \mathbf{v} \cdot \mathbf{F}_{ex}.$$

In the general case of magnetic hydrodynamics, external forces can be expressed as forces that act on the unit charge, such as force field strength $\mathbf{E}$. It may be given as the sum of three forces: Lorenz, electrical field, and Hall force:

$$\mathbf{E} = -\frac{1}{c} \mathbf{v} \times \mathbf{B} + \eta \mathbf{j} + \frac{h_c}{\rho} \mathbf{j} \times \mathbf{B}. \tag{1.4}$$

To simplify the equation transformation, we can rewrite the vector form of (1.3) to the component tensor form in the Cartesian coordinate system. Covariant and contravariant components of the tensor are equivalent in the orthonormalized Cartesian system. We can speak here about matrices and not about tensors because there is no difference between superscripts and subscripts. However, we use the tensor technique of summations for this case. At the end of the transformations, the results will be generalized to the tensor case in the arbitrary coordinate system. Then, we specially use subscripts for all terms to emphasize the particular case. Use of tensor calculus makes the governing equations more flexible for practical applications.

1.1. Continuity Equation

The mass conservation equation keeps its form in the magnetohydrodynamics (MHD) case

$$\frac{\partial \rho}{\partial t} + \frac{\partial}{\partial x_k} (\rho v_k) = 0. \tag{1.1.1}$$

Here and elsewhere we have in mind summation by repeating index.

1.2. Equation of Motion

Only the Lorenz force is taken into account by transformations of the equation of motion. This is possible to do with the local electrical neutrality approximation. Electrons and ions can have different energy (temperature), but the total charge of the plasma in the calculating cell we can assume as zero. In that way, $\mathbf{F}_{ex} = \frac{q}{c}\mathbf{v}\times\mathbf{B}$ => $\mathbf{F}_{ex} = \frac{1}{c}\mathbf{j}\times\mathbf{B}$. By using Ampere's law,

$$\mathrm{rot}\mathbf{B} = \frac{\mu}{c}\left(4\pi\mathbf{j} + \frac{\partial\mathbf{D}}{\partial t}\right). \tag{1.2.1}$$

Neglecting the displacement current $\frac{\partial\mathbf{D}}{\partial t}$, we can write the initial equation of motion for the system (1.3) for the MHD case in vector form:

$$\frac{\partial}{\partial t}\rho\mathbf{v} + \nabla\left(\rho\mathbf{v}\mathbf{v} + p_h\right) - \frac{1}{4\pi\mu}(\nabla\times\mathbf{B})\times\mathbf{B} = 0. \tag{1.2.2a}$$

In tensor form, it is

$$\frac{\partial}{\partial t}\rho v_i + \frac{\partial}{\partial x_k}\left(\rho v_i v_k + p_h\delta_{ik}\right) - \frac{1}{4\pi\mu}\varepsilon_{ijk}\left(\varepsilon_{jpn}\frac{\partial B_n}{\partial x_p}\right)B_k = 0. \tag{1.2.2b}$$

We transform the additional magnetic term:

$$\varepsilon_{ijk}\varepsilon_{jpn}\frac{\partial B_n}{\partial x_p}B_k = \varepsilon_{jki}\varepsilon_{jpn}\frac{\partial B_n}{\partial x_p}B_k = \left(\delta_{kp}\delta_{in} - \delta_{kn}\delta_{ip}\right)\frac{\partial B_n}{\partial x_p}B_k = \delta_{kp}\delta_{in}\frac{\partial B_n}{\partial x_p}B_k - \delta_{kn}\delta_{ip}\frac{\partial B_n}{\partial x_p}B_k =$$

$$= \frac{\partial B_i}{\partial x_k}B_k - \delta_{ik}\frac{\partial}{\partial x_k}\left(\frac{B^2}{2}\right) = \frac{\partial\left(B_i B_k\right)}{\partial x_k} - B_i\frac{\partial B_k}{\partial x_k} - \delta_{ik}\frac{\partial}{\partial x_k}\left(\frac{B^2}{2}\right).$$

We can write the equation of motion as

$$\frac{\partial}{\partial t}\rho v_i + \frac{\partial}{\partial x_k}\left(\rho v_i v_k\right) + \frac{\partial}{\partial x_k}\left(p_h \delta_{ik} + \frac{B^2 \delta_{ik}}{8\pi\mu} \right) - \frac{1}{4\pi\mu}\left(\frac{\partial\left(B_k B_i\right)}{\partial x_k} \right) = -\frac{1}{4\pi\mu} B_i \frac{\partial B_k}{\partial x_k}. \quad (1.2.3)$$

The term on the right side of Eq. (1.2.3) is the divergence of magnetic field $\mathbf{B}$. In analytical formulations, this term is equal to zero. However, the divergence $\mathbf{B}$ is not equal to zero in numerical calculations because of truncation errors. In modern numerical schemes [9,10], this term is used to correct the solution and to stabilize the divergence $\mathbf{B}$ near zero. The effect of nonzero $\nabla \cdot \mathbf{B}$ is called "numerical" Dirac monopole. By combining the hydrodynamic pressure with "magnetic pressure", we can write the expression in conservative form:

$$\frac{\partial}{\partial t}\rho v_i + \frac{\partial}{\partial x_k}\left(\rho v_i v_k + p_{tot}\delta_{ik} - \frac{B_k B_i}{4\pi\mu} \right) = -\frac{1}{4\pi\mu} B_i \frac{\partial B_k}{\partial x_k} \quad (1.2.4a)$$

$$p_{tot} = p_h + \frac{B^2}{8\pi\mu}.$$

In the more exploitable vector formulation we have

$$\frac{\partial \rho \mathbf{v}}{\partial t} + \nabla \cdot \left[\rho \mathbf{v}\mathbf{v} + p_{tot} - \frac{\mathbf{B}\mathbf{B}}{4\pi\mu} \right] = -\frac{1}{4\pi\mu}\mathbf{B}\left(\nabla \cdot \mathbf{B}\right). \quad (1.2.4b)$$

1.3. Energy Equation

By taking into account Eq. (1.4), we derive the energy equation in vector form from the equation set (1.3) as

$$\frac{\partial e_h}{\partial t} + \nabla \cdot \left[\mathbf{v}\left(e_h + p_h\right)\right] = \mathbf{j} \cdot \mathbf{E}. \quad (1.3.1)$$

Combining this equation with Ampere's law without omitted displacement current $\frac{\partial \mathbf{D}}{\partial t}$ in Eq. (1.2.1) gives the vector equation

$$\frac{\partial e_h}{\partial t} + \nabla \cdot \left[\mathbf{v}\left(e_h + p_h\right)\right] = \frac{c}{4\pi\mu}\left(\nabla \times \mathbf{B}\right) \cdot \mathbf{E}\,. \tag{1.3.2a}$$

At this stage the Hall term is not included in the energy equation. We assume that this term is small in the case of the plasma for EUV lithographic purposes, but we reserve it for future possible use of the Hall effect. Converting to tensor form, we have

$$\frac{\partial e_h}{\partial t} + \frac{\partial}{\partial x_k}\left[v_k\left(e_h + p_h\right)\right] = \frac{c}{4\pi\mu}\varepsilon_{nkp}\frac{\partial B_p}{\partial x_k}E_n\,. \tag{1.3.2b}$$

With the help of $\frac{\partial}{\partial x_k}\left(\varepsilon_{knp}E_n B_p\right) = B_p\varepsilon_{pkn}\frac{\partial E_n}{\partial x_k} - E_n\varepsilon_{nkp}\frac{\partial B_p}{\partial x_k}$ we can transform the right side of Eq. (1.3.2b),

$$\frac{c}{4\pi\mu}\varepsilon_{knp}\frac{\partial B_p}{\partial x_k}E_n = \frac{c}{4\pi\mu}B_p\varepsilon_{pkn}\frac{\partial E_n}{\partial x_k} - \frac{c}{4\pi\mu}\frac{\partial}{\partial x_k}\left(\varepsilon_{knp}E_n B_p\right). \tag{1.3.3}$$

For subsequent reductions, we use Faraday's law with the current of the numerical magnetic monopole:

$$\nabla \times \mathbf{E} = -\frac{1}{c}\frac{\partial \mathbf{B}}{\partial t} - \frac{1}{c}\mathbf{v}\left(\nabla \cdot \mathbf{B}\right) \quad => \quad \varepsilon_{pkn}\frac{\partial E_n}{\partial x_k} = -\frac{1}{c}\frac{\partial B_p}{\partial t} - \frac{1}{c}v_p\frac{\partial B_k}{\partial x_k}. \tag{1.3.4}$$

Faraday's law allows us to split the magnetic term $\frac{c}{4\pi\mu}\varepsilon_{knp}\frac{\partial B_p}{\partial x_k}E_n$ in Eq. (1.3.4):

$$-\frac{1}{4\pi\mu}B_p\frac{\partial B_p}{\partial t}-\frac{1}{4\pi\mu}B_p v_p\frac{\partial B_k}{\partial x_k}-\frac{c}{4\pi\mu}\frac{\partial}{\partial x_k}\left(\varepsilon_{knp}E_n B_p\right). \qquad (1.3.5)$$

Lorenz and resistance terms of field strength, Eq. (1.4), can be written in tensor form $E_n=-\frac{1}{c}\varepsilon_{nml}v_m B_l+\frac{c\eta}{4\pi\mu}\varepsilon_{nml}\frac{\partial B_l}{\partial x_m}$ and added to Eq. (1.3.5):

$$-\frac{1}{4\pi\mu}B_p\frac{\partial B_p}{\partial t}-\frac{1}{4\pi\mu}B_p v_p\frac{\partial B_k}{\partial x_k}+\frac{1}{4\pi\mu}\frac{\partial}{\partial x_k}\left(\varepsilon_{knp}\varepsilon_{nml}v_m B_l B_p\right)-\frac{c^2}{16\pi^2\mu^2}\frac{\partial}{\partial x_k}\left(\eta\varepsilon_{knp}\varepsilon_{nml}\frac{\partial B_l}{\partial x_m}B_p\right)=$$

$$=-\frac{\partial}{\partial t}\left(\frac{B^2}{8\pi\mu}\right)-\frac{1}{4\pi\mu}B_p v_p\frac{\partial B_k}{\partial x_k}+\frac{1}{4\pi\mu}\frac{\partial}{\partial x_k}\left(\varepsilon_{npk}\varepsilon_{nml}v_m B_l B_p\right)-\frac{c^2}{16\pi^2\mu^2}\frac{\partial}{\partial x_k}\left(\eta\varepsilon_{npk}\varepsilon_{nml}\frac{\partial B_l}{\partial x_m}B_p\right)=$$

$$=-\frac{\partial}{\partial t}\left(\frac{B^2}{8\pi\mu}\right)-\frac{1}{4\pi\mu}B_p v_p\frac{\partial B_k}{\partial x_k}+\frac{1}{4\pi\mu}\frac{\partial}{\partial x_k}\left(\left[\delta_{pm}\delta_{kl}-\delta_{pl}\delta_{km}\right]v_m B_l B_p\right)-$$

$$-\frac{c^2}{16\pi^2\mu^2}\frac{\partial}{\partial x_k}\left(\eta\left[\delta_{pm}\delta_{kl}-\delta_{pl}\delta_{km}\right]\frac{\partial B_l}{\partial x_m}B_p\right)=$$

$$=-\frac{\partial}{\partial t}\left(\frac{B^2}{8\pi\mu}\right)-\frac{1}{4\pi\mu}B_p v_p\frac{\partial B_k}{\partial x_k}+\frac{1}{4\pi\mu}\frac{\partial}{\partial x_k}\left(\delta_{pm}\delta_{kl}v_m B_l B_p\right)-\frac{1}{4\pi\mu}\frac{\partial}{\partial x_k}\left(\delta_{pl}\delta_{km}v_m B_l B_p\right)-$$

$$-\frac{c^2}{16\pi^2\mu^2}\frac{\partial}{\partial x_k}\left(\eta\delta_{pm}\delta_{kl}\frac{\partial B_l}{\partial x_m}B_p\right)+\frac{c^2}{16\pi^2\mu^2}\frac{\partial}{\partial x_k}\left(\eta\delta_{pl}\delta_{km}\frac{\partial B_l}{\partial x_m}B_p\right)=$$

$$=-\frac{\partial}{\partial t}\left(\frac{B^2}{8\pi\mu}\right)-\frac{1}{4\pi\mu}B_p v_p\frac{\partial B_k}{\partial x_k}+\frac{1}{4\pi\mu}\frac{\partial}{\partial x_k}\left(B_k B_m v_m\right)-\frac{1}{4\pi\mu}\frac{\partial}{\partial x_k}\left(v_k B_l B_l\right)-$$

$$-\frac{c^2}{16\pi^2\mu^2}\frac{\partial}{\partial x_k}\left(\eta\frac{\partial B_k}{\partial x_m}B_m\right)+\frac{c^2}{16\pi^2\mu^2}\frac{\partial}{\partial x_k}\left(\eta\frac{\partial B_l}{\partial x_k}B_l\right)=$$

$$=-\frac{\partial}{\partial t}\left(\frac{B^2}{8\pi\mu}\right)+\frac{\partial}{\partial x_k}\left(\frac{B_k B_m v_m}{4\pi\mu}-\frac{v_k B^2}{4\pi\mu}\right)-\frac{1}{4\pi\mu}B_p v_p\frac{\partial B_k}{\partial x_k}+$$

$$+\frac{\partial}{\partial x_k}\left[\frac{c^2}{32\pi^2\mu^2}\left(\eta\frac{\partial B^2}{\partial x_k}\right)-\frac{c^2}{16\pi^2\mu^2}\left(\eta\frac{\partial B_n}{\partial x_m}B_m\right)\right].$$

This transformed term is then equal to the needed to add to the energy equation, Eq. (1.3.2b):

$$\frac{\partial e_h}{\partial t}+\frac{\partial}{\partial x_k}\left[v_k\left(e_h+p_h\right)\right]=-\frac{\partial}{\partial t}\left(\frac{B^2}{8\pi\mu}\right)+\frac{\partial}{\partial x_k}\left(\frac{B_k B_m v_m}{4\pi\mu}-\frac{v_k B^2}{4\pi\mu}\right)-\frac{1}{4\pi\mu}B_p v_p\frac{\partial B_k}{\partial x_k}+ \qquad (1.3.6)$$

$$+\frac{\partial}{\partial x_k}\left[\frac{c^2}{32\pi^2\mu^2}\left(\eta\frac{\partial B^2}{\partial x_k}\right)-\frac{c^2}{16\pi^2\mu^2}\left(\eta\frac{\partial B_k}{\partial x_m}B_m\right)\right]$$

The underlined terms above can be combined with the hydrodynamics energy and pressure. The final expression for energy is

$$\frac{\partial e_{tot}}{\partial t}+\frac{\partial}{\partial x_k}\left[v_k\left(e_{tot}+p_{tot}\right)-\frac{B_k B_m v_m}{4\pi\mu}+\frac{c^2}{16\pi^2\mu^2}\left(\eta\frac{\partial B_k}{\partial x_m}B_m\right)-\frac{c^2}{32\pi^2\mu^2}\left(\eta\frac{\partial B^2}{\partial x_k}\right)\right]=-\frac{1}{4\pi\mu}B_p v_p\frac{\partial B_k}{\partial x_k},$$

where $e_{tot}=e_h+\frac{B^2}{8\pi\mu}, \quad p_{tot}=p_h+\frac{B^2}{8\pi\mu}.$ (1.3.7a)

The vector formulation of the energy equation without resistive term splitting is

$$\frac{\partial e_{tot}}{\partial t}+\nabla\cdot\left[\mathbf{v}\left(e_{tot}+p_{tot}\right)-\frac{1}{4\pi\mu}\left[\mathbf{v}\cdot\mathbf{B}\right]\cdot\mathbf{B}+\frac{c^2\eta}{16\pi^2\mu^2}\left(\nabla\times\mathbf{B}\right)\times\mathbf{B}\right]=-\frac{1}{4\pi\mu}\left(\mathbf{v}\cdot\mathbf{B}\right)\cdot\left(\nabla\cdot\mathbf{B}\right).$$

(1.3.7b)

1.4. Faraday's Equation

The hydrodynamic equations set must be closed with the equation for external force, which can be obtained from Faraday's equation (1.3.4) for magnetic force. Faraday's equation should be reduced to the conservative form just as the magnetic field conservation law. For such a transformation, we use Eq. (1.4) with Lorenz and resistance terms in the tensor form $E_p=-\frac{1}{c}\varepsilon_{pml}v_m B_l+\frac{c\eta}{4\pi\mu}\varepsilon_{pml}\frac{\partial B_l}{\partial x_m}$:

$$\frac{\partial B_i}{\partial t}+c\varepsilon_{ikp}\frac{\partial}{\partial x_k}\left(-\frac{1}{c}\varepsilon_{pml}v_m B_l+\frac{c\eta}{4\pi\mu}\varepsilon_{pml}\frac{\partial B_l}{\partial x_m}\right)+v_i\frac{\partial B_k}{\partial x_k}=0$$

$$\frac{\partial B_i}{\partial t}-\varepsilon_{ikp}\frac{\partial}{\partial x_k}\left(\varepsilon_{pml}v_m B_l\right)+\varepsilon_{ikp}\frac{\partial}{\partial x_k}\left(\frac{c^2\eta}{4\pi\mu}\varepsilon_{pml}\frac{\partial B_l}{\partial x_m}\right)+v_i\frac{\partial B_k}{\partial x_k}=0$$

$$\frac{\partial B_i}{\partial t}-\varepsilon_{pik}\varepsilon_{pml}\frac{\partial}{\partial x_k}\left(v_m B_l\right)+\varepsilon_{pik}\varepsilon_{pml}\frac{\partial}{\partial x_k}\left(\frac{c^2\eta}{4\pi\mu}\frac{\partial B_l}{\partial x_m}\right)+v_i\frac{\partial B_k}{\partial x_k}=0$$

$$\frac{\partial B_i}{\partial t}-\left(\delta_{im}\delta_{kl}-\delta_{il}\delta_{km}\right)\frac{\partial}{\partial x_k}\left(v_m B_l\right)+\left(\delta_{im}\delta_{kl}-\delta_{il}\delta_{km}\right)\frac{\partial}{\partial x_k}\left(\frac{c^2\eta}{4\pi\mu}\frac{\partial B_l}{\partial x_m}\right)+v_i\frac{\partial B_k}{\partial x_k}=0$$

$$\frac{\partial B_i}{\partial t}-\delta_{im}\delta_{kl}\frac{\partial}{\partial x_k}\left(v_m B_l\right)+\delta_{il}\delta_{km}\frac{\partial}{\partial x_k}\left(v_m B_l\right)+\delta_{im}\delta_{kl}\frac{\partial}{\partial x_k}\left(\frac{c^2\eta}{4\pi\mu}\frac{\partial B_l}{\partial x_m}\right)-\delta_{il}\delta_{km}\frac{\partial}{\partial x_k}\left(\frac{c^2\eta}{4\pi\mu}\frac{\partial B_l}{\partial x_m}\right)=-v_i\frac{\partial B_k}{\partial x_k}$$

$$\frac{\partial B_i}{\partial t}-\frac{\partial}{\partial x_k}\left(v_i B_k\right)+\frac{\partial}{\partial x_k}\left(v_k B_i\right)+\frac{\partial}{\partial x_k}\left(\frac{c^2\eta}{4\pi\mu}\frac{\partial B_k}{\partial x_i}\right)-\frac{\partial}{\partial x_k}\left(\frac{c^2\eta}{4\pi\mu}\frac{\partial B_i}{\partial x_k}\right)=-v_i\frac{\partial B_k}{\partial x_k}.$$

The final conservative form of Faraday's equation with the numerical "Dirac monopole" is

$$\frac{\partial B_i}{\partial t}+\frac{\partial}{\partial x_k}\left(v_k B_i-B_k v_i+\frac{c^2\eta}{4\pi\mu}\frac{\partial B_k}{\partial x_i}-\frac{c^2\eta}{4\pi\mu}\frac{\partial B_i}{\partial x_k}\right)=-v_i\frac{\partial B_k}{\partial x_k}. \qquad (1.4.1a)$$

The vector form of this equation without splitting of the resistive term can be given as

$$\frac{\partial \mathbf{B}}{\partial t}+\nabla\cdot\left(\mathbf{vB}-\mathbf{Bv}\right)+\frac{c^2}{4\pi\mu}\nabla\times\left(\eta\nabla\times\mathbf{B}\right)=-\mathbf{v}\left(\nabla\cdot\mathbf{B}\right). \qquad (1.4.1b)$$

From Eqs. (1.3) - (1.4.1), it is possible to write a general system of MHD equations in orthonormalized Cartesian coordinates:

$$
\begin{cases}
\dfrac{\partial \rho}{\partial t}+\dfrac{\partial}{\partial x_k}\left(\rho v_k\right)=0 \\
\dfrac{\partial}{\partial t}\rho v_i+\dfrac{\partial}{\partial x_k}\left(\rho v_i v_k+p_{tot}\delta_{ik}-\dfrac{B_k B_i}{4\pi\mu}\right)=-\dfrac{1}{4\pi\mu}B_i\dfrac{\partial B_k}{\partial x_k} \\
\dfrac{\partial e_{tot}}{\partial t}+\dfrac{\partial}{\partial x_k}\left(v_k\left[e_{tot}+p_{tot}\right]-\dfrac{B_k B_m v_m}{4\pi\mu}+\dfrac{c^2}{16\pi^2\mu^2}\left[\eta\dfrac{\partial B_k}{\partial x_m}B_m\right]-\dfrac{c^2}{32\pi^2\mu^2}\left[\eta\dfrac{\partial B^2}{\partial x_k}\right]\right)=-\dfrac{1}{4\pi\mu}B_p v_p\dfrac{\partial B_k}{\partial x_k} \\
\dfrac{\partial B_i}{\partial t}+\dfrac{\partial}{\partial x_k}\left(v_k B_i-B_k v_i+\dfrac{c^2\eta}{4\pi\mu}\dfrac{\partial B_k}{\partial x_i}-\dfrac{c^2\eta}{4\pi\mu}\dfrac{\partial B_i}{\partial x_k}\right)=-v_i\dfrac{\partial B_k}{\partial x_k},
\end{cases}
\tag{1.4.2}
$$

where $e_{tot}=e_h+\dfrac{B^2}{8\pi\mu}$, $\quad p_{tot}=p_h+\dfrac{B^2}{8\pi\mu}$, and $i,k,m=1,2,3$.

The equation set (1.4.2) may be directly used for 3D TVD-LF calculations in the Cartesian coordinate system. For 2D calculations, however, the equation set (1.4.2) must be changed to another coordinate system, including curvilinear non-orthogonal coordinates. For this case, the equation set (1.4.2) must be transformed to the general tensor form. Bear in mind that v^i and B^i are contravariant vectors and $\partial/\partial x^k$ is a covariant derivative. As a result, $v^i v^k$ is a twice contravariant tensor, and $B^k B^m v^m$ a thrice contravariant tensor. We exclude resistivity terms from Eqs. (1.4.2) because of its large dimensions and consider this problem in the next section. We use the following:

$$
\begin{aligned}
&\operatorname{div}\mathbf{v}=\frac{\partial v^k}{\partial x^k}=\nabla_k v^k, \\
&\frac{\partial v^i}{\partial x^k}=\nabla_k v^i, \\
&\frac{\partial}{\partial t}=\nabla_0 .
\end{aligned}
\tag{1.4.3}
$$

With this notation, we can represent the general MHD system as

$$\begin{cases} \nabla_0 \rho + \nabla_k \left(\rho v^k \right) = 0 \\ \nabla_0 \left(\rho v^i \right) + \nabla_k \left(\rho v^i v^k + p_{tot} \delta^{ik} - \dfrac{B^k B^i}{4\pi\mu} \right) = -\dfrac{1}{4\pi\mu} B^i \nabla_k B^k \\ \nabla_0 e_{tot} + \nabla_k \left(v^k \left[e_{tot} + p_{tot} \right] - \dfrac{B^k B^m v^m}{4\pi\mu} \right) = -\dfrac{1}{4\pi\mu} B^m v^m \nabla_k B^k \\ \nabla_0 B^i + \nabla_k \left(v^k B^i - B^k v^i \right) = -v^i \nabla_k B^k \end{cases} . \qquad (1.4.4a)$$

The equation set (1.4.4a) describes, in general tensor form, ideal MHD equations (without resistivity terms) in all curvilinear coordinates, including nonorthogonal. The next section shows the detailed transformation of these equations for the cylindrical orthonormalized coordinate system. The derived equation set corresponds to the expression in vector form, which is using in most astrophysical applications:

$$\begin{cases} \dfrac{\partial \rho}{\partial t} + \nabla \cdot \left(\rho \mathbf{v} \right) = 0 \\ \dfrac{\partial \rho \mathbf{v}}{\partial t} + \nabla \cdot \left(\rho \mathbf{v}\mathbf{v} + p_{tot} - \dfrac{\mathbf{B}\mathbf{B}}{4\pi\mu} \right) = -\dfrac{1}{4\pi\mu} \mathbf{B} \left(\nabla \cdot \mathbf{B} \right) \\ \dfrac{\partial e_{tot}}{\partial t} + \nabla \cdot \left[\mathbf{v} \left(e_{tot} + p_{tot} \right) - \dfrac{1}{4\pi\mu} \left(\mathbf{v} \cdot \mathbf{B} \right) \cdot \mathbf{B} \right] = -\dfrac{1}{4\pi\mu} \left(\mathbf{v} \cdot \mathbf{B} \right) \cdot \left(\nabla \cdot \mathbf{B} \right) \\ \dfrac{\partial \mathbf{B}}{\partial t} + \nabla \cdot \left(\mathbf{v}\mathbf{B} - \mathbf{B}\mathbf{v} \right) = -\mathbf{v} \left(\nabla \cdot \mathbf{B} \right) \end{cases} . \qquad (1.4.4b)$$

2. Cylindrical Case of MHD Equations

The cylindrical case holds a central place in most practical applications. The HEIGHTS code uses the cylindrical coordinate system for modeling DPP devices [6-8] and for calculating LPP devices [11]. Applying cylindrical symmetry to DPP and LPP devices, we derived a general set of MHD equations (1.4.2) in an axisymmetric geometry (r, φ, z). Plasma motion was neglected along the φ direction, and we assumed that the magnetic field has only one component B_φ. The case of theta-pinch can be easily obtained from the general equations presented in the cylindrical coordinate system.

2.1. Continuity Equation

For transformation of the equation set (1.4.4) in any coordinate system, one must define the covariant derivative of the contravariant components of the tensor or vector in the new coordinate system $\{q^k\}$, $k = 1, 2, 3$. As is well known, the covariant derivative of contravariant components is the same as the physical derivative. For contravariant vector components, this derivative can be written as [12]

$$A^j_{,k} = \frac{1}{h_k}\frac{\partial A^j}{\partial q^k} + \Gamma^j_{nk} A^n, \tag{2.1.1}$$

where Γ^j_{nk} represents Christoffel symbols of the second kind. For the cylindrical coordinate system, only two symbols are nonzero:

$$\Gamma^r_{\varphi\varphi} = -\frac{1}{r} \quad \text{and} \quad \Gamma^{\varphi}_{r\varphi} = \frac{1}{r}. \tag{2.1.2}$$

Similarly, it is possible to define covariant derivatives for double and triple contravariant tensors in Eq. (2.1.1) [13]:

$$A^{kj}_{,k} = \frac{1}{h_k}\frac{\partial A^{kj}}{\partial q^k} + \Gamma^k_{nk} A^{nj} + \Gamma^j_{nk} A^{kn}, \tag{2.1.3}$$

$$A^{kjj}_{,k} = \frac{1}{h_k}\frac{\partial A^{kjj}}{\partial q^k} + \Gamma^k_{nk} A^{njj} + \Gamma^j_{nk} A^{knj} + \Gamma^j_{nk} A^{kjn} \ . \tag{2.1.4}$$

The transformation for the triple contravariant tensor with two equal indices is presented for convenience. Equations (2.1.1) and (2.1.2) can be used in Eq. (1.4.4) for the case of cylindrical coordinates (here and later we include only nonzero Christoffel symbols):

$$\nabla_k\left(\rho v^k\right)=\frac{1}{h_k}\frac{\partial v^k}{\partial q^k}+\Gamma^k_{nk}v^n=\frac{\partial}{\partial r}\left(\rho v^r\right)+\frac{1}{r}\frac{\partial}{\partial\varphi}\left(\rho v^\varphi\right)+\frac{\partial}{\partial z}\left(\rho v_z\right)+\Gamma^\varphi_{r\varphi}\rho v^r=$$

$$=\frac{\partial}{\partial r}\left(\rho v^r\right)+\frac{1}{r}\frac{\partial}{\partial\varphi}\left(\rho v^\varphi\right)+\frac{\partial}{\partial z}\left(\rho v_z\right)+\frac{\rho v^r}{r}=\frac{1}{r}\frac{\partial}{\partial r}\left(r\rho v^r\right)+\frac{1}{r}\frac{\partial}{\partial\varphi}\left(\rho v^\varphi\right)+\frac{\partial}{\partial z}\left(\rho v_z\right) \tag{2.1.5a}$$

The final result is

$$\frac{\partial\rho}{\partial t}+\frac{1}{r}\frac{\partial}{\partial r}\left(r\rho v^r\right)+\frac{1}{r}\frac{\partial}{\partial\varphi}\left(\rho v^\varphi\right)+\frac{\partial}{\partial z}\left(\rho v^z\right)=0\,. \tag{2.1.5b}$$

2.2. Equation of Motion

By taking into account that $v^i v^k$ is the double contravariant tensor, we can revise Eq (2.1.5) as follow

$$\left(\rho v^r v^k\right)_{;k}=\frac{1}{h_r}\frac{\partial\left(\rho v^r v^r\right)}{\partial r}+\frac{1}{h_\varphi}\frac{\partial\left(\rho v^r v^\varphi\right)}{\partial\varphi}+\frac{1}{h_z}\frac{\partial\left(\rho v^r v^z\right)}{\partial z}+\Gamma^\varphi_{r\varphi}\rho v^r v^r+\Gamma^r_{\varphi\varphi}\rho v^\varphi v^\varphi=$$

$$=\frac{\partial\left(\rho v^r v^r\right)}{\partial r}+\frac{1}{r}\frac{\partial\left(\rho v^r v^\varphi\right)}{\partial\varphi}+\frac{\partial\left(\rho v^r v^z\right)}{\partial z}+\frac{\rho v^r v^r}{r}-\frac{\rho v^\varphi v^\varphi}{r}=$$

$$=\frac{\partial\left(\rho v^r v^r\right)}{\partial r}+\frac{\rho v^r v^r}{r}+\frac{1}{r}\frac{\partial\left(\rho v^r v^\varphi\right)}{\partial\varphi}+\frac{\partial\left(\rho v^r v^z\right)}{\partial z}-\frac{\rho v^\varphi v^\varphi}{r}=$$

$$=\frac{1}{r}\frac{\partial}{\partial r}\left(r\rho v^r v^r\right)+\frac{1}{r}\frac{\partial\left(\rho v^r v^\varphi\right)}{\partial\varphi}+\frac{\partial\left(\rho v^r v^z\right)}{\partial z}-\frac{\rho v^\varphi v^\varphi}{r}\,, \tag{2.2.1}$$

$$\left(\rho v^\varphi v^k\right)_{;k}=\frac{1}{h_r}\frac{\partial\left(\rho v^\varphi v^r\right)}{\partial r}+\frac{1}{h_\varphi}\frac{\partial\left(\rho v^\varphi v^\varphi\right)}{\partial\varphi}+\frac{1}{h_z}\frac{\partial\left(\rho v^\varphi v^z\right)}{\partial z}+\Gamma^\varphi_{r\varphi}\rho v^r v^\varphi+\Gamma^\varphi_{r\varphi}\rho v^r v^\varphi=$$

$$=\frac{\partial\left(\rho v^\varphi v^r\right)}{\partial r}+\frac{1}{r}\frac{\partial\left(\rho v^\varphi v^\varphi\right)}{\partial\varphi}+\frac{\partial\left(\rho v^\varphi v^z\right)}{\partial z}+\frac{\rho v^r v^\varphi}{r}+\frac{\rho v^r v^\varphi}{r}=$$

$$=\frac{\partial\left(\rho v^\varphi v^r\right)}{\partial r}+\frac{\rho v^r v^\varphi}{r}+\frac{1}{r}\frac{\partial\left(\rho v^\varphi v^\varphi\right)}{\partial\varphi}+\frac{\partial\left(\rho v^\varphi v^z\right)}{\partial z}+\frac{\rho v^r v^\varphi}{r}=$$

$$= \frac{1}{r}\frac{\partial}{\partial r}\left(r\rho v^{\varphi}v^{r}\right)+\frac{1}{r}\frac{\partial\left(\rho v^{\varphi}v^{\varphi}\right)}{\partial\varphi}+\frac{\partial\left(\rho v^{\varphi}v^{z}\right)}{\partial z}+\frac{\rho v^{r}v^{\varphi}}{r}, \tag{2.2.2}$$

$$\left(\rho v^{z}v^{k}\right)_{;k}=\frac{1}{h_r}\frac{\partial\left(\rho v^{z}v^{r}\right)}{\partial r}+\frac{1}{h_{\varphi}}\frac{\partial\left(\rho v^{z}v^{\varphi}\right)}{\partial\varphi}+\frac{1}{h_z}\frac{\partial\left(\rho v^{z}v^{z}\right)}{\partial z}+\Gamma^{\varphi}_{r\varphi}\rho v^{r}v^{z}=$$

$$=\frac{\partial\left(\rho v^{z}v^{r}\right)}{\partial r}+\frac{\rho v^{r}v^{z}}{r}+\frac{1}{r}\frac{\partial\left(\rho v^{z}v^{\varphi}\right)}{\partial\varphi}+\frac{\partial\left(\rho v^{z}v^{z}\right)}{\partial z}=\frac{1}{r}\frac{\partial}{\partial r}\left(r\rho v^{z}v^{r}\right)+\frac{1}{r}\frac{\partial\left(\rho v^{z}v^{\varphi}\right)}{\partial\varphi}+\frac{\partial\left(\rho v^{z}v^{z}\right)}{\partial z}. \tag{2.2.3}$$

The magnetic term with tensor $B^{i}B^{k}$ can be represented similarly:

$$\left(-\frac{B^{r}B^{k}}{4\pi\mu}\right)_{;k}=-\frac{1}{r}\frac{\partial}{\partial r}\left(\frac{rB^{r}B^{r}}{4\pi\mu}\right)-\frac{1}{r}\frac{\partial}{\partial\varphi}\left(\frac{B^{r}B^{\varphi}}{4\pi\mu}\right)-\frac{\partial}{\partial z}\left(\frac{B^{r}B^{z}}{4\pi\mu}\right)+\frac{B^{\varphi}B^{\varphi}}{r4\pi\mu}, \tag{2.2.4}$$

$$\left(-\frac{B^{\varphi}B^{k}}{4\pi\mu}\right)_{;k}=-\frac{1}{r}\frac{\partial}{\partial r}\left(\frac{rB^{\varphi}B^{r}}{4\pi\mu}\right)-\frac{1}{r}\frac{\partial}{\partial\varphi}\left(\frac{B^{\varphi}B^{\varphi}}{4\pi\mu}\right)-\frac{\partial}{\partial z}\left(\frac{B^{\varphi}B^{z}}{4\pi\mu}\right)-\frac{B^{r}B^{\varphi}}{r4\pi\mu}, \tag{2.2.5}$$

$$\left(-\frac{B^{z}B^{k}}{4\pi\mu}\right)_{;k}=-\frac{1}{r}\frac{\partial}{\partial r}\left(\frac{rB^{z}B^{r}}{4\pi\mu}\right)-\frac{1}{r}\frac{\partial}{\partial\varphi}\left(\frac{B^{z}B^{\varphi}}{4\pi\mu}\right)-\frac{\partial}{\partial z}\left(\frac{B^{z}B^{z}}{4\pi\mu}\right). \tag{2.2.6}$$

These equations can be rewritten with divergence of the magnetic field:

$$\begin{aligned}
-\frac{1}{4\pi\mu}B^{r}B^{k}_{;k}&=-\frac{B^{r}}{r4\pi\mu}\frac{\partial\left(rB^{r}\right)}{\partial r}-\frac{B^{r}}{r4\pi\mu}\frac{\partial B^{\varphi}}{\partial\varphi}-\frac{B^{r}}{4\pi\mu}\frac{\partial B^{z}}{\partial z},\\
-\frac{1}{4\pi\mu}B^{\varphi}B^{k}_{;k}&=-\frac{B^{\varphi}}{r4\pi\mu}\frac{\partial\left(rB^{r}\right)}{\partial r}-\frac{B^{\varphi}}{r4\pi\mu}\frac{\partial B^{\varphi}}{\partial\varphi}-\frac{B^{\varphi}}{4\pi\mu}\frac{\partial B^{z}}{\partial z},\\
-\frac{1}{4\pi\mu}B^{z}B^{k}_{;k}&=-\frac{B^{z}}{r4\pi\mu}\frac{\partial\left(rB^{r}\right)}{\partial r}-\frac{B^{z}}{r4\pi\mu}\frac{\partial B^{\varphi}}{\partial\varphi}-\frac{B^{z}}{4\pi\mu}\frac{\partial B^{z}}{\partial z}.
\end{aligned} \tag{2.2.7}$$

From Eqs. (2.2.1)-(2.2.7), we can write the final equation of motion in the cylindrical coordinate system in projection to the r, φ, and z axes:

$$\frac{\partial \rho v^r}{\partial t}+\frac{1}{r}\frac{\partial}{\partial r}r\left(\rho v^r v^r-\frac{B^r B^r}{4\pi\mu}\right)+\frac{1}{r}\frac{\partial}{\partial \varphi}\left(\rho v^r v^\varphi-\frac{B^r B^\varphi}{4\pi\mu}\right)+\frac{\partial}{\partial z}\left(\rho v^r v^z-\frac{B^r B^z}{4\pi\mu}\right)+\frac{\partial p_{tot}}{\partial r}-\frac{\rho v^\varphi v^\varphi}{r}+\frac{B^\varphi B^\varphi}{r4\pi\mu}=$$
$$=-\frac{B^r}{r4\pi\mu}\frac{\partial\left(rB^r\right)}{\partial r}-\frac{B^r}{r4\pi\mu}\frac{\partial B^\varphi}{\partial \varphi}-\frac{B^r}{4\pi\mu}\frac{\partial B^z}{\partial z}$$

$$\frac{\partial \rho v^\varphi}{\partial t}+\frac{1}{r}\frac{\partial}{\partial r}r\left(\rho v^\varphi v^r-\frac{B^\varphi B^r}{4\pi\mu}\right)+\frac{1}{r}\frac{\partial}{\partial \varphi}\left(\rho v^\varphi v^\varphi+p_{tot}-\frac{B^\varphi B^\varphi}{4\pi\mu}\right)+\frac{\partial}{\partial z}\left(\rho v^\varphi v^z-\frac{B^\varphi B^z}{4\pi\mu}\right)-\frac{\rho v^r v^\varphi}{r}+\frac{B^r B^\varphi}{r4\pi\mu}=$$
$$=-\frac{B^\varphi}{r4\pi\mu}\frac{\partial\left(rB^r\right)}{\partial r}-\frac{B^\varphi}{r4\pi\mu}\frac{\partial B^\varphi}{\partial \varphi}-\frac{B^\varphi}{4\pi\mu}\frac{\partial B^z}{\partial z}$$

$$\frac{\partial \rho v^z}{\partial t}+\frac{1}{r}\frac{\partial}{\partial r}r\left(\rho v^z v^r-\frac{B^z B^r}{4\pi\mu}\right)+\frac{1}{r}\frac{\partial}{\partial \varphi}\left(\rho v^z v^\varphi-\frac{B^z B^\varphi}{4\pi\mu}\right)+\frac{\partial}{\partial z}\left(\rho v^z v^z+p_{tot}-\frac{B^z B^z}{4\pi\mu}\right)=$$
$$=-\frac{B^z}{r4\pi\mu}\frac{\partial\left(rB^r\right)}{\partial r}-\frac{B^z}{r4\pi\mu}\frac{\partial B^\varphi}{\partial \varphi}-\frac{B^z}{4\pi\mu}\frac{\partial B^z}{\partial z}. \qquad (2.2.8)$$

2.3. Energy Equation

Energy conservation in a cylindrical system can be obtained by splitting the term $-\frac{B^k B^m v^m}{4\pi\mu}$ as a triple contravariant tensor. From Eq. (2.1.4) we have

$$\left(B^k B^m v^m\right)_{;k}=\frac{1}{h_k}\frac{\partial\left(B^k B^m v^m\right)}{\partial q^k}+\Gamma^k_{nk}B^n B^m v^m+\Gamma^m_{nk}B^k B^n v^m+\Gamma^m_{nk}B^k B^m v^n=$$
$$=\frac{\partial\left(B^r B^r v^r\right)}{\partial r}+\frac{\partial\left(B^r B^\varphi v^\varphi\right)}{\partial r}+\frac{\partial\left(B^r B^z v^z\right)}{\partial r}+\frac{1}{r}\frac{\partial\left(B^\varphi B^r v^r\right)}{\partial \varphi}+\frac{1}{r}\frac{\partial\left(B^\varphi B^\varphi v^\varphi\right)}{\partial \varphi}+\frac{1}{r}\frac{\partial\left(B^\varphi B^z v^z\right)}{\partial \varphi}+$$
$$+\frac{\partial\left(B^z B^r v^r\right)}{\partial z}+\frac{\partial\left(B^z B^\varphi v^\varphi\right)}{\partial z}+\frac{\partial\left(B^z B^z v^z\right)}{\partial z}+\Gamma^\varphi_{r\varphi}B^r B^r v^r+\Gamma^\varphi_{r\varphi}B^r B^\varphi v^\varphi+\Gamma^\varphi_{r\varphi}B^r B^z v^z+$$
$$+\Gamma^r_{\varphi\varphi}B^\varphi B^\varphi v^r+\Gamma^\varphi_{r\varphi}B^\varphi B^r v^\varphi+\Gamma^r_{\varphi\varphi}B^\varphi B^r v^\varphi+\Gamma^\varphi_{r\varphi}B^\varphi B^\varphi v^r=$$
$$=\frac{\partial\left(B^r B^r v^r\right)}{\partial r}+\frac{\partial\left(B^r B^\varphi v^\varphi\right)}{\partial r}+\frac{\partial\left(B^r B^z v^z\right)}{\partial r}+\frac{1}{r}\frac{\partial\left(B^\varphi B^r v^r\right)}{\partial \varphi}+\frac{1}{r}\frac{\partial\left(B^\varphi B^\varphi v^\varphi\right)}{\partial \varphi}+\frac{1}{r}\frac{\partial\left(B^\varphi B^z v^z\right)}{\partial \varphi}+$$
$$+\frac{\partial\left(B^z B^r v^r\right)}{\partial z}+\frac{\partial\left(B^z B^\varphi v^\varphi\right)}{\partial z}+\frac{\partial\left(B^z B^z v^z\right)}{\partial z}+\frac{B^r B^r v^r}{r}+\frac{B^r B^\varphi v^\varphi}{r}+\frac{B^r B^z v^z}{r}-$$

$$-\cancel{\frac{B^{\varphi}B^{\varphi}v^{r}}{r}}+\cancel{\frac{B^{\varphi}B^{r}v^{\varphi}}{r}}-\cancel{\frac{B^{\varphi}B^{r}v^{\varphi}}{r}}+\cancel{\frac{B^{\varphi}B^{\varphi}v^{r}}{r}}=$$

$$=\frac{1}{r}\frac{\partial}{\partial r}\left(rB^{r}B^{r}v^{r}\right)+\frac{1}{r}\frac{\partial}{\partial r}\left(rB^{r}B^{\varphi}v^{\varphi}\right)+\frac{1}{r}\frac{\partial}{\partial r}\left(rB^{r}B^{z}v^{z}\right)+$$

$$+\frac{1}{r}\frac{\partial\left(B^{\varphi}B^{r}v^{r}\right)}{\partial\varphi}+\frac{1}{r}\frac{\partial\left(B^{\varphi}B^{\varphi}v^{\varphi}\right)}{\partial\varphi}+\frac{1}{r}\frac{\partial\left(B^{\varphi}B^{z}v^{z}\right)}{\partial\varphi}+\frac{\partial\left(B^{z}B^{r}v^{r}\right)}{\partial z}+\frac{\partial\left(B^{z}B^{\varphi}v^{\varphi}\right)}{\partial z}+\frac{\partial\left(B^{z}B^{z}v^{z}\right)}{\partial z}=$$

$$\frac{1}{r}\frac{\partial}{\partial r}\left[rB^{r}\left(B^{r}v^{r}+B^{\varphi}v^{\varphi}+B^{z}v^{z}\right)\right]+\frac{1}{r}\frac{\partial}{\partial\varphi}\left[B^{\varphi}\left(B^{r}v^{r}+B^{\varphi}v^{\varphi}+B^{z}v^{z}\right)\right]+\frac{\partial}{\partial z}\left[B^{z}\left(B^{r}v^{r}+B^{\varphi}v^{\varphi}+B^{z}v^{z}\right)\right]$$

$$=\frac{1}{r}\frac{\partial}{\partial r}\left[rB^{r}\mathbf{Bv}\right]+\frac{1}{r}\frac{\partial}{\partial\varphi}\left[B^{\varphi}\mathbf{Bv}\right]+\frac{\partial}{\partial z}\left[B^{z}\mathbf{Bv}\right].$$

As the tensor $B^{m}v^{m}$ is a simple scalar, we can write

$$-\frac{B^{k}B^{m}v^{m}}{4\pi\mu}=-\frac{1}{r4\pi\mu}\frac{\partial}{\partial r}\left[rB^{r}\mathbf{Bv}\right]-\frac{1}{r4\pi\mu}\frac{\partial}{\partial\varphi}\left[B^{\varphi}\mathbf{Bv}\right]+\frac{1}{4\pi\mu}\frac{\partial}{\partial z}\left[B^{z}\mathbf{Bv}\right] \tag{2.3.1}$$

$$\left(v^{k}\left[e_{tot}+p_{tot}\right]\right)_{;k}=\frac{1}{r}\frac{\partial}{\partial r}\left(rv^{r}\left[e_{tot}+p_{tot}\right]\right)+\frac{1}{r}\frac{\partial}{\partial\varphi}\left(v^{\varphi}\left[e_{tot}+p_{tot}\right]\right)+\frac{\partial}{\partial z}\left(v^{z}\left[e_{tot}+p_{tot}\right]\right) \tag{2.3.2}$$

$$B^{j}v^{j}\left(B^{k}\right)_{;k}=\frac{\mathbf{Bv}}{r}\frac{\partial}{\partial r}\left[rB^{r}\right]+\frac{\mathbf{Bv}}{r}\frac{\partial}{\partial\varphi}\left[B^{\varphi}\right]+\mathbf{Bv}\frac{\partial}{\partial z}\left[B^{z}\right]. \tag{2.3.3}$$

In this way, the final expression for energy in a cylindrical system of coordinates is

$$\frac{\partial e_{tot}}{\partial t}+\frac{1}{r}\frac{\partial}{\partial r}\left\{r\left[v^{r}\left(e_{tot}+p_{tot}\right)-\frac{B^{r}\mathbf{Bv}}{4\pi\mu}\right]\right\}+\frac{1}{r}\frac{\partial}{\partial\varphi}\left\{v^{\varphi}\left[e_{tot}+p_{tot}\right]-\frac{B^{\varphi}\mathbf{Bv}}{4\pi\mu}\right\}+ \tag{2.3.4}$$

$$+\frac{\partial}{\partial z}\left\{v^{z}\left[e_{tot}+p_{tot}\right]-\frac{B^{z}\mathbf{Bv}}{4\pi\mu}\right\}=-\frac{\mathbf{Bv}}{r4\pi\mu}\frac{\partial}{\partial r}\left[rB^{r}\right]-\frac{\mathbf{Bv}}{r4\pi\mu}\frac{\partial}{\partial\varphi}\left[B^{\varphi}\right]-\frac{\mathbf{Bv}}{4\pi\mu}\frac{\partial}{\partial z}\left[B^{z}\right].$$

2.4. Faraday's Equation

Analogously to the velocity tensors Eqs. (2.2.1)-(2.2.3), the magnetic field terms can be transformed:

$$\left(v^k B^r\right)_{;k} = \frac{\partial\left(v^r B^r\right)}{\partial r}+\frac{1}{r}\frac{\partial\left(v^\varphi B^r\right)}{\partial \varphi}+\frac{\partial\left(v^z B^r\right)}{\partial z}-\frac{v^\varphi B^\varphi}{r}+\frac{v^r B^r}{r} =$$

$$= \frac{1}{r}\frac{\partial}{\partial r}\left(r v^r B^r\right)+\frac{1}{r}\frac{\partial\left(v^\varphi B^r\right)}{\partial \varphi}+\frac{\partial\left(v^z B^r\right)}{\partial z}-\frac{v^\varphi B^\varphi}{r}$$

$$\left(v^k B^\varphi\right)_{;k} = \frac{\partial\left(v^r B^\varphi\right)}{\partial r}+\frac{1}{r}\frac{\partial\left(v^\varphi B^\varphi\right)}{\partial \varphi}+\frac{\partial\left(v^z B^\varphi\right)}{\partial z}+\frac{v^\varphi B^r}{r}+\frac{v^r B^\varphi}{r} =$$

$$= \frac{1}{r}\frac{\partial}{\partial r}\left(r v^r B^\varphi\right)+\frac{1}{r}\frac{\partial\left(v^\varphi B^\varphi\right)}{\partial \varphi}+\frac{\partial\left(v^z B^\varphi\right)}{\partial z}+\frac{v^\varphi B^r}{r}$$

$$\left(v^k B^z\right)_{;k} = \frac{\partial\left(v^r B^z\right)}{\partial r}+\frac{1}{r}\frac{\partial\left(v^\varphi B^z\right)}{\partial \varphi}+\frac{\partial\left(v^z B^z\right)}{\partial z}+\frac{v^r B^z}{r} =$$

$$= \frac{1}{r}\frac{\partial}{\partial r}\left(r v^r B^z\right)+\frac{1}{r}\frac{\partial\left(v^\varphi B^z\right)}{\partial \varphi}+\frac{\partial\left(v^z B^z\right)}{\partial z}.$$

By index change, we have the following:

$$\left(B^k v^r\right)_{;k} = \frac{1}{r}\frac{\partial}{\partial r}\left(r B^r v^r\right)+\frac{1}{r}\frac{\partial\left(B^\varphi v^r\right)}{\partial \varphi}+\frac{\partial\left(B^z v^r\right)}{\partial z}-\frac{B^\varphi v^\varphi}{r}$$

$$\left(B^k v^\varphi\right)_{;k} = \frac{1}{r}\frac{\partial}{\partial r}\left(r B^r v^\varphi\right)+\frac{1}{r}\frac{\partial\left(B^\varphi v^\varphi\right)}{\partial \varphi}+\frac{\partial\left(B^z v^\varphi\right)}{\partial z}+\frac{B^\varphi v^r}{r}$$

$$\left(B^k v^z\right)_{;k} = \frac{1}{r}\frac{\partial}{\partial r}\left(r B^r v^z\right)+\frac{1}{r}\frac{\partial\left(B^\varphi v^z\right)}{\partial \varphi}+\frac{\partial\left(B^z v^z\right)}{\partial z}$$

$$v^r \frac{\partial B^k}{\partial x^k} = v^r\left\{\frac{1}{r}\frac{\partial}{\partial r}\left(r B^r\right)+\frac{1}{r}\frac{\partial\left(B^\varphi\right)}{\partial \varphi}+\frac{\partial\left(B^z\right)}{\partial z}\right\}$$

$$v^\varphi \frac{\partial B^k}{\partial x^k} = \left\{\frac{1}{r}\frac{\partial}{\partial r}\left(r B^r\right)+\frac{1}{r}\frac{\partial\left(B^\varphi\right)}{\partial \varphi}+\frac{\partial\left(B^z\right)}{\partial z}\right\} v^\varphi$$

$$v^z \frac{\partial B^k}{\partial x^k} = \left\{\frac{1}{r}\frac{\partial}{\partial r}\left(r B^r\right)+\frac{1}{r}\frac{\partial\left(B^\varphi\right)}{\partial \varphi}+\frac{\partial\left(B^z\right)}{\partial z}\right\} v^z$$

$$\frac{\partial B^r}{\partial t}+\frac{1}{r}\frac{\partial}{\partial r}\left\{r\left[v^r B^r - B^r v^r\right]\right\}+\frac{1}{r}\frac{\partial\left[v^\varphi B^r - B^\varphi v^r\right]}{\partial\varphi}+\frac{\partial\left[v^z B^r - B^z v^r\right]}{\partial z}-\frac{v^\varphi B^\varphi}{r}+\frac{B^\varphi v^\varphi}{r}=$$
$$=-v^r\left\{\frac{1}{r}\frac{\partial}{\partial r}\left(rB^r\right)+\frac{1}{r}\frac{\partial\left(B^\varphi\right)}{\partial\varphi}+\frac{\partial\left(B^z\right)}{\partial z}\right\}$$

$$\frac{\partial B^r}{\partial t}+\frac{1}{r}\frac{\partial\left[v^\varphi B^r - B^\varphi v^r\right]}{\partial\varphi}+\frac{\partial\left[v^z B^r - B^z v^r\right]}{\partial z}=-v^r\left\{\frac{1}{r}\frac{\partial}{\partial r}\left(rB^r\right)+\frac{1}{r}\frac{\partial\left(B^\varphi\right)}{\partial\varphi}+\frac{\partial\left(B^z\right)}{\partial z}\right\}$$

$$\frac{\partial B^\varphi}{\partial t}+\frac{1}{r}\frac{\partial}{\partial r}\left\{r\left[v^r B^\varphi - B^r v^\varphi\right]\right\}+\frac{1}{r}\frac{\partial\left[v^\varphi B^\varphi - B^\varphi v^\varphi\right]}{\partial\varphi}+\frac{\partial\left[v^z B^\varphi - B^z v^\varphi\right]}{\partial z}+\frac{v^\varphi B^r}{r}-\frac{B^\varphi v^r}{r}=$$
$$=-v^\varphi\left\{\frac{1}{r}\frac{\partial}{\partial r}\left(rB^r\right)+\frac{1}{r}\frac{\partial\left(B^\varphi\right)}{\partial\varphi}+\frac{\partial\left(B^z\right)}{\partial z}\right\}$$

$$\frac{\partial B^\varphi}{\partial t}+\frac{1}{r}\frac{\partial}{\partial r}\left\{r\left[v^r B^\varphi - B^r v^\varphi\right]\right\}+\frac{\partial\left[v^z B^\varphi - B^z v^\varphi\right]}{\partial z}+\frac{v^\varphi B^r}{r}-\frac{B^\varphi v^r}{r}=-v^\varphi\left\{\frac{1}{r}\frac{\partial}{\partial r}\left(rB^r\right)+\frac{1}{r}\frac{\partial\left(B^\varphi\right)}{\partial\varphi}+\frac{\partial\left(B^z\right)}{\partial z}\right\}$$

$$\frac{\partial B^z}{\partial t}+\frac{1}{r}\frac{\partial}{\partial r}\left\{r\left[v^r B^z - B^r v^z\right]\right\}+\frac{1}{r}\frac{\partial\left[v^\varphi B^z - B^\varphi v^z\right]}{\partial\varphi}+\frac{\partial\left[v^z B^z - B^z v^z\right]}{\partial z}=$$
$$=-v^z\left\{\frac{1}{r}\frac{\partial}{\partial r}\left(rB^r\right)+\frac{1}{r}\frac{\partial\left(B^\varphi\right)}{\partial\varphi}+\frac{\partial\left(B^z\right)}{\partial z}\right\}$$

$$\frac{\partial B^z}{\partial t}+\frac{1}{r}\frac{\partial}{\partial r}\left\{r\left[v^r B^z - B^r v^z\right]\right\}+\frac{1}{r}\frac{\partial\left[v^\varphi B^z - B^\varphi v^z\right]}{\partial\varphi}=-v^z\left\{\frac{1}{r}\frac{\partial}{\partial r}\left(rB^r\right)+\frac{1}{r}\frac{\partial\left(B^\varphi\right)}{\partial\varphi}+\frac{\partial\left(B^z\right)}{\partial z}\right\}.$$

Finally, the equations for Faraday's law in the cylindrical coordinate system with magnetic field divergence stabilizer are

$$\frac{\partial B^r}{\partial t}+\frac{1}{r}\frac{\partial\left[v^\varphi B^r - B^\varphi v^r\right]}{\partial\varphi}+\frac{\partial\left[v^z B^r - B^z v^r\right]}{\partial z}=-v^r\left\{\frac{1}{r}\frac{\partial}{\partial r}\left(rB^r\right)+\frac{1}{r}\frac{\partial\left(B^\varphi\right)}{\partial\varphi}+\frac{\partial\left(B^z\right)}{\partial z}\right\}$$

$$\frac{\partial B^\varphi}{\partial t}+\frac{1}{r}\frac{\partial}{\partial r}\left\{r\left[v^r B^\varphi - B^r v^\varphi\right]\right\}+\frac{\partial\left[v^z B^\varphi - B^z v^\varphi\right]}{\partial z}+\frac{v^\varphi B^r}{r}-\frac{B^\varphi v^r}{r}=-v^\varphi\left\{\frac{1}{r}\frac{\partial}{\partial r}\left(rB^r\right)+\frac{1}{r}\frac{\partial\left(B^\varphi\right)}{\partial\varphi}+\frac{\partial\left(B^z\right)}{\partial z}\right\}$$

$$\frac{\partial B^z}{\partial t}+\frac{1}{r}\frac{\partial}{\partial r}\left\{r\left[v^r B^z - B^r v^z\right]\right\}+\frac{1}{r}\frac{\partial\left[v^\varphi B^z - B^\varphi v^z\right]}{\partial\varphi}=-v^z\left\{\frac{1}{r}\frac{\partial}{\partial r}\left(rB^r\right)+\frac{1}{r}\frac{\partial\left(B^\varphi\right)}{\partial\varphi}+\frac{\partial\left(B^z\right)}{\partial z}\right\}. \quad (2.4.1)$$

2.5. Magnetic Diffusion Terms

Modeling of laboratory plasma applications demands consideration of non-ideal diffusive magnetic problems. Dissipation of magnetic energy appears in the form of Joule heat in the energy equation and the diffusive term in Faraday's equation. These terms can be transformed to the cylindrical case from Eqs. (1.16b) and (1.17b):

$$\begin{aligned}\frac{c^2}{16\pi^2\mu^2}\nabla\left[\eta(\nabla\times\mathbf{B})\times\mathbf{B}\right] = {} & \frac{c^2}{16\pi^2\mu^2 r}\frac{\partial}{\partial r}\left\{r\eta\left[B^z\left(\frac{\partial B^r}{\partial z}-\frac{\partial B^z}{\partial r}\right)-\frac{B^\varphi}{r}\left(\frac{\partial}{\partial r}\left(rB^\varphi\right)-\frac{\partial B^r}{\partial\varphi}\right)\right]\right\}+\\ & +\frac{c^2}{16\pi^2\mu^2 r}\frac{\partial}{\partial\varphi}\left\{\eta\left[\frac{B^r}{r}\left(\frac{\partial}{\partial r}\left(rB^\varphi\right)-\frac{\partial B^r}{\partial\varphi}\right)-B^z\left(\frac{1}{r}\frac{\partial B^z}{\partial\varphi}-\frac{\partial B^\varphi}{\partial z}\right)\right]\right\}+\\ & +\frac{c^2}{16\pi^2\mu^2}\frac{\partial}{\partial z}\left\{\eta\left[B^\varphi\left(\frac{1}{r}\frac{\partial B^z}{\partial\varphi}-\frac{\partial B^\varphi}{\partial r}\right)-B^r\left(\frac{\partial B^r}{\partial z}-\frac{\partial B^z}{\partial r}\right)\right]\right\}. \quad (2.5.1)\end{aligned}$$

Faraday's equation with resistivity term splitting yields

$$\begin{aligned}\frac{c^2}{4\pi\mu}\nabla\times\eta\nabla\times\mathbf{B} = {} & \frac{c^2}{4\pi\mu}\left\{\frac{1}{r}\frac{\partial}{\partial\varphi}\left[\frac{\eta}{r}\frac{\partial}{\partial r}\left(rB^\varphi\right)-\frac{\eta}{r}\frac{\partial B^r}{\partial\varphi}\right]-\frac{\partial}{\partial z}\left[\eta\frac{\partial B^r}{\partial z}-\eta\frac{\partial B^z}{\partial r}\right]\right\}\vec{e}_r \quad +\\ & +\frac{c^2}{4\pi\mu}\left\{\frac{\partial}{\partial z}\left[\frac{\eta}{r}\frac{\partial B^z}{\partial\varphi}-\eta\frac{\partial B^\varphi}{\partial z}\right]-\frac{\partial}{\partial r}\left[\frac{\eta}{r}\frac{\partial}{\partial r}\left(rB^\varphi\right)-\frac{\eta}{r}\frac{\partial B^r}{\partial\varphi}\right]\right\}\vec{e}_\varphi \quad +\\ & +\frac{c^2}{4\pi\mu r}\left\{\frac{\partial}{\partial r}\left[r\eta\frac{\partial B^r}{\partial z}-r\eta\frac{\partial B^z}{\partial r}\right]-\frac{\partial}{\partial\varphi}\left[\frac{\eta}{r}\frac{\partial B^z}{\partial\varphi}-\eta\frac{\partial B^\varphi}{\partial z}\right]\right\}\vec{e}_z. \quad (2.5.2)\end{aligned}$$

2.6. Case Studies for Cylindrical Symmetry

In this section we present MHD equations for practical application in the two most exploitable cases: Z-pinch and Θ-pinch. In the first case, it is assumed that the plasma current is strongly parallel to the *z*-axis and one is uniform along the φ-axis. At the same time, the current can have a gradient in the *r* and *z* directions. The magnetic field has only one φ-projection in this ideal symmetric case. This idealization does not remove general plasma processes. Hence, we can have the *z*-gradient of the magnetic field B^{φ} as a result of the current *z*-gradient (for example, by fluctuation of resistivity η). In this case, we have the *z*-gradient of magnetic tension $-\frac{B^{\varphi}B^{\varphi}}{r4\pi\mu}$ and a Rayleigh-Taylor type instability. On the basis of these assumptions, the final MHD system for Z-pinch symmetry that is used in HEIGHTS is given by

$$
\begin{aligned}
&\frac{\partial\rho}{\partial t}+\frac{1}{r}\frac{\partial}{\partial r}\left(r\rho v^{r}\right)+\frac{\partial}{\partial z}\left(\rho v^{z}\right)=0\\
&\frac{\partial\rho v^{r}}{\partial t}+\frac{1}{r}\frac{\partial}{\partial r}r\left(\rho v^{r}v^{r}\right)+\frac{\partial}{\partial z}\left(\rho v^{r}v^{z}\right)+\frac{\partial p_{tot}}{\partial r}=-\frac{B^{\varphi}B^{\varphi}}{r4\pi\mu}\\
&\frac{\partial\rho v^{z}}{\partial t}+\frac{1}{r}\frac{\partial}{\partial r}r\left(\rho v^{z}v^{r}\right)+\frac{\partial}{\partial z}\left(\rho v^{z}v^{z}+p_{tot}\right)=0 \qquad (2.6.1)\\
&\frac{\partial e_{tot}}{\partial t}+\frac{1}{r}\frac{\partial}{\partial r}\left\{r\left[v^{r}\left(e_{tot}+p_{tot}\right)\right]-\frac{c^{2}\eta B^{\varphi}}{16\pi^{2}\mu^{2}}\left[\frac{\partial}{\partial r}\left(rB^{\varphi}\right)\right]\right\}+\frac{\partial}{\partial z}\left\{v^{z}\left[e_{tot}+p_{tot}\right]-\frac{c^{2}\eta B^{\varphi}}{16\pi^{2}\mu^{2}}\left[\frac{\partial B^{\varphi}}{\partial r}\right]\right\}=0\\
&\frac{\partial B^{\varphi}}{\partial t}+\frac{\partial}{\partial r}\left\{v^{r}B^{\varphi}-\frac{c^{2}\eta}{r4\pi\mu}\frac{\partial}{\partial r}\left(rB^{\varphi}\right)\right\}+\frac{\partial}{\partial z}\left\{v^{z}B^{\varphi}-\frac{c^{2}\eta}{4\pi\mu}\frac{\partial B^{\varphi}}{\partial z}\right\}=0.
\end{aligned}
$$

In the Θ-pinch cylindrical symmetry case, we assume that the plasma current has an azimuth component only and is uniform along the φ-axis. At the same time, the current can have a gradient in the *r* and *z* directions. The magnetic field has only two projections in this ideal symmetric case: B^{r} and B^{z}. This idealization does not remove general plasma processes. The resulting equations for this case are as follows:

$$\frac{\partial \rho}{\partial t}+\frac{1}{r}\frac{\partial}{\partial r}\left(r\rho v^{r}\right)+\frac{\partial}{\partial z}\left(\rho v^{z}\right)=0$$

$$\frac{\partial \rho v^{r}}{\partial t}+\frac{1}{r}\frac{\partial}{\partial r}r\left(\rho v^{r}v^{r}-\frac{B^{r}B^{r}}{4\pi\mu}\right)+\frac{\partial}{\partial z}\left(\rho v^{r}v^{z}-\frac{B^{r}B^{z}}{4\pi\mu}\right)+\frac{\partial p_{tot}}{\partial r}=-\frac{B^{r}}{r4\pi\mu}\frac{\partial\left(rB^{r}\right)}{\partial r}-\frac{B^{r}}{4\pi\mu}\frac{\partial B^{z}}{\partial z}$$

$$\frac{\partial \rho v^{z}}{\partial t}+\frac{1}{r}\frac{\partial}{\partial r}r\left(\rho v^{z}v^{r}-\frac{B^{z}B^{r}}{4\pi\mu}\right)+\frac{\partial}{\partial z}\left(\rho v^{z}v^{z}+p_{tot}-\frac{B^{z}B^{z}}{4\pi\mu}\right)=-\frac{B^{z}}{r4\pi\mu}\frac{\partial\left(rB^{r}\right)}{\partial r}-\frac{B^{z}}{4\pi\mu}\frac{\partial B^{z}}{\partial z}$$

$$\frac{\partial e_{tot}}{\partial t}+\frac{1}{r}\frac{\partial}{\partial r}\left\{r\left[v^{r}\left(e_{tot}+p_{tot}\right)-\frac{B^{r}\left(B^{r}v^{r}+B^{z}v^{z}\right)}{4\pi\mu}+\frac{c^{2}\eta B^{z}}{16\pi^{2}\mu^{2}}\left(\frac{\partial B^{r}}{\partial z}-\frac{\partial B^{z}}{\partial r}\right)\right]\right\}+ \qquad (2.6.2)$$

$$+\frac{\partial}{\partial z}\left\{v^{z}\left[e_{tot}+p_{tot}\right]-\frac{B^{z}\left(B^{r}v^{r}+B^{z}v^{z}\right)}{4\pi\mu}-\frac{c^{2}\eta B^{r}}{16\pi^{2}\mu^{2}}\left(\frac{\partial B^{r}}{\partial z}-\frac{\partial B^{z}}{\partial r}\right)\right\}=$$

$$=-\frac{\left(B^{r}v^{r}+B^{z}v^{z}\right)}{r4\pi\mu}\frac{\partial\left(rB^{r}\right)}{\partial r}-\frac{\left(B^{r}v^{r}+B^{z}v^{z}\right)}{4\pi\mu}\frac{\partial B^{z}}{\partial z}$$

$$\frac{\partial B^{r}}{\partial t}+\frac{\partial}{\partial z}\left\{v^{z}B^{r}-B^{z}v^{r}-\frac{c^{2}\eta}{4\pi\mu}\left[\frac{\partial B^{r}}{\partial z}-\frac{\partial B^{z}}{\partial r}\right]\right\}=-v^{r}\left\{\frac{1}{r}\frac{\partial\left(rB^{r}\right)}{\partial r}+\frac{\partial B^{z}}{\partial z}\right\}$$

$$\frac{\partial B^{z}}{\partial t}+\frac{1}{r}\frac{\partial}{\partial r}\left\{r\left[v^{r}B^{z}-B^{r}v^{z}+\frac{c^{2}\eta}{4\pi\mu}\left(\frac{\partial B^{r}}{\partial z}-\frac{\partial B^{z}}{\partial r}\right)\right]\right\}=-v^{z}\left\{\frac{1}{r}\frac{\partial\left(rB^{r}\right)}{\partial r}+\frac{\partial B^{z}}{\partial z}\right\}.$$

3. Nonconvective Terms

The ideal MHD equation set (1.20) can be used to solve a limited physical problem such as a dense space plasma [10, 14, 15], to conduct theoretical investigations of instabilities [16-18] or to simplify real devices [19,20]. Key in modeling DPP or LPP devices, however, is representing the correct energy exchange and taking into account the main dissipative processes. It is essential to understand the transport processes, such as particle diffusion, heat conduction across the magnetic field, electric resistivity, and radiation transport. These processes occur as a result of plasma interactions, which may be described in terms of either binary collisions between particles or collective effects involving the scattering of particles by plasma waves. In general, the state of a fully ionized plasma of electrons and ions can be specified in terms of the velocity

distribution functions, which satisfy the kinetic equation for electrons and ions. In the approximation of no collisions, this equation is commonly referred to as the Vlasov or the collisionless Boltzmann equation. This description of ions and electrons in terms of distribution functions is often more detailed than is required. When the plasma is close to equilibrium, it is sufficient to describe the plasma in terms of macroscopic variables and the equation set (1.20). Additional nonconvective terms can be represented in the right side of the conservation law equations or transformed to additional dissipative fluxes. In the second case, Eq. (1.1) can be expanded to

$$\frac{\partial q}{\partial t} + \nabla \cdot \left(\mathbf{F}_q - \widetilde{\mathbf{F}}_q \right) = 0 , \tag{3.1}$$

where $\widetilde{\mathbf{F}}_q$ is the dissipative flux. At present, the HEIGHTS code includes three main dissipation sources: heat transport, magnetic diffusion, and radiation transport. The general MHD equation set taking into account these processes in Eq. (3.1) is given as

$$\begin{cases} \dfrac{\partial \rho}{\partial t} + \nabla \cdot \left(\rho \mathbf{v} \right) = 0 \\ \dfrac{\partial \rho \mathbf{v}}{\partial t} + \nabla \cdot \left(\rho \mathbf{v}\mathbf{v} + p_{tot} - \dfrac{\mathbf{B}\mathbf{B}}{4\pi\mu} \right) = -\dfrac{1}{4\pi\mu} \mathbf{B} \left(\nabla \cdot \mathbf{B} \right) \\ \dfrac{\partial e_{tot}}{\partial t} + \nabla \cdot \left[\mathbf{v} \left(e_{tot} + p_{tot} \right) - \dfrac{1}{4\pi\mu} \left(\mathbf{v} \cdot \mathbf{B} \right) \cdot \mathbf{B} + \dfrac{c^2 \eta}{16\pi^2 \mu^2} \left(\nabla \times \mathbf{B} \right) \times \mathbf{B} - \lambda \nabla T - \mathbf{S}_{rad} \right] = -\dfrac{1}{4\pi\mu} \left(\mathbf{v} \cdot \mathbf{B} \right) \cdot \left(\nabla \cdot \mathbf{B} \right) \\ \dfrac{\partial \mathbf{B}}{\partial t} + \nabla \cdot \left(\mathbf{v}\mathbf{B} - \mathbf{B}\mathbf{v} \right) + \dfrac{c^2}{4\pi\mu} \nabla \times \left(\eta \nabla \times \mathbf{B} \right) = -\mathbf{v} \left(\nabla \cdot \mathbf{B} \right), \end{cases} \tag{3.2}$$

where λ is thermal conductivity, η the resistivity, and $\mathbf{S}_{rad}$ the radiation flux. At first sight, the conservative equation set (3.2) can be easily solved with one of the numerous methods developed for the hyperbolic conservation law equations [10, 14, 15, 21]. However, direct use of convective hydrodynamic numerical schemes to (3.2) leads to nonphysical oscillations. The solutions can be obtained by use of time steps that are so small as to have no practical applications. The problem is that Eqs. (3.2) and (3.1) are not fully hyperbolic because the dissipative flux $\widetilde{\mathbf{F}}_q$ adds "parabolicity" to the system. A powerful approach that HEIGHTS utilizes for this problem is a

splitting method [22-24], which involves decoupling the full model into a separate component for each process, employing specialized numerical methods to solve each component, and coupling the resulting solutions. Thus, the MHD equations are solved as a decoupled set of hyperbolic and parabolic equations. At each time step Eq. (3.1) is split into decoupled subproblems (which may involve different meshes and solution methods) corresponding to the different physical processes (plasma flow, transport, diffusion, etc.) that occur within the computational domain or in individual regions.

The splitting algorithm has been used in the HEIGHTS numerical solution of Eq. (3.2) to separate the contributions from heat conduction, magnetic diffusion, and radiation transport. These processes redistribute internal energy and magnetic flux in the plasma.

3.1. Heat Conduction

Heat conduction in the plasma is one of the most important physical processes that should be taken into account when modeling experimental plasma behavior. Energy redistribution because of heat spread leads to major changes in the thermal conditions of real plasma devices. Decoupled from Eq. (3.2), the system heat conduction equation can be given as

$$\frac{\partial e}{\partial t} - \nabla \lambda \nabla T = 0 . \tag{3.1.1}$$

For the 3D case in a Cartesian grid, we can write this as follow:

$$\frac{\partial}{\partial t}\rho c_p T(t,x,y,z) - \frac{\partial}{\partial x}\lambda \frac{\partial}{\partial x} T(t,x,y,z) - \frac{\partial}{\partial y}\lambda \frac{\partial}{\partial y} T(t,x,y,z),$$
$$- \frac{\partial}{\partial z}\lambda \frac{\partial}{\partial z} T(t,x,y,z) = 0 , \tag{3.1.2}$$

where c_p is specific heat at constant pressure. With this parabolic equation, implicit numerical schemes are the most effective methods for obtaining results. However, these schemes have a

limiting factor and an appreciable disadvantage: they require extensive computer memory. Consideration of full 3D schemes is most critical. To avoid this problem the HEIGHTS code uses sparse matrix technology. The idea of excluding zero elements from the final linear equations matrix [25] is key to this theory.

We used a grid of gradually varying cell size by imposing unequal grid spacing $\Delta x_i = x_{i+1/2} - x_{i-1/2}$, $\Delta y_j = y_{j+1/2} - y_{j-1/2}$, and $\Delta z_k = z_{k+1/2} - z_{k-1/2}$ in the x, y, and z directions, respectively. The subscripts $i+1/2$, $j+1/2$, and $k+1/2$ refer to quantities defined on the cell interfaces $x_{i+1/2}$, $y_{j+1/2}$, and $z_{k+1/2}$. Cell centers $x_i = \left(x_{i+1/2} + x_{i-1/2}\right)/2$, $y_j = \left(y_{j+1/2} + y_{j-1/2}\right)/2$, and $z_k = \left(z_{k+1/2} + z_{k-1/2}\right)/2$ are specified at positions (i, j, k). We used standard notation for evaluating the function $T^n_{i,j,k}$ defined at cell centers (i, j, k) and time level n. We assumed time spacing t^n with intervals $\Delta t^n = t^{n+1} - t^n$. The spatial derivatives were approximated at each point (i, j, k) by using centered differences with truncation error of order $o = 2$.

The spatial derivative of temperature in the x-direction at x_i can be approximated as

$$\left(\frac{\partial}{\partial x}\lambda\frac{\partial}{\partial x}T(t,x,y,z)\right)_{i,j,k} = C_1^x T_{i-1,j,k} + C_2^x T_{i,j,k} + C_3^x T_{i+1,j,k} \qquad (3.1.3)$$

where

$$C_1^x = \frac{2\lambda_{i-1/2,j,k}}{\Delta x_i\left(\Delta x_{i-1} + \Delta x_i\right)},\ C_2^x = -\frac{2\left[\lambda_{i+1/2,j,k}\left(\Delta x_{i-1} + \Delta x_i\right) + \lambda_{i-1/2,j,k}\left(\Delta x_{i+1} + \Delta x_i\right)\right]}{\Delta x_j\left(\Delta x_{i-1} + \Delta x_i\right)\left(\Delta x_{i+1} + \Delta x_i\right)},$$

$$C_3^x = \frac{2\lambda_{i+1/2,j,k}}{\Delta x_i\left(\Delta x_{i+1} + \Delta x_i\right)}.$$

Analogous approximation along the y- and z-axes follows after reduction to the common expression:

$$A_{i,j,k-1}T^{n+1}_{i,j,k-1} + A_{i,j-1,k}T^{n+1}_{i,j-1,k} + A_{i-1,j,k}T^{n+1}_{i-1,j,k} + A_{i,j,k}T^{n+1}_{i,j,k} + A_{i+1,j,k}T^{n+1}_{i+1,j,k} + A_{i,j+1,k}T^{n+1}_{i,j+1,k} + A_{i,j,k+1}T^{n+1}_{i,j,k+1} = D_{i,j,k}, \quad (3.1.4)$$

where the coefficients are

$$A_{i,j,k-1} = \frac{\lambda_{i,j,k-1/2}}{\Delta z_k\left(\Delta z_{k-1} + \Delta z_k\right)}, \qquad A_{i,j-1,k} = \frac{\lambda_{i,j-1/2,k}}{\Delta y_j\left(\Delta y_{j-1} + \Delta y_j\right)}, \qquad A_{i-1,j,k} = \frac{\lambda_{i-1/2,j,k}}{\Delta x_i\left(\Delta x_{i-1} + \Delta x_i\right)},$$

$$A_{i,j,k} = -\left\{ \begin{array}{l} \dfrac{c^n_{i,j,k}\rho^n_{i,j,k}}{2\Delta t^n} + \dfrac{\lambda_{i,j,k-1/2}}{\Delta z_k\left(\Delta z_{k-1} + \Delta z_k\right)} + \dfrac{\lambda_{i,j,k+1/2}}{\Delta z_k\left(\Delta z_{k+1} + \Delta z_k\right)} + \dfrac{\lambda_{i,j-1/2,k}}{\Delta y_j\left(\Delta y_{j-1} + \Delta y_j\right)} + \\ + \dfrac{\lambda_{i,j+1/2,k}}{\Delta y_j\left(\Delta y_{j+1} + \Delta y_j\right)} + \dfrac{\lambda_{i-1/2,j,k}}{\Delta x_i\left(\Delta x_{i-1} + \Delta x_i\right)} + \dfrac{\lambda_{i+1/2,j,k}}{\Delta x_i\left(\Delta x_{i+1} + \Delta x_i\right)} \end{array} \right\},$$

$$A_{i,j,k+1} = \frac{\lambda_{i,j,k+1/2}}{\Delta z_k\left(\Delta z_{k+1} + \Delta z_k\right)}, \quad A_{i,j+1,k} = \frac{\lambda_{i,j+1/2,k}}{\Delta y_j\left(\Delta y_{j+1} + \Delta y_j\right)}, \quad A_{i+1,j,k} = \frac{\lambda_{i+1/2,j,k}}{\Delta x_i\left(\Delta x_{i+1} + \Delta x_i\right)} \text{ and}$$

$$D_{i,j,k} = -\frac{c^n_{i,j,k}\rho^n_{i,j,k}T^n_{i,j,k}}{2\Delta t^n}.$$

Equation (3.1.4) can be rewritten in simple matrix form as

$$\mathbf{A}\cdot\mathbf{T} = \mathbf{D}. \tag{3.1.5}$$

We assume that the plasma parameters do not change during one time step; the linear equations include specific heat $c^n_{p\{i,j\}}$ and density $\rho^n_{i,j}$ with *n* time steps. Equation (3.1.5) is a closed system, where the number of unknown values equals the number of linear equations if the boundary conditions are determined. In general, boundary conditions on any border Γ are given by $\alpha\lambda\nabla T\big|_\Gamma + \beta T\big|_\Gamma = f\left(T\big|_\Gamma, t\right)$, where the numerical parameters α and β specify the situation at the Γ border for given a heat flux (α = 1, β = 1), given temperature (α = 0, β = 1), or heat flux as a function of temperature. The simplest case of thermally isolated borders can be realized as

equivalences $\left.\frac{\partial T}{\partial x}\right|_{\Gamma(x=const)}=0$, $\left.\frac{\partial T}{\partial y}\right|_{\Gamma(y=const)}=0$, and $\left.\frac{\partial T}{\partial z}\right|_{\Gamma(z=const)}=0$. A more comprehensive discussion of boundary conditions is presented in [26]. Numerical simulation with the implicit scheme is unconditionally stable, and in combined schemes the limiting factor on the time step is usually the explicit part (the convection stage in our case). Ideal MHD calculations demand Courant-Friedrich-Levi conditions for the explicit algorithm [27]. In the heat conduction equation the time step limiter can be used: $\Delta t \sim \min\left|\frac{\Delta x^2 c_p \rho}{2\lambda}\right|$, where Δx is the minimal cell size.

In Fig. 3, we present the matrix expression for the heat conduction equation in the simplest 3 × 3 × 3 domain, where zero elements are shown as empty cells. The linear system is sparse and seven-diagonal. The coefficient matrix size is n·m·k × n·m·k × n·m·k, where n, m, and k are the cell amounts along the x-, y-, and z-axes. In our LPP problem, the largest grid size was 60 × 60 × 60 cells, which produces a coefficient matrix of about $1.0 \cdot 10^{16}$ elements. This large sparse matrix has an extremely large number of zero elements. The structure of the matrix is invariable, with linear equations that describe nonuseful cells. Key to computational efficiency is to store and operate on only nonzero entries of the matrix. Several mathematic libraries (e.g., NAG, IMSL, and PARDISO) are used for solution of linear equation systems with a band or sparse matrix. MUMPS and SuperLU codes allow parallel solution of the system of linear equations given in (3.1.5) [28]. Calculations for the complex domain need special code for implementation of boundary conditions and exclusion of nonuseful domain areas. If the computational domain does not change during the simulation time (no motion of any device walls), the best calculational method is to analyze the domain form before the start of the main computer program, and to prepare templates of needed matrices. In contrast to the explicit algorithm, where it is possible to

have a separate module of boundary conditions, the implicit code requires embedding of the linear coefficients **A** and **D** during construction of matrices **A** and **D**.

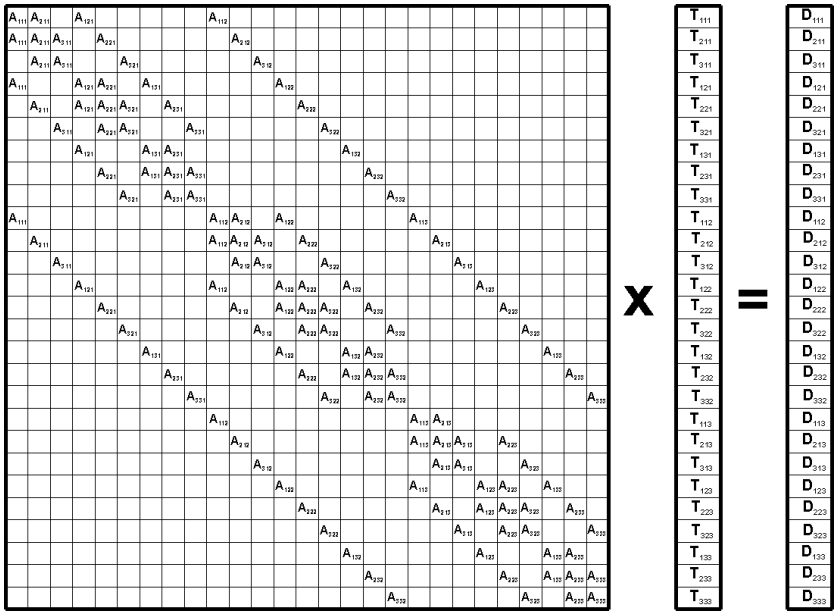

Fig. 3. Detail matrix construction for domain 3 × 3 × 3. Empty cells correspond to zero elements.

3.2. Magnetic Diffusion and Magnetic Source

The magnetic diffusion equation is similar to the heat conduction equation:

$$\frac{\partial \mathbf{B}}{\partial t} + \frac{c^2}{4\pi\mu}\nabla \times \left(\eta \nabla \times \mathbf{B}\right) = 0\,. \qquad (3.2.1)$$

The three-dimensional case has no discontinuities and can be solved analogously to the heat conduction, Section 3.1. The 2D cylindrical geometry is more complicated because of the discontinuity at $r = 0$. An implicit numerical method is considered in this section for application

to cylindrical geometry and to the problem of the discontinuity at the zero point. Following the equation set in Section 2.5, we can give Eq. (3.2.1) for this case as

$$\frac{\partial}{\partial t}B(t,r,z)-\frac{\partial}{\partial r}\frac{c^2\eta}{4\pi r}\frac{\partial}{\partial r}rB(t,r,z)-\frac{\partial}{\partial z}\frac{c^2\eta}{4\pi}\frac{\partial}{\partial z}B(t,r,z)=0, \tag{3.2.2}$$

where the magnetic field B has one component along the φ-axis. The first space derivation term in this equation can be approximated as

$$\left(\frac{\partial}{\partial r}\frac{\eta}{r}\frac{\partial}{\partial r}rB(t,r,z)\right)_{i,j} = C_1^r B_{i-1,j}+C_2^r B_{i,j}+C_3^r B_{i+1,j}, \tag{3.2.3}$$

where

$$C_1^r=\frac{2\eta_{i-1/2,j}r_{i-1}}{r_{i-1/2}\Delta r_i\left(\Delta r_{i-1}+\Delta r_i\right)},\ C_2^r=-\left[\frac{2\eta_{i+1/2,j}r_i}{r_{i+1/2}\Delta r_i\left(\Delta r_i+\Delta r_{i+1}\right)}+\frac{2\eta_{i-1/2,j}r_i}{r_{i-1/2}\Delta r_i\left(\Delta r_{i-1}+\Delta r_i\right)}\right],$$

$$C_3^r=\frac{2\eta_{i+1/2,j}r_{i+1}}{r_{i+1/2}\Delta r_i\left(\Delta r_i+\Delta r_{i+1}\right)} \text{ for } r_{i-1/2}\neq 0 \text{, i.e., } i>1.$$

The linear coefficients in Eq. (3.2.3) cannot be determined if $r_{i\pm1/2}=0$. In other words, the magnetic field derivation is not defined at the zero point. However, the requirement of the equivalence of the left- and right-side derivatives and the calculation of the limit to zero yield a full description of the numerical function behavior near the singularity point $B\big|_{r=0}=0$, $\left.\frac{\partial B}{\partial r}\right|_{+}=-\left.\frac{\partial B}{\partial r}\right|_{-}$:

$$\lim_{r\to 0}\frac{c^2\eta}{4\pi\mu r}\frac{\partial rB}{\partial r}=\frac{c^2\eta}{2\pi\mu}\lim_{r\to 0}\frac{\partial B}{\partial r}. \tag{3.2.4}$$

Implementation of Eq. (3.2.4) conditions in (3.2.3) provides coefficients for the first cell of the computational domain:

$$C_1^r = 0,\ C_2^r = -\left[\frac{2\eta_{3/2,j} r_1}{r_{3/2}\Delta r_1\left(\Delta r_1 + \Delta r_2\right)} + \frac{4\eta_{1/2,j}}{\Delta r_1^2}\right],\ C_3^r = \frac{2\eta_{3/2,j} r_2}{r_{3/2}\Delta r_1\left(\Delta r_1 + \Delta r_2\right)} \text{ for } i = 1. \quad (3.2.5)$$

The second space derivation term (z-axis) in Eq. (3.2.2) has no exclusions and can be solved similarly to heat conduction

$$\left(\frac{\partial}{\partial z}\eta\frac{\partial}{\partial z}B(t,r,z)\right)_{i,j} = C_1^z B_{i,j-1} + C_2^z B_{i,j} + C_3^z B_{i,j+1}, \quad (3.2.6)$$

where

$$C_1^z = \frac{2\eta_{i,j-1/2}}{\Delta z_j\left(\Delta z_{j-1} + \Delta z_j\right)},\ C_2^z = -\frac{2\left[\eta_{i,j+1/2}\left(\Delta z_{j-1} + \Delta z_j\right) + \eta_{i,j-1/2}\left(\Delta z_{j+1} + \Delta z_j\right)\right]}{\Delta z_j\left(\Delta z_{j-1} + \Delta z_j\right)\left(\Delta z_{j+1} + \Delta z_j\right)},$$

$$C_3^z = \frac{2\eta_{i,j+1/2}}{\Delta z_j\left(\Delta z_{j+1} + \Delta z_j\right)}.$$

Finally, after transformations, Eq. (3.2.2) can be represented as a linear equation system:

$$A_{i-1,j}B_{i-1,j}^{n+1} + A_{i,j}B_{i,j}^{n+1} + A_{i+1,j}B_{i+1,j}^{n+1} + A_{i,j-1}B_{i,j-1}^{n+1} + A_{i,j+1}B_{i,j+1}^{n+1} = D_{i,j}, \quad (3.2.7)$$

where coefficients A and D are calculated from corresponding C:

$$A_{i-1,j} = C_1^r,\ A_{i,j} = C_2^r + C_2^z - \frac{4\pi\mu}{\Delta t^n c^2},\ A_{i+1,j} = C_3^r,\ A_{i,j-1} = C_1^z,\ A_{i,j+1} = C_3^z, \qquad (3.2.8)$$

$$D_{i,j} = -\frac{4\pi\mu B_{i,j}^n}{\Delta t^n c^2}.$$

The time steps for implicit magnetic diffusion algorithms are discussed in [29]. Conditions on the external borders of the domain are determined by various physical processes. Most useful are the following: current $B\big|_\Gamma = 2I/rc$; symmetry $\left.\frac{\partial rB}{\partial r}\right|_{\Gamma(r=const)} = 0$, $\left.\frac{\partial B}{\partial z}\right|_{\Gamma(z=const)} = 0$; and conducting wall $B\big|_\Gamma = 0$.

The self-generated magnetic fields in laser-produced plasmas are of much theoretical and experimental interest because of their role in the design of inertial confinement fusion targets [30-32]. Interest in this area arises from the large number of transport characteristics (e.g., thermal transport, lateral plasma flow, and fast plasma blowoff), which affect the performance of the target. These, in turn, are related to the properties of large-scale magnetic fields generated in the system. Based on these properties, the HEIGHTS package takes into account the magnetic field source term in the Faraday equation (1.17b):

$$\frac{\partial \mathbf{B}}{\partial t} + \nabla\cdot(\mathbf{vB} - \mathbf{Bv}) + \frac{c^2}{4\pi\mu}\nabla\times(\eta\nabla\times\mathbf{B}) + \frac{ck_B}{en_e}\nabla n_e\times\nabla T_e = -\mathbf{v}(\nabla\cdot\mathbf{B}). \qquad (3.2.9)$$

Here, n_e and T_e are the concentration and temperature of electrons. Numerical simulations have been undertaken to investigate the influence of the self-generated magnetic field on plasma parameters and on the EUV output for a laser radiation power of $10^{11} - 10^{12}$ W/cm^2. Numerical simulations of the LPP device with droplet and planar targets showed a very small dependence of the plasma parameters on the thermomagnetic source for the laser radiation power [11].

3.3. Radiation Transport

Data obtained for the temperature and radiation flux fields in star photospheres was applied to the calculation of star luminance [33]. Radiation transport theory was created on the basis of this classical problem, from which numerical methods and approximations of the radiation transport equation solution were developed [34]. Stationary stars are huge gaseous objects that are heated from several thousands degrees on their surface up to millions in the center. Massive heated gaseous spheres of that kind radiate only from their surface. Gas in the star body is optically very thick, and space around the star is optically very thin. This situation enables a simple approximation of the radiation transport equation: diffusion approximation, radiative heat conduction, forward-reverse, and so forth. A laboratory plasma has a specific place in this regard. Such a plasma is usually a nonstationary object, where an intermediate variant is present: not thick and not thin optically. Simple approximations are invalid as a rule for most practical applications. Advanced physical models and numerical methods should be applied to obtaining correct results. The HEIGHTS system uses two approaches: direct Gauss integration of the radiation transport equation and a Monte Carlo model with a weight factor hierarchy. Direct solution of the radiation transport equation is more correct in a certain sense but has a serious disadvantage: it is very expensive. Thus, it is applied only as a test for Monte Carlo calculations.

Direct Gauss Integration. The main goal of this method is to obtain the radiation flux in every cell of the MHD mesh and its divergence:

$$Q_{rad} = \nabla \cdot \vec{S}_{rad} . \qquad (3.3.1)$$

The divergence indicates the loss of radiation energy in some cells and adding of radiation energy in other cells. Radiation flux is integrated by a spectrum (or quantum of energy) and is an angular variable. It depends on the distribution of thermodynamic parameters (temperature and density) in the entire volume under consideration:

$$\vec{S} = \int_0^\infty \vec{S}_E \, dE , \qquad \vec{S}_E = \int_{4\pi} I_E \, \vec{\Omega} \, d\vec{\Omega} , \qquad (3.3.2)$$

where I_E is the spectral radiation intensity and $\vec{\Omega}$ is a unit vector in the direction of quanta distribution s. Suppose n is a normal vector to the unit element, which quanta cross (see Fig. 4). The projection of the radiation flux vector onto n is

$$S_E = \int_{(4\pi)} I_E \cos\theta \, d\Omega . \qquad (3.3.3)$$

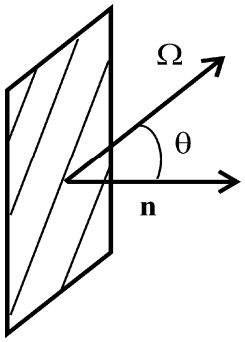

Fig. 4. Integration scheme.

For the solid angle $d\Omega = \sin\theta \, d\theta \, d\varphi$, it is possible to obtain the expression:

$$S_E = \int_0^{2\pi} d\varphi \int_0^{\pi} I_E(\varphi,\theta)\cos\theta \sin\theta \, d\theta ,$$

where φ and θ are the angles that determine the direction of the quanta distribution.

In the case of cylindrical symmetry, the spectral flux at the point with coordinates r_0 and z_0 is described by the expression

$$S_E = 2\int_0^{\pi} d\varphi \int_0^{\pi} I_E(\varphi,\theta)\cos\theta \sin\theta \, d\theta , \qquad (3.3.4a)$$

where the symmetry of the quanta distribution on the corner φ is taken into account. Here, φ is the angle between the projection of the direction s to the plane, perpendicular to the z-axis and normal to the cylindrical surface; and θ is the angle between the direction s and the z-axis (Fig. 5).

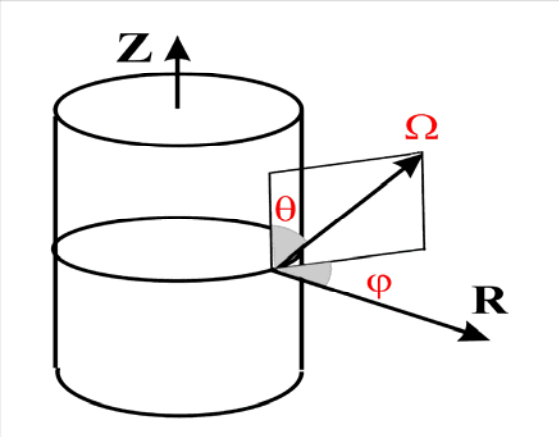

Fig. 5. Cylindrical geometry case.

For projections of the radiation flux on the radial *r*- and axial *z*-axis we have

$$S_{RE}(r_0, z_0) = 2\int_0^{\pi} d\varphi \int_0^{\pi} \cos\varphi \sin^2\theta \, I_E(r_0, z_0, \varphi, \theta) d\theta \,, \qquad (3.3.4b)$$

$$S_{ZE}(r_0, z_0) = 2\int_0^{\pi} d\varphi \int_0^{\pi} \cos\theta \sin\theta \, I_E(r_0, z_0, \varphi, \theta) d\theta \,. \qquad (3.3.4c)$$

The spectral radiation intensity $I_E(r_0, z_0, \varphi, \theta)$ is found from the solution of the radiation transport equation (RTE):

$$\frac{dI_E}{ds} = k_{Eemi} I_{Ep} - k_{Eabs} I_E \,. \qquad (3.3.5)$$

Here, κ_{Eabs} is a spectral absorption coefficient for quanta with energy E, κ_{Eemi} is a spectral emission coefficient, I_E is the spectral intensity, and I_{Ep} is the spectral equilibrium intensity. RTE represents the energy conservation law for the radiation intensity. The equilibrium intensity I_{Ep} is defined by the Planck function:

$$I_{Ep} = \frac{\hbar\omega^3}{4\pi^2c^2}\cdot\frac{1}{e^{\frac{\hbar\omega}{\kappa T}}-1} = \frac{\hbar^3\omega^3}{4\pi^2c^2\hbar^2}\cdot\frac{1}{e^{\frac{\hbar\omega}{\kappa T}}-1} = \frac{1}{4\pi^2c^2\hbar^2}\cdot E^3(e^{\frac{E}{\kappa T}}-1)^{-1}, \text{ or}$$

$$I_{Ep} = \frac{\kappa^3T^3}{4\pi^2c^2\hbar^2}\cdot\frac{E^3}{\kappa^3T^3}(e^{\frac{E}{\kappa T}}-1)^{-1} = \frac{\kappa^3T^3}{4\pi^2c^2\hbar^2}\cdot x^3(e^x-1)^{-1}, \text{ where } x=\frac{E}{\kappa T}. \quad (3.3.6)$$

Equation (3.3.5) is a one-dimensional differential equation relative to the intensity along the ray of the quanta distribution. A formal solution of a Cauchy problem is given for this equation:

$$I_E(s) = I_E(s_0)\exp\{-\int_{s_0}^{s} k_{Eabs}(s')ds'\} + \int_{s_0}^{s} I_{Ep}(s')k_{Eemi}(s')\exp\{-\int_{s'}^{s} k_{Eabs}(s'')ds''\}ds' \ , \quad (3.3.7)$$

which expresses the fact that the intensity at any point in a given direction is the result of the emission at all anterior points s', reduced by the factor $\exp\{-\int_{s_0}^{s} k_{Eabs}(s')ds'\}$ to allow for absorption by intervening matter.

The RTE solution is determined by the temperature and density on the ray (they determine the spectral coefficients and the equilibrium intensity) and does not depend on the geometry of the plasma.

Equation (3.3.5) can be written as

$$\frac{dI_E}{ds} = \kappa_{abs}\left(\frac{\kappa_{emi}}{\kappa_{abs}}I_{Ep} - I_E\right) \text{ or } \frac{dI_E}{d\tau} = \frac{\kappa_{emi}}{\kappa_{abs}}I_{Ep} - I_E \quad (3.3.8)$$

where $d\tau = k_{abs}ds$. This leads to

$$I_E(\tau) = I_E(\tau_0)\exp\{-\int_{\tau s_0}^{\tau} d\tau'\} + \int_{\tau_0}^{\tau}\frac{k_{emi}(\tau')}{k_{abs}(\tau')}I_{Ep}(\tau')\exp\{-\int_{\tau'}^{\tau} d\tau''\}d\tau' \ . \quad (3.3.9)$$

The numerical approximation of Eq. (3.3.9) was obtained by discretization of the integration half-lines. At the same time, we assume that the changing of temperature and density (and

accordingly, the spectral coefficients) is insignificant within the one-cell boundaries. Then, the spectral intensity value on the observation ray is found by integration of values in the cells using

$$I_E(\tau_i) = I_E(\tau_{i-1})e^{-(\tau_i-\tau_{i-1})} + \frac{k_{emi}(\tau_i)}{k_{abs}(\tau_i)} \int_{\tau_{i-1}}^{\tau_i} I_{Ep}(\tau')\exp\{-\int_{\tau'}^{\tau_i} d\tau''\}d\tau' ,$$

from which

$$I_E(\tau_i) = I_E(\tau_{i-1})e^{-(\tau_i-\tau_{i-1})} + \frac{k_{emi}(\tau_i)}{k_{abs}(\tau_i)} \int_{\tau_{i-1}}^{\tau_i} I_{Ep}(\tau')\, d\left\{\exp\{-\int_{\tau'}^{\tau_i} d\tau''\}\right\}.$$

Integrating yields

$$I_E(\tau_i) = I_E(\tau_{i-1})e^{-(\tau_i-\tau_{i-1})} + \frac{k_{emi}(\tau_i)}{k_{abs}(\tau_i)}\left[I_{Ep}(\tau_i) - I_{Ep}(\tau_{i-1})\, e^{-(\tau_i-\tau_{i-1})} - \int_{\tau_{i-1}}^{\tau_i} \exp\{-\int_{\tau'}^{\tau_i} d\tau''\}\, dI_{Ep}(\tau')\right]$$

and

$$I_E(\tau_i) = I_E(\tau_{i-1})e^{-(\tau_i-\tau_{i-1})} + \frac{k_{emi}(\tau_i)}{k_{abs}(\tau_i)}\left[I_{Ep}(\tau_i) - I_{Ep}(\tau_{i-1})\, e^{-(\tau_i-\tau_{i-1})} - \int_{\tau_{i-1}}^{\tau_i} \exp\{-\int_{\tau'}^{\tau_i} d\tau''\}\, (I_{Ep}(\tau'))' d\tau'\right].$$

In view of the chosen discretization, the Planck function derivative is a constant value in each cell. Thus,

$$I_E(\tau_i) = I_E(\tau_{i-1})e^{-\Delta\tau_i} + \frac{k_{emi}(\tau_i)}{k_{abs}(\tau_i)}\left[I_{Ep}(\tau_i) - I_{Ep}(\tau_{i-1})\, e^{-\Delta\tau_i} - \frac{I_{Ep}(\tau_i) - I_{Ep}(\tau_{i-1})}{\Delta\tau_i}\left(1 - e^{-\Delta\tau_i}\right)\right]. \quad (3.3.10)$$

Here $\Delta\tau_i = \tau_i - \tau_{i-1} = \kappa_{abs}(s_i - s_{i-1})$ is the optical absorption thickness of the cell for quanta with energy E.

Using Eq. (3.3.10), we can calculate the spectral intensity along the radiation ray. Next, we derive the spectral components of the radiation flux in the point. All quanta of energies must be integrated to find the total components of the radiation flux:

$$S_R(r_0,z_0)=\int_0^\infty S_{RE}(r_0,z_0)dE \quad , \qquad S_Z(r_0,z_0)=\int_0^\infty S_{ZE}(r_0,z_0)dE \, .$$

Taking into consideration Eqs. (3.3.4b) and (3.3.4c), we obtain

$$S_R(r_0,z_0)=2\int_0^\pi d\varphi \int_0^\pi \cos\varphi \sin^2\theta \left[\int_0^\infty I_E(r_0,z_0,\varphi,\theta)dE\right] d\theta \, , \tag{3.3.11}$$

$$S_Z(r_0,z_0)=2\int_0^\pi d\varphi \int_0^\pi \cos\theta \sin\theta \left[\int_0^\infty I_E(r_0,z_0,\varphi,\theta)dE\right] d\theta \, . \tag{3.3.12}$$

Integration by Spectrum: The total radiation flux in the point is found by angular integration of the total intensity values from Eqs. (3.3.11) and (3.3.12). The total intensity is the result of integrating by the energy quanta:

$$I=\int_0^\infty I_E(r_0,z_0,\varphi,\theta)dE$$

The energy spectrum grouping is used to obtain a numerical approximation of the last integral solution. Each group E_k is defined by the boundary values of energy quanta E_k и E_{k+1} and the mean group absorption and emission coefficients. Then, the total radiation intensity is found by summation of the intensity values, obtained for the spectral groups:

$$I=\sum_k \int_{E_k}^{E_{k+1}} I_E(r_0,z_0,\varphi,\theta)dE \, .$$

Based on Eq. (3.3.9), we integrate the Planck function for each group by its boundary values:

$$I_{E_k p} = \int_{E_k}^{E_{k+1}} \frac{\kappa^3 T^3}{4\pi^2 c^2 \hbar^2} \cdot \frac{x^3}{e^x - 1} dE = \frac{\kappa^4 T^4}{4\pi^2 c^2 \hbar^2} \int_{E_k}^{E_{k+1}} \frac{x^3}{e^x - 1} dx \,. \qquad (3.3.13)$$

Estimation of the quantum energy, which can be ignored with a given error (~ 10^{-4}) is carried out to reduce the calculation time before integrating the intensity along the ray. The following inequality can be used:

$$\int_{E_k}^{\infty} I_{Ep} dE < 10^{-4} \int_0^{\infty} I_{Ep} dE \,, \text{ or } \quad \int_{E_k}^{\infty} \frac{x^3 dx}{e^x - 1} < 10^{-4} \int_0^{\infty} \frac{x^3 dx}{e^x - 1} \,.$$

Maximal value of temperature T_{max} along the ray is found for that inequality. The approximate integral value is calculated as $\int_0^{\infty} \frac{x^3 dx}{e^x - 1} = \frac{\pi^4}{15}$, from which it follows that

$$\frac{15}{\pi^4} \int_{x_k}^{\infty} \frac{x^3 dx}{e^x - 1} \approx \frac{15}{\pi^4} e^{-x_k} \left[x_k^3 + 3x_k^2 + 6x_k + 6 \right] < 10^{-4} \text{, where } \; x_k = \frac{E_k}{T_{\max}} \,. \qquad (3.3.14)$$

This estimation allows us to determine the energy group and all following energy groups whose contributions are less than 10^{-4}. These groups are not taken into account when the intensity integration along the ray is carried out. Tables of absorption and emission coefficients with the detailed resolution on the quanta energy, density, and temperature are used when the intensity for the spectral group is calculated.

Integration by Ray: We need to know the temperature and density distributions on the ray to calculate the intensity along the half-line from Eq. (3.3.10). For this reason, the ray is divided into equal cells Δl from the starting point (r_0, z_0) to the exit from the hydrodynamic mesh. We assume that the change of temperature and density (and accordingly, the spectral coefficients) is insignificant within the bounds of one cell. In the first step the coordinates of the boundary points are calculated relative to the *r*- and *z*-axes. The coordinates depend on the angles φ and θ (they determine the ray direction). The *z*-coordinate can be obtained next. Since the distance from the

ray starting point (r_0, z_0) to point (r_i, z_i) is equal to $\Delta l * i$ and since the z_0 coordinate is known, for angle $0 < \theta < \frac{\pi}{2}$ (Fig. 6),

$$z_i = |BZ_i| = |AZ_0| + |CZ_i| = |AZ_0| + |Z_0Z_i| * \cos\theta = z_0 + \Delta l * i * \cos\theta .$$

For angle $\frac{\pi}{2} < \theta < \pi$ (Fig. 7),

$$z_i = |BZ_i| = |AZ_0| - |CZ_0| = |AZ_0| - |Z_0Z_i| * \cos\theta = z_0 - \Delta l * i * \cos\theta .$$

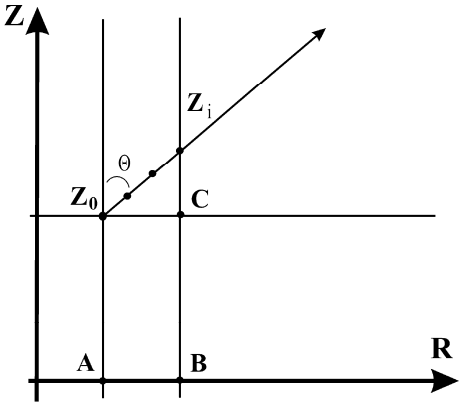

Fig. 6. z-coordinate for $0 < \theta < \frac{\pi}{2}$.

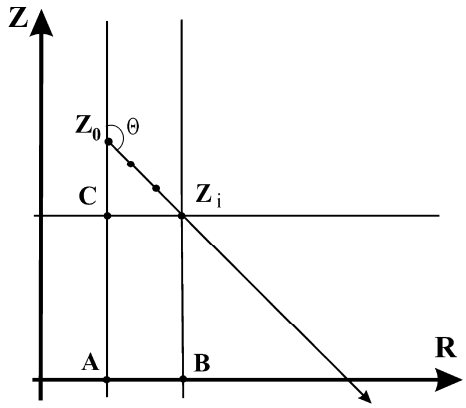

Fig.7. z-coordinate for $\frac{\pi}{2} < \theta < \pi$.

The *r*-coordinate is calculated in the next step. It is needed to obtain the projection of the segment $|Z_0Z_i|$ onto the $r\varphi$- plane: $|R_0R_i| = \Delta l * i * \sin\theta$. The $|R_0B|$ distance is given by $|R_0B| = \sqrt{|OR_0|^2 - |OB|^2}$, where $|OB|$ is the nearest distance from the coordinate center to the ray (Figs. 8 and 9): $|OB| = |OR_0| * \sin\varphi$. Then, for $0 < \varphi < \frac{\pi}{2}$ (Fig. 8) $|BR_i| = |R_0B| + |R_0R_i|$.

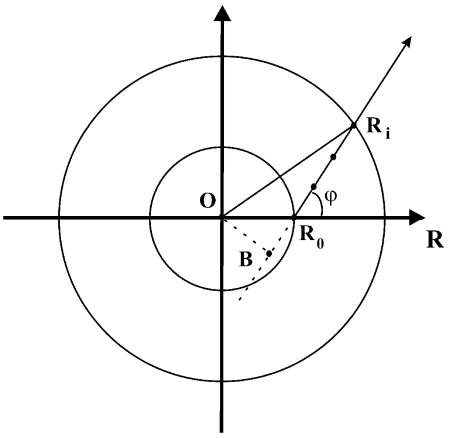

Fig. 8. Ray expansion for $0 < \varphi < \frac{\pi}{2}$.

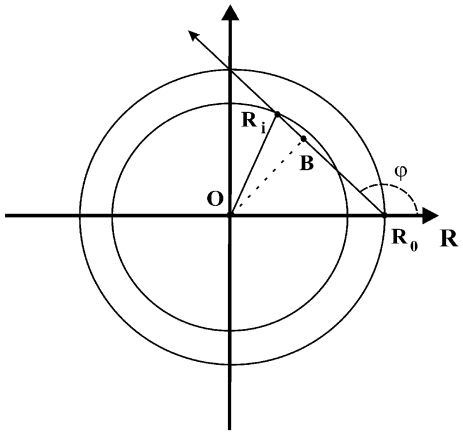

Fig. 9. Ray expansion for $\frac{\pi}{2} < \varphi < \pi$.

For $\frac{\pi}{2} < \varphi < \pi$ (Fig. 9), depending on the location of the point r_i, we have $|BR_i| = |R_0 B| - |R_0 R_i|$ or $|BR_i| = |R_0 R_i| - |R_0 B|$. Now, we find the *r*-coordinate of the point by using the distances $r_i = |OR_i| = \sqrt{|OB|^2 + |BR_i|^2}$.

Knowing the point coordinates allows us to determine the temperature and density values by using the MHD plasma parameters at these cell points. Next, we determine which cell of the hydrodynamic mesh the point belongs to. As assumed earlier, temperature and density in the bounds of one cell are constant. From this MHD data we can calculate absorption and emission coefficients in the ray points (from the tables) and obtain the equilibrium intensity. Then, the intensity by the observation ray is calculated with Eq. (3.3.10).

Integration by Angles: The total intensity is integrated by the angles φ and θ within the ranges $0 \le \varphi \le \pi$ and $0 \le \theta \le \pi$. The total components of the radiation flux are calculated in the point by Eqs. (3.3.11) and (3.3.12). Integrals over angles are approximated by the Gauss quadrature method:

$$A = \int_a^b f(x)dx = \frac{b-a}{2}\int_{-1}^{1} f(\xi)d\xi = \frac{b-a}{2}\sum_i f(\xi_i)C_i \,. \qquad (3.3.15)$$

Here, C_i are weights of the Gauss quadrature, and $\xi_{i,j}$ are abscissas (changing from -1 up to 1). The splitting is carried out at nodal values φ_i and θ_j equal to $\varphi_i = \frac{\pi}{2}(1+\xi_i)$ and $\theta_j = \frac{\pi}{2}(1+\xi_i)$.

Expressions for calculating the flux components are written with Eq. (3.3.15) as follows:

$$S_R(r_0, z_0) = \frac{\pi^2}{2} \sum_i C_i \sum_j \cos\varphi \sin^2\theta \, I(r_0, z_0, \xi_i, \xi_j) \, C_j, \tag{3.3.16}$$

$$S_Z(r_0, z_0) = \frac{\pi^2}{2} \sum_i C_i \sum_j \cos\theta \sin\theta \, I(r_0, z_0, \xi_i, \xi_j) \, C_j. \tag{3.3.17}$$

The HEIGHTS code can vary in order of angular quadrature. Depending on the given order of Gauss quadrature, the integration can be carried out by 8, 12, 16, 20, 24, 32, 64, 80, or 96 points of an angular grid. Accordingly, the total flux value in each point is calculated by integration of the intensity in the direction of 64, 144, 400, 576, 1024, 4096, 6400 or 9216 observation rays, going out from the point. The angular integration accuracy increases with increasing order of Gauss. But the calculation time increases greatly, too. Abscissas and weights for integration by Gauss quadrature are determined in advance and are kept in the tables of values in the positive half-range, from which the arrays of values in the range from -1 to 1 are generated.

Sequential Algorithm of the Radiation Flux: To take into account heat radiation energy redistribution, the MHD task includes calculation of the radiation flux and its divergence based on current temperature and density field. The MHD task is solved in two-dimensional space, but the radiation flux is calculated in a 3D volume. However in consequence of the cylindrical symmetry HEIGHTS algorithm can use the grid partitioning of two-dimensional MHD space in the procedure of the radiation flux calculating and we can get the flux values in central points of the hydrodynamic mesh.

Solving the problem is divided into subtasks:

1. Input initial data – the size of MHD mesh, the optical characteristics tables (energy groups bounds, absorption and emission coefficients), the order of Gauss quadrature.

2. Initialization of the workspace – the construction of calculation mesh, which is similar to the MHD mesh, the preparation of the abscissas and weights arrays in compliance with chosen order of Gauss quadrature.
3. Organization of the cycle for the radiation flux components calculating in central points of all mesh cells by *z*-axial and *r*-radial axis. It includes the following:
    - Determination of the thermodynamic parameters distribution on the ray, going out from central point (r_0, z_0) on given angles φ_i, θ_j (temperature $T(r_0, z_0, \varphi_i, \theta_j)$ and density $\rho(r_0, z_0, \varphi_i, \theta_j)$).
    - Obtaining of the necessary integration limits by quanta energy E_{max}, depending on maximal temperature on the ray $T_{max}(r_0, z_0, \varphi_i, \theta_j)$ using (3.3.14).
    - Calculation of the equilibrium intensity values for each spectral group by (3.3.13) and the intensity integration $I_{Ek} (r_0, z_0, \varphi_i, \theta_j)$ by the ray at point (r_0, z_0) using (3.3.10).
    - Integration of the intensity by the energy groups:

      $$I(r_0, z_0, \varphi_i, \theta_j) = \sum_{k=1}^{N} I_{E_k}(r_0, z_0, \varphi_i, \theta_j)$$

    - Integration of the intensity by the angles using (3.3.16) and (3.3.17):

      $$S_R(r_0, z_0) = \frac{\pi^2}{2} \sum_i C_i \sum_j \cos\varphi \sin^2\theta \; I\;(r_0, z_0, \xi_i, \xi_j)\, C_j$$

      $$S_Z(r_0, z_0) = \frac{\pi^2}{2} \sum_i C_i \sum_j \cos\theta \sin\theta \; I\;(r_0, z_0, \xi_i, \xi_j)\, C_j$$

4. Calculation of the flux divergence, taking into account the cylindrical symmetry by formula: $\nabla \cdot \vec{S} = \frac{1}{r}\frac{\partial}{\partial r}(rS_R) + \frac{\partial S_Z}{\partial z}$.

Since the same optical characteristics tables and grid partitioning are used during the total process of the MHD task solving subtasks 1 and 2 are executed at first call of the flux calculating procedure only. Each call of the procedure is conducted by the transfer of current temperature and density values in central points of the hydrodynamic mesh to it.

Monte Carlo Radiation Transport. As stated in Section 3.3, HEIGHTS can use two approaches to calculate radiation transport: direct Gauss integration of the radiation transport equation and

Monte Carlo technique with weight factors hierarchy. Each method has its own advantages and disadvantages. Test calculations show that both methods give good coordinated results and can be used selectively. Because Monte Carlo calculations demand smaller computational capabilities, this method was used for the basic simulation, and direct integration was used to verify our results.

By considering radiation transport processes, we need to indicate two general aspects. Radiation fluxes should be determined for (1) correction of the plasma thermal energy and, as a result, correction of the plasma motion in device, and (2) investigation of the final useful part of the plasma radiation. These problems involve different requirements for the flux data and as a result require different numerical techniques for solving the photon transport problem. Correct calculation of the energy space redistribution in the full spectrum plays a leading role in the solution of the first problem. The model describes radiation transport adequately only if it takes into account the optical thickness of the plasma over a wide spectral range. One must divide the full spectrum of the plasma in the working diapason of the device into narrow spectral ranges with separation of strongest lines. The total spectral range must be optimized to accurate describing of the radiation energy redistribution using reasonable computational capability. As practice calculations show, MHD results have an acceptable error by the total number of spectral ranges about $\sim 10^3$. These opacities will be inapplicable for detailed investigations in spectral band of plasma focus devices 13.5±2% nm. Hence two sets of optical opacities are needed: general (for full energy redistribution calculations) and detailed (for a specific spectral band). MHD simulations execute by application of general tables. Density and temperature fields are obtained during simulation. The second stage of calculations involves investigations in the working spectral band of the device, where prepared density and temperature fields. The detailed set of optical opacities is used there.

Emission of Photons. Monte Carlo methods work by following the evolution of test particles and have the advantage of being relatively straightforward to apply to complex geometries (Fig. 10). We used a numerical algorithm with a weight hierarchy of statistical accumulated events. Two major weight categories were allocated: normalization of emitted photon "bundles" relative to the most radiated cell of computational domain, and normalization of the photon bundle magnitudes relative to the optical thickness of cell. The first weight coefficient enables us to detail the emission process by neglecting the cold cell emission.

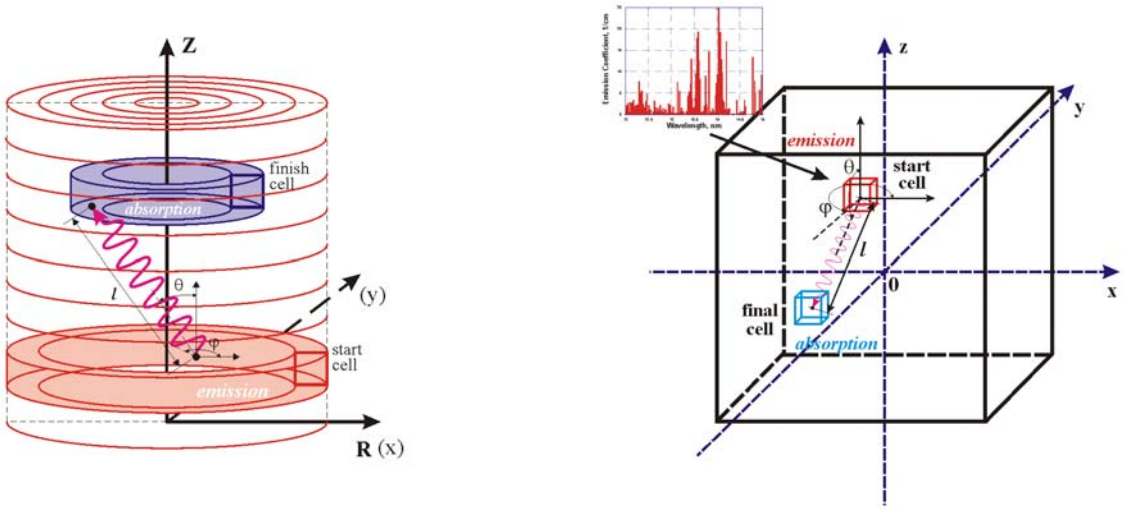

a) b)

Fig. 10. Monte Carlo presentation of emission-absorption process for (a) 2D cylindrical geometry, and (b) 3D case.

With the second coefficient, "idle" processes are ignored: situations with emitting and absorption in one cell (absorbed lines). These coefficients allowed us to decrease significantly the computational burden. As preliminary calculations at a strongly nonuniform mesh showed, a third weight coefficient can be useful. The volume of the emitting cell can be so small that the amount needed to simulation photon bundles will not enough to the proper results. The volume weight coefficient increases the computation accuracy in this case.

As is well known [34], one needs to integrate the emission coefficient k_{em} with Planck's function $B(\omega)$ in the full spectrum to obtain the number N of photons emitted in space (from the volume unit in the time unit):

$$N = 4\pi \int_0^\infty \frac{k_{em} B(\omega)}{\hbar\omega} d\omega \,. \tag{3.3.18}$$

$$B(\omega) = \frac{\hbar\omega^3}{4\pi^3 c^2} \left(e^{\frac{\hbar\omega}{T}} - 1 \right)^{-1} . \tag{3.3.19}$$

After substitution and change of variables we obtain the follow expression that is convenient for numerical calculations:

$$N = \int_{E_{\min}}^{E_{\max}} \frac{k_{em}(E,T,\rho)E^2}{\hbar^3\pi^2c^2}\left(e^{\frac{E}{T}}-1\right)^{-1} dE \qquad [\mathrm{cm^{-3}s^{-1}}], \tag{3.3.20}$$

where

E - energy of emitted photon [eV];

$E_{\min}, E_{\max}$ - spectral range [eV];

$k_{em}(E,T,\rho)$ - emission coefficient [$\mathrm{cm^{-1}}$];

T - plasma temperature [eV];

ρ - plasma density [$\mathrm{g/cm^3}$]

$\hbar = 6.58217\times10^{-16}$ [eV·s] - Planck's constant;

$c = 2.9979\times10^{10}$ [cm/s] – speed of light.

From the cell volume, temperature, and density we calculate the total amount of photons that arise in the time unit:

$$N_{i,j,k} = V_{i,j,k}\int_{E_{\min}}^{E_{\max}} \frac{k_{em}(E,T_{i,j,k},\rho_{i,j,k})E^2}{\hbar^3\pi^2c^2}\left(e^{\frac{E}{T_{i,j,k}}}-1\right)^{-1} dE, \tag{3.3.21}$$

where $V_{i,j,k}$ is the volume of cell (*i*,*j*,*k*).

The HEIGHTS code uses the Simpson's integration method:

$$\int_a^b f(x)dx \approx \frac{b-a}{6M}\left\{f_0 + f_{2M} + 2\left(f_2 + f_4 + \cdots + f_{2M-2}\right) + 4\left(f_1 + f_3 + \cdots + f_{2M-1}\right)\right\}. \tag{3.3.22}$$

For a reasonable degree of accuracy, we need $M \geq 10$.

The most critical point of Monte Carlo simulation algorithm is a search of most radiated cell.

An incorrect choice follows to the wrong weight coefficient and, as a result, to a decrease in the efficiency of the calculations. We use a function $F_L = \rho^2 T^4 V_{cell}$ in our numerical algorithm. Unfortunately, simple functions for the density, temperature and cell volume do not always give correct results. Hence, we use the cited function for the first time step only. The calculations subsequently use information about photon emission obtained from the previous time step. This technique significantly increases the efficiency of the calculations. The total amount of photons in most radiated cell is used for initial normalization of photon bundles. A reasonable degree of accuracy requires any amount of emission test simulation not less than N_{sim}. Based on this assumption the first weight coefficient of photon bundle is

$$W_1 = \frac{N^{\max}}{N_{sim}}. \qquad (3.3.23)$$

$N^{\max}$ is the integral (3.3.21) in the most radiated cell. To obtain good accuracy for the radiation transport calculations, we need $N_{sim} \sim 10^3$.

With the Monte Carlo radiation transport method, one can simulate situation in which a spectral band is absorbed greatly within one cell volume. The Monte Carlo algorithm brings to the "idle tests" in this case. The particle energy is subtracted from the cell energy by emission simulation and is added by absorption in the same cell. A second weight coefficient is introduced to solve this problem:

$$W^n_{2\{i,j,k\}} = k_{abs}\left(E_n, T_{i,j,k}, \rho_{i,j,k}\right)\Delta r_i. \qquad (3.3.24)$$

$W^n_{2\{i,j,k\}}$ is the weight coefficient of the *n*th spectral range in the cell (*i*,*j*,*k*); $k_{abs}\left(E_n, T_{i,j,k}, \rho_{i,j,k}\right)$ is the absorption coefficient of the *n*th spectral range in the cell (*i*,*j*,*k*); and Δr_i is the characteristic size of the cell. If the expression (3.3.24) is less than 1, the second coefficient is equivalent to 1.

It is possible to avoid simulations in absorbed lines. On the basis of the presented theory, the following algorithm was developed for Monte Carlo modeling of photon emission:

1. The total amount of emitted photons is calculated in the most radiated cell by integration range-by-range:

$$N^{\max} = \frac{V^{\max}}{\hbar^3 \pi^2 c^2} \sum_{k=1}^{M} k_{em}\left(E_n, T^{\max}, \rho^{\max}\right) \int_{E_k}^{E_{k+1}} E^2 \left(e^{\frac{E}{T^{\max}}} - 1 \right)^{-1} dE \,. \qquad (3.3.25)$$

This expression assumes that the emission coefficient $k_{em}\left(E_n, T^{\max}, \rho^{\max}\right)$ is constant within one spectral range. M is the total number of ranges.

2. The first weight coefficient W_1 is calculated by the formula (3.3.23).
3. The spectral range distribution of emitted photons is obtained for the (*i*,*j*,*k*) cell:

$$N_{i,j,k}^{n} = \frac{V_{i,j} k_{em}\left(E_n, T_{i,j,k}, \rho_{i,j,k}\right)}{\hbar^3 \pi^2 c^2} \int_{E_k}^{E_{k+1}} E^2 \left(e^{\frac{E}{T_{i,j,k}}} - 1 \right)^{-1} dE \,. \qquad (3.3.26)$$

4. The spectral range distribution of the second weight coefficient is determined for the (*i*,*j*,*k*) cell by the formula (3.3.24).
5. Taking into account obtained weight factors, we can calculate the total sum of Monte Carlo emission tests in the (*i*,*j*,*k*) cell:

$$N_{i,j,k}^{sim} = \frac{1}{W_1} \sum_{n=1}^{M} \frac{N_{i,j,k}^{n}}{W_{2\{i,j,k\}}^{n}} . \qquad (3.3.27)$$

6. We need to normalize the emission spectra on unit for the photon energy:

$$P_n = \frac{N_{i,j,k}^{n}}{W_1 W_{2\{i,j,k\}}^{n} N_{i,j,k}^{sim}} , \text{ i.e., } \quad \sum_{n=1}^{M} P_n = 1 , \quad n = 1, M \,. \qquad (3.3.28)$$

We assume that the photon energies were distributed equiprobability within one spectral range. Hence, linear interpolation was used to sample the emitted particle energy E_{ph}. Taking

into account both weight factors gives energy of the photon bundle $E_{ph}^{sim} = E_{ph} W_1 W_{2\{i,j,k\}}^n$ as a function of the spectral range number n. The range number is determined with the real physical energy of photon E_{ph}. The value E_{ph}^{sim} is subtracted from the cell energy by the emission process and added by the absorption process.

Photons Transition: It is important in the simulation to choose properly the start position of the sampled photon bundle within the domain cell and the initial direction of motion [35]. Axisymmetric geometry sampling of the start coordinates along *z* axis is equiprobable (analogously *x*, *y* and *z* in Cartesian 3D). Curvature of space should be taken into account along the *r* axis: as one approached the cell volume decreases by constant step Δr (see Fig. 11). These facts follow to expressions:

$$z = z_1 + \xi(z_2 - z_1), \tag{3.3.29}$$

$$r = \sqrt{r_1^2 + \xi(r_2^2 - r_1^2)}, \tag{3.3.30}$$

where

r_1, r_2 are the left and right borders of cell along *r* axis correspondingly;

z_1, z_2 are the left and right borders of cell along *z* axis correspondingly;

ξ is the random number within the interval [0,1].

Equiprobable space directions (azimuth angle φ and axial angle θ in Fig. 10) are sampled with standard method:

$$\varphi = 2\pi\xi, \tag{3.3.31}$$

$$\cos\theta = 2\xi - 1.$$

Photons Absorption: Attenuation of light intensity as a result of matter absorption is described by the expression $I = I_0 e^{-\int_0^l k_{as}(\omega,l)dl}$ [36] or, in photon number terms

$$N(\omega) = N_0(\omega) e^{-\int_0^l k_{abs}(\omega, l) dl} . \qquad (3.3.32)$$

Here $N_0(\omega)$ is the initial number of photons with frequency ω and l is the path length.

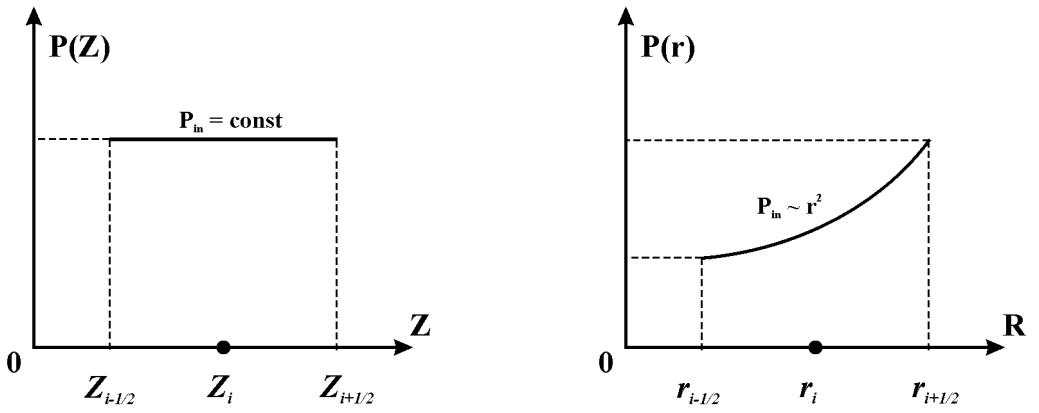

(a) (b)

Fig. 11. Probability density distributions of photon start coordinates along axes within one computational domain cell: (a) r-axis; (b) Z-axis.

By considering the photon path within one cell (where the absorption coefficient is independent of the coordinates) we can calculate the attenuation as

$$N(\omega) = N_0(\omega) e^{-k_{abs}(\omega) l} . \qquad (3.3.33)$$

The absorption/transition probability of the photon by path length l in the cell (i,j,k) following the expression (3.3.32) is given

$$P^{abs}_{i,j,k}(\omega) = 1 - \frac{N(\omega)}{N_0(\omega)} = 1 - e^{-k_{abs\{i,j,k\}}(\omega) l}, \qquad (3.3.34)$$

$$P^{trans}_{i,j,k}(\omega) = e^{-k_{abs\{i,j,k\}}(\omega) l}$$

For complete simulation of the absorption process, we need to have the absorption coefficient (which depends on the matter parameters in the computational domain cell and on the photon energy), and we need to know the photon path length in this cell. The photon path length within the cell can be obtained by consecutive solution of equation systems for the cell borders. For the more complicated case of cylindrical symmetry, these equations are [37]

$$\begin{cases} x = x_0 + l\sin\theta\cos\varphi \\ y = y_0 + l\sin\theta\sin\varphi \\ z = z_0 + l\cos\theta \\ z = z_i \end{cases}, \tag{3.3.35}$$

$$\begin{cases} x = x_0 + l\sin\theta\cos\varphi \\ y = y_0 + l\sin\theta\sin\varphi \\ z = z_0 + l\cos\theta \\ x^2 + y^2 = r_i^2 \end{cases}. \tag{3.3.36}$$

Here, (x_0, y_0, z_0) is the start position of photon, (x, y, z) is the final position (intersection with z_j border or r_i border of cell), θ is the axial angle, φ is the azimuth angle. The photon path length l is the minimum at the system (3.3.35)-(3.3.36) solutions.

After sampling the E_{ph} and E_{ph}^{sim} energies, photon transition of computational domain cells is simulated by checking each cell on absorption. Summation of all test results $N = \sum_{i,j,k} N_{i,j,k}^{sim}$ presents information about the energy redistribution in the computational domain due to radiation transport. Installation of additional counters at the cell borders enables us to calculate radiation fluxes in matter. We can easily obtain the radiation fluxes on surfaces with complicated geometry. Investigation of radiation spectra requires additional registration of the energy distributions of the absorbed photons. Our numerical technique has universality both for radiated objects geometry and spectral bands applications. Depending on the problem, one can investigate energy redistribution over a wide range or can calculate radiation transport in a narrow band by detailed resolution of each spectral line.

3.4. Laser Radiation Absorption

Ideally, the laser absorption by a target should be treated in two phases: first by the cold, unperturbed target and then by the target having a plasma layer in front of the remaining solid target. Most of the hydrodynamics codes developed for infrared, visible, or UV lasers interaction consider the plasma creation as instantaneous, at last compared to the driving laser duration. In this approximation, the laser interacts only with the expanding plasma because the beam is reflected at the critical density, typically about a hundred times lower than the solid density. Figures 12 and 13 present HEIGHTS calculations of the $10^{\times}$ attenuation of the initial laser beam intensity for a Xe target. The figures show the depth of penetration for wave lengths $\lambda = 1.064$ μm and $\lambda = 0.53$ μm, respectively, which are use extensively in LPP devices for EUV lithography [38-41]. For most parts of the modeling, inverse bremsstrahlung was proposed as the process by which the laser radiation was absorbed by the plasma electrons [42, 43].

The HEIGHTS package uses, for the laser radiation absorption simulation, the Monte Carlo technology presented in Section 3.3. Advanced schemes allow one to model the laser beams distributed in time and space, focused in any space point. Reflection processes are taken into account.

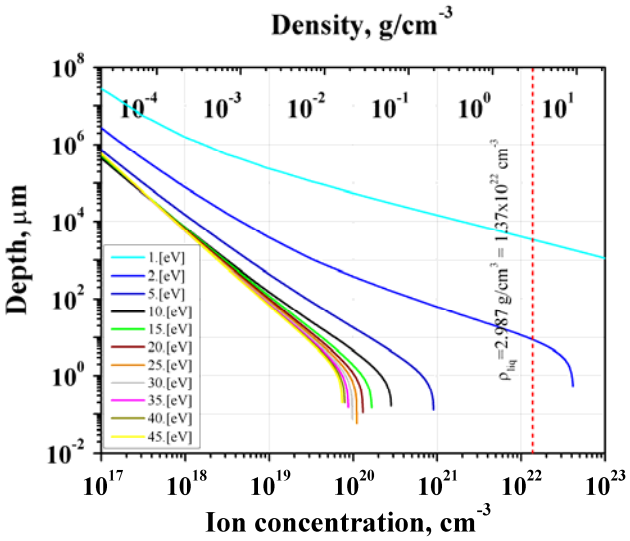

Fig. 12. Depth of the $10^{\times}$ laser beam attenuation in Xe plasma for $\lambda = 1.064$ μm.

The laser beam is considered as directional flux of the macro-photons. The separate macro-photon has the same properties (absorption, reflection probability, etc.) of the one real laser radiation photon. However, the action of each real photon cannot be simulated because of large number of real photons in the beam, and the action (energy transport) of each group photon is combined into the macro-photon action. The number of real photons W_{macro} in the macro-photon can be estimated from the total number of available macro-photons N_{macro}

$$N_{macro} = \frac{N_{real}}{W_{macro}}, \quad N_{real} = \frac{P_{las}}{E_{ph}}. \tag{3.4.1}$$

Here P_{las} is the momentary laser power, and E_{ph} is the energy of one real laser radiation photon.

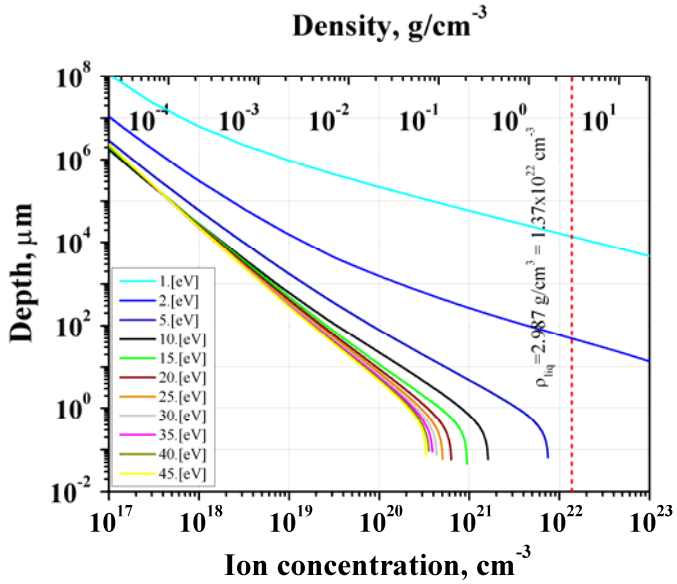

Fig. 13. Depth of the $10^{\times}$ laser beam attenuation in Xe plasma for λ = 0.53 μm.

The HEGHTS package considers the time distribution of the laser pulse power. In the case of square time distribution, the laser pulse power is

$$P_{las} = \frac{Q_{pulse}}{t_{pulse}}, \tag{3.4.2}$$

where the energy of the pulse Q_{pulse} is distributed uniformly in the pulse duration t_{pulse}. Gaussian distribution in time can be expressed as a time function:

$$P_{las}(t) = P_0 \exp\left\{-\frac{(t-\sigma_t)^2}{\sigma_t^2}\right\}. \qquad (3.4.3)$$

This equation assumes, that the pulse duration is $t_{pulse} = 2\sigma_t$. The maximal power P_0 can be calculated from the integral (see Fig. 14)

$$P_0 = \frac{Q_{pulse}}{\int_0^{\infty} \exp\left\{-\frac{(t-\sigma_t)^2}{\sigma_t^2}\right\} dt}. \qquad (3.4.4)$$

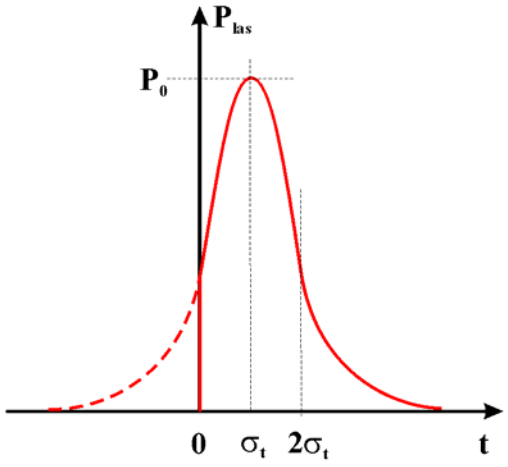

Fig. 14. Gaussian distribution of the laser pulse energy in time.

Assuming a round laser beam cross-section, one can choose the space distribution of the laser radiation flux to be uniform and Gaussian along the radius. Most applications have Gaussian space distribution [44]

$$I(r,t) = I_0(t)\exp\left\{-\frac{r^2}{\sigma_s^2}\right\}, \tag{3.4.5}$$

where taken into account pulse power distribution in time $P_{las}(t)$. There is also proposed that radius of beam is equal $r_{beam} = \sigma_s$ in Eq. (3.4.5). Double integration of the Gauss distribution has the analytical solution

$$P_{las}(t) = \iint_{\infty} I_0(t)\exp\left\{-\frac{r^2}{\sigma_s^2}\right\} dS = I_0(t)\pi\sigma_s^2 , \tag{3.4.6}$$

and hence the laser intensity in case of Gaussian space distribution can be given as

$$I(r,t) = \frac{P_{las}(t)}{\pi\sigma_s^2}\exp\left\{-\frac{r^2}{\sigma_s^2}\right\}. \tag{3.4.7}$$

Equation (3.4.7) loses an exponential term in the case of square space distribution.

The HEIGHTS package has a computation module for controlling the directional and focusing the characteristics of a laser beam set. Figure 15 presents a 3D computation domain directed onto the target laser beam.

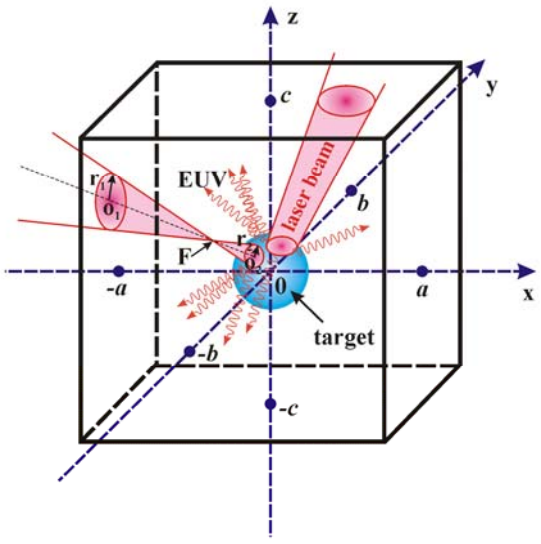

Fig. 15. Laser beam determination in the three-dimensional space.

For a full description of the laser beam, we need to define the coordinates of the initial laser beam point $O_1(x_1, y_1, z_1)$, the radius of the beam at initial point r_1, the final point $O_2(x_2, y_2, z_2)$, and the final radius r_2. Additionally, we should define where the focus point F of the laser beam is located: inside or outside the $[O_1O_2]$segment. These five items define the space geometry of the laser beam completely. A parallel laser beam can be defined with $r_1 = r_2$ and focus location outside the $[O_1O_2]$ segment. Following this simple method for determining the laser beam position, the numerical algorithm should simulate the start point coordinate and direction for each laser radiation photon (by conservation of the time and space distributions). The photons initial position can be simulated easily in an adjuvant (primed) 3D Cartesian coordinate system, which was used for the conversion between laboratory and primed coordinate systems. The primed coordinate system was selected so that the z'-axis was parallel to the laser beam axis and the x'-axis was located on the $x0y$ plane. The position relationship of two systems S and S' can be described by using two Euler angles Θ and Φ only [46]. The third Euler angle Ψ is equal to zero because the x'-axis coincides with the line of nodes located on the $x0y$ plane. Hence, arbitrariness is correct in the case of the equiprobable distribution of the laser beam photons in the azimuth direction and no strong requirements on the orientation of the x'-axis. The junction between the systems of coordinates can be expressed in matrix form as follows

$$\begin{bmatrix} x \\ y \\ z \end{bmatrix} = \begin{bmatrix} \cos\Phi & -\cos\Theta\sin\Phi & \sin\Theta\sin\Phi \\ \sin\Phi & \cos\Theta\cos\Phi & -\sin\Theta\sin\Phi \\ 0 & \sin\Theta & \cos\Theta \end{bmatrix} \times \begin{bmatrix} x' \\ y' \\ z' \end{bmatrix}, \tag{3.4.8}$$

where the Euler angles Θ and Φ can be calculated from the laser beam axis orientation in the S system:

$$\cos\Theta = \frac{z_1 - z_2}{\sqrt{(x_1 - x_2)^2 + (y_1 - y_2)^2 + (z_1 - z_2)^2}} \quad \cos\Phi = \frac{y_2 - y_1}{\sqrt{(x_1 - x_2)^2 + (y_1 - y_2)^2}}$$
$$\sin\Theta = \frac{\sqrt{(x_1 - x_2)^2 + (y_1 - y_2)^2}}{\sqrt{(x_1 - x_2)^2 + (y_1 - y_2)^2 + (z_1 - z_2)^2}} \quad \sin\Phi = \frac{x_1 - x_2}{\sqrt{(x_1 - x_2)^2 + (y_1 - y_2)^2}} \tag{3.4.9}$$

Additionally, shift between the start plane of photons and point of origin in the primed system S' $\Delta z' = z_1' - \sqrt{(x_1 - x_2)^2 + (y_1 - y_2)^2 + (z_1 - z_2)^2}$ is taken into account. In accordance with (3.4.5)-(3.4.7) we obtained equations for simulating the square space distribution of the laser beam with radius σ_s:

$$\begin{aligned} x' &= \sigma_s \sqrt{\xi_1} \cos(2\pi\xi_2) \\ y' &= \sigma_s \sqrt{\xi_1} \sin(2\pi\xi_2) \end{aligned}, \tag{3.4.10}$$

and for Gaussian distribution

$$\begin{aligned} x' &= \sigma_s \sqrt{-\ln\xi_1} \cos(2\pi\xi_2) \\ y' &= \sigma_s \sqrt{-\ln\xi_1} \sin(2\pi\xi_2) \end{aligned}. \tag{3.4.11}$$

Here ξ_1 and ξ_2 are independent random numbers in the interval [0, 1].

As was mentioned earlier the HEGHTS model considers laser absorption in a plasma cloud. Therefore, inverse bremsstrahlung was assumed as the main process by which the laser radiation was absorbed by the plasma electrons. The classical value for the absorption coefficient k_{abs}^{las} characterizing this collisional absorption mechanism is [47]

$$k_{abs}^{las} = \frac{16\pi Z n_e^2 e^6 \ln\Lambda(\nu)}{3c\nu^2 (2\pi m_e k_B T_e)^{3/2} \left(1 - \nu_p^2/\nu^2\right)^{1/2}}, \tag{3.4.12}$$

where e, n_e, m_e, and T_e are the electron charge, density, mass and temperature respectively; Ze is the ionic charge; c is the light speed; ν is the frequency of laser light; $\nu_p = \sqrt{\frac{n_e e^2}{\pi m_e}}$ is the plasma frequency; and k_B is the Boltzmann constant. The Coulomb logarithm is given by [48]

$$\ln\Lambda = \ln\left[\frac{3}{2}\sqrt{\frac{\left(k_B T_e\right)^3}{\pi n_e}}\frac{1}{Ze^3}\right]. \qquad (3.4.13)$$

Condition $\nu_p \geq \nu$ in any space point is used for simulating the photon reflection. The new direction of motion is sampled isotropic.

4. Total Variation Diminishing Solution.

Total variation diminishing (TVD) schemes ensure that the total variation in the calculated area does not increase with time [21]:

$$\sum_j \left|\Delta U_{j+1/2}^{n+1}\right| \leq \sum_j \left|\Delta U_{j+1/2}^{n}\right|. \qquad (4.1)$$

As is well known, predictor-corrector schemes are unstable and need the addition of an energy dissipation mechanism at the front of the shock waves [26]. It can be artificial diffusion, viscosity, etc. The coefficients of the mechanism can be tuned to get better results, but that problem-dependent approach is not in the spirit of modern shock-capturing schemes. The TVD method is a particular case of essentially non oscillatory (ENO) schemes. There is no generation of nonphysical oscillations along the shock waves in these solutions. Mechanisms of numerical (mathematical) dissipation with automatic feedback allow transformation of shock wave kinetic energy in heat energy in this case. The scheme can solve shock waves within 2-4 cells.

We present a general approach for constructing a TVD-LF scheme for the 1D case of the hyperbolic conservation law for any variable U. More detailed HEIGHTS numerical schemes for 2D and 3D cases are presented in Appendix 1 and 2. As indicated above, the differential form of the conservation law equation can be given for any conservative variable U for the 1D case:

$$\frac{\partial U(x,t)}{\partial t} + \frac{\partial F(U)}{\partial x} = 0. \qquad (4.2)$$

The computational mesh was defined as having unequal spacing $\Delta x_i = x_{i+1/2} - x_{i-1/2}$, where the subscripts $i-1/2$ and $i+1/2$ refer to quantities defined on the cell interfaces. Cell centers $x_i = \left(x_{i+1/2} + x_{i-1/2}\right)/2$ are specified at positions *i*. The code uses standard notation for evaluating the function U_i^n defined at cell centers *i* and time level *n*. A time spacing t^n, with intervals $\Delta t^n = t^{n+1} - t^n$, was assumed. Explicit algorithms expect calculation of U_i^{n+1} values only from the neighbor cells data on time level *n*. Data from neighbor cells should be enough for determining fluxes $F_{i\pm1/2}^{final}$ on the cell borders to calculate the next time level values

$$U_i^{n+1} = U_i^n - \frac{\Delta t^n}{\Delta x_i}\left(F_{i+1/2}^{final} - F_{i-1/2}^{final}\right). \tag{4.3}$$

Final fluxes $F_{i\pm1/2}^{final}$ are composed of two parts: main fluxes $F_{i\pm1/2}^{LR}$ and TVD corrections $\Phi_{i\pm1/2}$. Main fluxes are an average of left and right fluxes on any cell interface $F_{i\pm1/2}^{LF} = \frac{1}{2}\left(F_{i\pm1/2}^{L} + F_{i\pm1/2}^{R}\right)$. The correction term is based on the concept of the maximum propagation speed $c_x^{\max}$ of information in direction *x*. In the case of hydrodynamics it is the speed of sound, v_{ac}. The MHD case takes into account Alfven waves speed, also. (For details of this problem, see [9, 21]). We express for the case of HD and MHD with one component of the magnetic field B as follows:

$$c_x^{\max} = |v_x| + |v_{ac}|, \quad c_x^{\max} = |v_x| + \sqrt{v_{ac}^2 + \frac{B^2}{4\pi\mu\rho}}\,. \tag{4.4}$$

Here ρ is the mass density. Below we present expressions only for one border cell $i+1/2$. The expression is analogous to the left border $i-1/2$. Consequently it is possible to show the equation for the final flux:

$$F_{i+1/2}^{final} = \frac{1}{2}\left(F_{i+1/2}^{L} + F_{i+1/2}^{R} - c_{i+1/2}^{LR}\Delta U_{i+1/2}^{LR}\right), \tag{4.5}$$

where

$$F^L_{i+1/2} = F\left(U^L_{i+1/2}\right),\ F^R_{i+1/2} = F\left(U^R_{i+1/2}\right),\ U^{LR}_{i+1/2} = \frac{1}{2}\left(U^L_{i+1/2} + U^R_{i+1/2}\right), \text{ and } \Delta U^{LR}_{i+1/2} = U^L_{i+1/2} - U^R_{i+1/2}.$$

This numerical scheme has a second-order approximation in time and space. The second-order approximation in time is achieved by using a Hancock predictor step. Following this, we calculated the left and right $U_{i+1/2}$ values from the data obtained in the predictor step $t = n + 1/2$

$$U^L_{i+1/2} = U^{n+1/2}_i + \frac{1}{2}\overline{\Delta U^n_i},\ \ U^R_{i+1/2} = U^{n+1/2}_{i+1} - \frac{1}{2}\overline{\Delta U^n_{i+1}} \tag{4.6}$$

where limited differences are defined as minmod- functions or other slope limiters [21] of the U differences

$$\overline{\Delta U_i} = \min\mathrm{mod}\left(\Delta U^n_{i-1/2}, \Delta U^n_{i+1/2}\right),\ \overline{\Delta U_{i+1}} = \min\mathrm{mod}\left(\Delta U^n_{i+1/2}, \Delta U^n_{i+3/2}\right) \tag{4.7}$$

$$\Delta U^n_{i-1/2} = U^n_i - U^n_{i-1},\ \Delta U^n_{i+1/2} = U^n_{i+1} - U^n_i,\ \Delta U^n_{i+3/2} = U^n_{i+2} - U^n_{i+1}.$$

In the full step, upwinded left and right states, denoted by $U^L_{i+1/2}$ and $U^R_{i+1/2}$, are formed from values on the predictor step $U^{n+1/2}_i$ and $U^{n+1/2}_{i+1}$:

$$U^{n+1/2}_i = U^n_i - \frac{\Delta t^n}{\Delta x_i}\left[F\left(U^{nL}_{i+1/2}\right) - F\left(U^{nR}_{i-1/2}\right)\right],\ U^{n+1/2}_{i+1} = U^n_{i+1} - \frac{\Delta t^n}{\Delta x_{i+1}}\left[F\left(U^n_{i+3/2}\right) - F\left(U^{nR}_{i+1/2}\right)\right]. \tag{4.8}$$

The cell border values are calculated analogously (4.6):

$$U_{i+1/2}^{nL} = U_i^n + \frac{1}{2}\overline{\Delta U_i^n}, \qquad U_{i-1/2}^{nR} = U_i^n - \frac{1}{2}\overline{\Delta U_i^n} \tag{4.9}$$

$$U_{i+1/2}^{nR} = U_{i+1}^n - \frac{1}{2}\overline{\Delta U_{i+1}^n}, \qquad U_{i+3/2}^{n} = U_{i+1}^n + \frac{1}{2}\overline{\Delta U_{i+1}^n}$$

The easiest way to extend the one-dimensional numerical scheme to more space dimensions is to use dimensional (operator) splitting [49, 21]. A multidimensional problem is simply split into a sequence of one-dimensional problems. Assuming that L_x, L_y, and L_z are temporally and spatially second-order operators that evolve the one-dimensional equations

$$\begin{aligned} &\frac{\partial \mathbf{U}}{\partial t} + \frac{\partial \mathbf{F}_x}{\partial x} = 0 \\ &\frac{\partial \mathbf{U}}{\partial t} + \frac{\partial \mathbf{F}_y}{\partial y} = 0 \\ &\frac{\partial \mathbf{U}}{\partial t} + \frac{\partial \mathbf{F}_z}{\partial z} = 0 \end{aligned} \tag{4.10}$$

one can apply these 1D operators one by one in alternating order as

$$\mathbf{U}^{n+2} = L_x L_y L_z \mathbf{U}^{n+1} = L_x L_y L_z L_z L_y L_x \mathbf{U}^n \tag{4.11}$$

for 3D expansion. The HEIGHTS package uses a modified version of the operator splitting method [6, 7] where realized componentwise decomposition of fluxes. An expanded 13-cell template is used for the 2D case and 33-cell for the 3D case. Boundary conditions are defined separately for each direction of the decomposed fluxes. Appendixes 1 and 2 present more detailed applications of this method to the 2D and 3D case, respectively.

5. Two-Temperature Approximation

Because inverse bremsstrahlung is the main mechanism of laser radiation absorption in plasma, the electrons are the main recipient of the laser radiation energy. The maximal energy that can be transmitted from one particle to another particle by elastic interaction is given by [50]

$$E_{\max} = \frac{4m_1 m_2}{(m_1 + m_2)^2} E_1 = C_{tr} E_1, \qquad (5.1)$$

where m_1 and E_1 are the mass and energy of the bullet particle, and m_2 is the mass of the recoil particle. The transmission coefficient for the equal particles (electron-electron or ion-ion) reaches ~1.0. The transmission between electron and ion (Xe^+ for example) is much smaller, $C_{tr}^{ei} \sim 1.6 \cdot 10^{-5}$. These estimations show that energy transfer between the same particles is considerably higher; that is, by laser heating of the plasma electrons, the thermal energy will be transferred from the electrons to the ions with a time delay. The temperature of the electrons will differ from that of the ions because laser heating is a very fast process as a rule. Describing the laser plasma as a mixture of two gases (electronic and ionic) is more correct and enables one to explain numerous physical phenomena of laser heating: electrons overheating and acceleration, magnetic field generation, and so forth. The final MHD equation set (3.2) should be expanded to consider of these plasma component. The three conservation law equations should be split (mass density, pulse, energy density) to obtain electron and ion parts.

The HEGHTS model takes into account the principle of electro-neutrality of plasma. This approach neglects local charge separation and enables one to split the energy equation only. The continuity and pulse equations consider plasma motion as a whole. Moreover, it was found that the best way for total energy control is to solve the energy equation for the whole plasma. The energy of the plasma components is separated by the introduction of an additional energy equation for ions, which takes into account the mechanism of energy exchange between the ionic and electronic parts. The additional ion energy equation operates with the ion particles in the ideal gas approximation. The nonideal part (ionization energy) is included in the electronic part and is summarized in the total plasma energy equation. The expanded general MHD equation set in a two-temperature approximation used in the HEIGHTS package is given by

$$
\begin{cases}
\dfrac{\partial \rho}{\partial t} + \nabla \cdot (\rho \mathbf{v}) = 0 \\
\dfrac{\partial \rho \mathbf{v}}{\partial t} + \nabla \cdot \left(\rho \mathbf{v}\mathbf{v} + p_{tot} - \dfrac{\mathbf{B}\mathbf{B}}{4\pi\mu} \right) = -\dfrac{1}{4\pi\mu} \mathbf{B} (\nabla \cdot \mathbf{B}) \\
\dfrac{\partial e_{tot}}{\partial t} + \nabla \cdot \left[\mathbf{v}(e_{tot} + p_{tot}) - \dfrac{1}{4\pi\mu} (\mathbf{v} \cdot \mathbf{B}) \cdot \mathbf{B} + \dfrac{c^2 \eta}{16\pi^2 \mu^2} (\nabla \times \mathbf{B}) \times \mathbf{B} - \lambda_e \nabla T_e - \lambda_i \nabla T_i - \mathbf{S}_{rad} \right] = \\
\qquad\qquad = Q_{las} - \dfrac{1}{4\pi\mu} (\mathbf{v} \cdot \mathbf{B}) \cdot (\nabla \cdot \mathbf{B}) \\
\dfrac{\partial e_i}{\partial t} + \nabla \cdot \left[\mathbf{v}(e_i + p_i) - \lambda_i \nabla T_i \right] = 3 \dfrac{m_e n_e}{m_i \tau_e} (k_B T_e - k_B T_i) \\
\dfrac{\partial \mathbf{B}}{\partial t} + \nabla \cdot (\mathbf{v}\mathbf{B} - \mathbf{B}\mathbf{v}) + \dfrac{c^2}{4\pi\mu} \nabla \times (\eta \nabla \times \mathbf{B}) + \dfrac{c k_B}{e n_e} \nabla n_e \times \nabla T_e = -\mathbf{v} (\nabla \cdot \mathbf{B}),
\end{cases}
\tag{5.2}
$$

where are incorporated the source of laser energy Q_{las}, the energy exchange between electron and ion plasma components, and the magnetic source term. Also included heat conductions for ions and electrons [51]

$$
\lambda_e = \frac{25 n_i T_e k_B^2}{4 \beta_e \gamma_e m_e} \frac{1}{1 + \dfrac{25\Omega_e^2}{\beta_e (4\beta_e - 9) \gamma_e^2}}, \quad \lambda_i = \frac{25 n_i T_i k_B^2}{4 \beta_i \gamma_i m_i} \frac{1}{1 + \dfrac{6.25\Omega_i^2}{\beta_i^2 \gamma_i^2}}, \tag{5.3}
$$

where

$$
\gamma_e = \frac{4\sqrt{2\pi} e^4 n_i \ln \Lambda}{3 (k_B T_e)^{3/2} m_e^{1/2}}, \quad \gamma_i = \frac{4\sqrt{2\pi} e^4 n_i \ln \Lambda}{3 (k_B T_i)^{3/2} m_i^{1/2}}, \tag{5.4}
$$

$$
\beta_e = \sqrt{2} + \frac{13}{4}, \ \beta_i = \sqrt{2} + \frac{15}{2} \left(\frac{T_i}{T_e} \right)^{3/2} \left(\frac{m_e}{m_i} \right)^{1/2} \tag{5.5}
$$

with the cyclotron frequencies expressed as $\Omega_{e/i} = \frac{eB}{cm_{e/i}}$. The Coulomb logarithm is given by (3.4.13). As was determined by numerical experiment, the ion part of heat transport is significantly smaller in comparison to the electron part and can be neglected.

The magnetic diffusion and Joule heating can be determined with the Spitzer resistivity expression [48]

$$\eta = \frac{1}{2}\sqrt{\frac{\pi^3 m_e}{8\left(k_B T_e\right)^3}} Ze^2 \ln\Lambda . \tag{5.6}$$

The electron-ion energy exchange was considered as a function of electron and ion gas temperatures [51]

$$Q_{ei} = 3\frac{m_e n_e}{m_i \tau_e}\left(k_B T_e - k_B T_i\right), \tag{5.7}$$

where the time between electron interactions is

$$\tau_e = \frac{3\sqrt{m_e}\left(k_B T_e\right)^{3/2}}{4\sqrt{2\pi}e^4 Z^2 n_i \ln\Lambda} . \tag{5.8}$$

Numerical experiments with laser power fluxes up to 10^{12} W/cm^2 (typical of those used for EUV lithography) showed a small influence of the thermally generated magnetic field on the plasma behavior and on the EUV output. (See Appendixes 3, 4, and 5 which give the hydrodynamics equation sets for the cases with and without magnetic field generation.) The cases that take into account the magnetic field can be used for numerical experiments with laser plasma in an externally induced magnetic field (i.e., for debris mitigation).

6. Validation and Benchmarking

To validate the model and benchmark the code, we solved several test problems and compared the results with known analytical and experimental data. The calculation blocks were tested separately (TVD-LF, thermal conductivity, radiation transport etc.). We also tested combined action of numerical blocks in various alternations of blocks to check stability of results. Moreover, the full model of LPP device was provided and compared with available data.

6.1. Testing of the TVD-LF Numerical Scheme

To validate the convective block and to test our numerical scheme with the hydrodynamics fluxes directional decomposition (see Section 4), we computed the supersonic air flow around a sphere and compared it to published data. The thermodynamic properties of air were considered in an ideal gas approximation (one temperature) with adiabatic constant $\gamma = 1.4$:

$$v_{ac} = \sqrt{\frac{\gamma p_h}{\rho}}, \; p_h = (\gamma - 1)\left(e_h - \frac{\rho v^2}{2} \right), \; T = \frac{\mu p_h}{\rho R}. \qquad (6.1.1)$$

Here μ is molar mass of gas and R is universal gas constant. We tested the two-dimensional TVD-LF numerical algorithm, presented in Appendix 1, after excluding of the magnetic field. Figure 16 shows the excellent agreement between tabulated data [52] and computation by our scheme of density distribution in the shock wave in front of the sphere for the flow velocity 1.5 M.

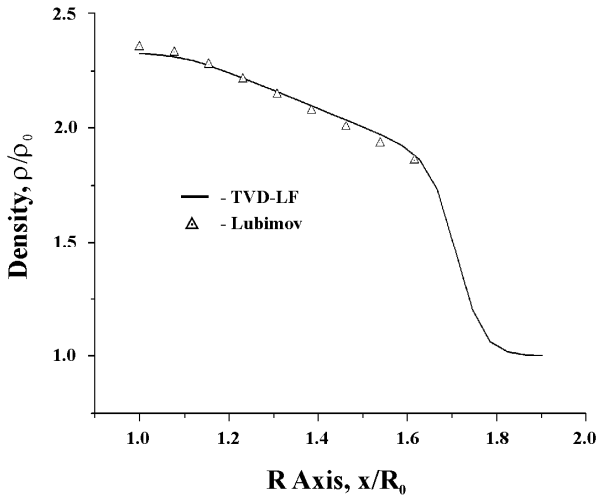

Fig. 16. Density distribution in the front of the air blasted (1.5M) sphere. Comparison to tabulated data [52].

We compared the results from the total variation diminishing scheme with experimental data. Figure 17a presents a shadowgraph of the ½-inch sphere that flows through air at M=1.53 [53]. Figure 17b presents the TVD-LF calculations, which give identical location and angles for the shock wave fronts.

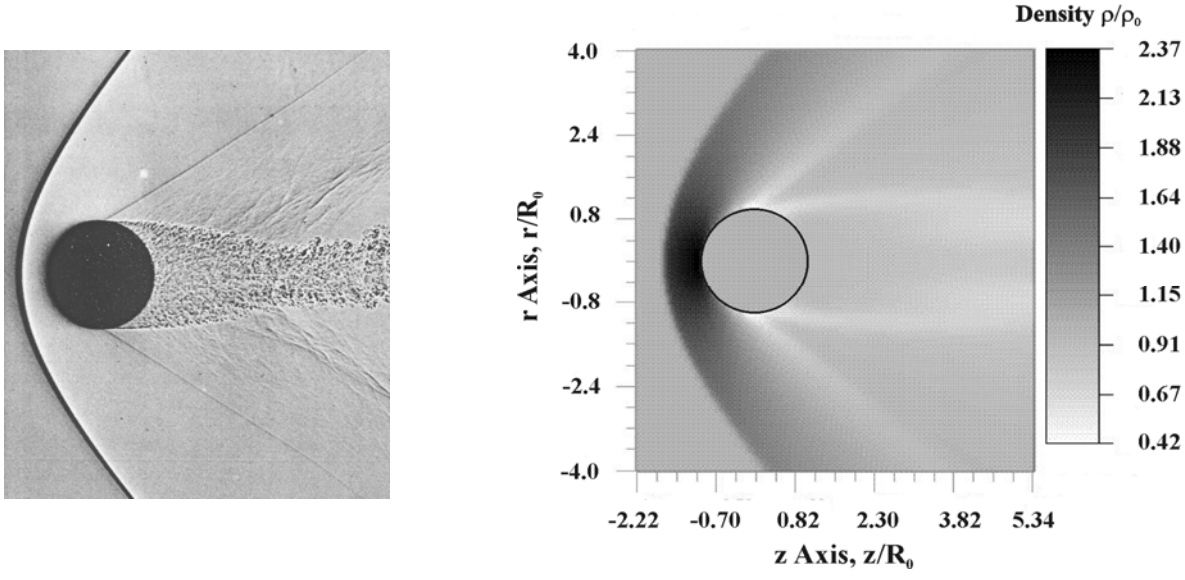

a) b)

Fig. 17. Air blasting (1.53M) of sphere. a) A shadowgraph catches a ½ -inch sphere in free flight through air [53]; b) Calculated with TVD-LF density distribution.

6.2. Validation of the Implicit Sparse Matrix Scheme

To validate the implicit numerical scheme that solves the parabolic part of the general MHD equation set, we calculated two test problems and compared the results with known analytical data [54]. The first test problem describes heat transport into the semi-restricted computational domain with thermal conductivity $\lambda = \lambda_0 T^{\alpha}$. The power dependence of conductivity allows analytical solution of the heat transport problem

$$\frac{\partial T}{\partial t} = \frac{\partial}{\partial z}\lambda_0 T^{\alpha}\frac{\partial T}{\partial z}, \text{ for } z > 0,\ t > 0 \tag{6.2.1}$$

with initial and boundary conditions

$$T(0,t) = \left[\frac{\alpha D}{\lambda_0}(z_1 + Dt)\right]^{1/\alpha},\ t > 0 \tag{6.2.2}$$

$$T(z,0) = \begin{cases} \left[\frac{\alpha D}{\lambda_0}(z_1 - z)\right]^{1/\alpha}, & 0 < z \le z_1 \\ 0, & z > z_1 \end{cases}$$

given by

$$T(z,t) = \begin{cases} \left[\frac{\alpha D}{\lambda_0}(Dt + z_1 - z)\right]^{1/\alpha}, & 0 < z \le z_1 + Dt \\ 0, & z > z_1 + Dt \end{cases}. \tag{6.2.3}$$

Test calculations were performed for the parameter set $\alpha = 2$, $\lambda_0 = 0.5$, $z_1 = 0$, and $D = 5$ on uniform and appreciably nonuniform meshes. Figure 18 presents time-step calculations for the implicit algorithm with uniform mesh and $\Delta z = 10^{-2}$. The heat front at time moment $t = 0.1$ is shown. The scheme remains stable for very large time steps. Analytical results and numerical simulation solutions for this heat transport problem were satisfactorily fit by $\Delta t \le 10^{-4}$

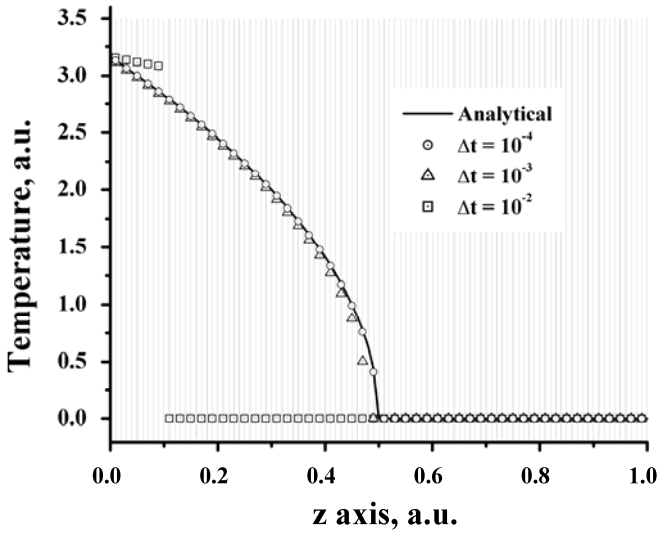

Fig.18. Heat front distribution calculated with different time steps. Uniform mesh $\Delta z = 0.01$. Time moment $t = 0.1$.

with the implicit method. We also constructed a simple explicit numerical scheme and obtained similar results to the implicit scheme but only by using time steps smaller than $\Delta t \le 10^{-6}$. Larger time steps caused oscillations and numerical scheme disturbances. Accordingly, the difference between implicit and explicit time steps is two orders of magnitude.

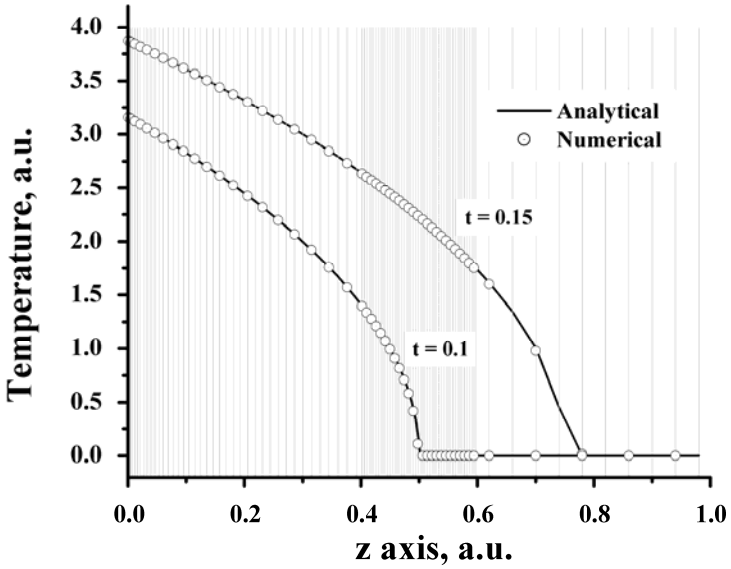

Fig. 19. Heat front evolution. Nonuniform mesh; time step $\Delta t = 10^{-4}$.

The implicit algorithm retains stability by using the appreciably nonuniform meshes. The evolution of the heat front on a nonuniform mesh is presented in Fig. 19. The calculations were carried out with time step $\Delta t = 10^{-4}$. The analytical and numerical simulation results compare very well.

The second numerical test investigated the "stopped" temperature wave, obtained from Eq. (6.2.1) at intervals z > 0, and $0 < t < C$ with initial and boundary conditions given by

$$T(0,t) = \left[\frac{\alpha z_1}{2\lambda_0(\alpha+2)(C-t)} \right]^{1/\alpha}, \quad 0 < t < C, \tag{6.2.4}$$

$$T(z,0) = \begin{cases} \left[\dfrac{\alpha(z_1 - z)^2}{2\lambda_0(\alpha+2)C} \right]^{1/\alpha}, & 0 < t < C \\ 0, & z > z_1 \end{cases}.$$

The temperature front evolution in this case is

$$T(z,t)=\begin{cases}\left[\dfrac{\alpha(z_1-z)^2}{2\lambda_0(\alpha+2)(C-t)}\right]^{1/\alpha}, & 0\le z\le z_1\\ 0, & z>z_1\end{cases}. \qquad (6.2.5)$$

Analytical and numerical simulation results were compared for coefficients $\alpha = 2$, $\lambda_0 = 0.5$, $z_1 = 0.5$, and $C = 0.1125$. Figure 20 presents calculations obtained by an implicit scheme with time step $\Delta t = 10^{-4}$ on uniform spatial mesh $\Delta z = 10^{-4}$.

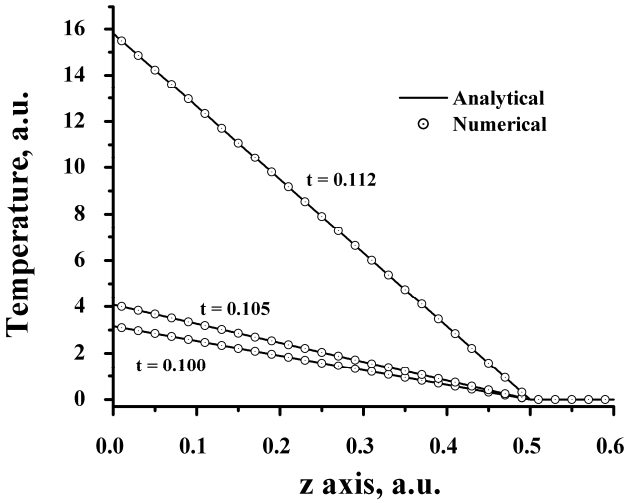

Fig. 20. "Stopped" temperature wave. Time step $\Delta t = 10^{-4}$. Uniform mesh $\Delta t = 10^{-2}$.

Our validation of the numerical simulations with analytical results showed stability and accuracy for artificial problems. However, computation for real devices is of much more interest. We thus compared results for a discharge plasma device calculated by both the implicit and explicit schemes. A detailed description of the discharge device is given in [8]. Figure 21 includes temperature and magnetic field distributions around the device electrode at 200 ns after discharge start. The computational procedure combined magnetic field input with external current and excluded the electrode area from the domain. The plasma motion was calculated by the implicit scheme and by substitution of heat and magnetic diffusion fluxes directly into the MHD explicit scheme [6, 7]. The results obtained by both schemes compared well. Figure 22 shows cross-sections of temperature and magnetic fields distributions calculated by both schemes for $z = 1.5$ cm in Figure 21. The independent implicit scheme has a number of advantages over the direct MHD explicit method. Of vital importance is the ability to use much longer time steps. The curves in Figure 22 were calculated with time step $\Delta t = 5$ ps for the implicit method and $\Delta t = 5 \cdot 10^{-2}$ ps for the explicit method. The time step is strongly confined with heat transport in areas of small plasma density. These areas are usually the back of the magnetic "snow plow".

The explicit scheme is very unstable in heat transport calculations for rarefied plasma. One can explain this result by considering the mechanism of thermal conductivity: hot particles transfer energy into neighbor cells, as a result of chaotic thermal motions.

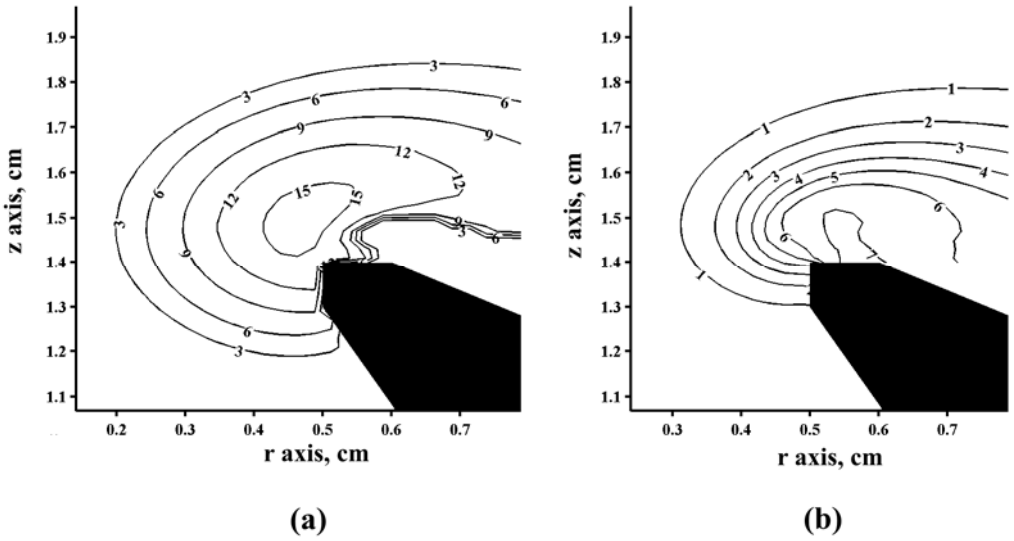

Fig. 21. Plasma parameter distributions around electrode at t= 200 ns:
(a) temperature field (eV) and (b) magnetic field (*k*G).

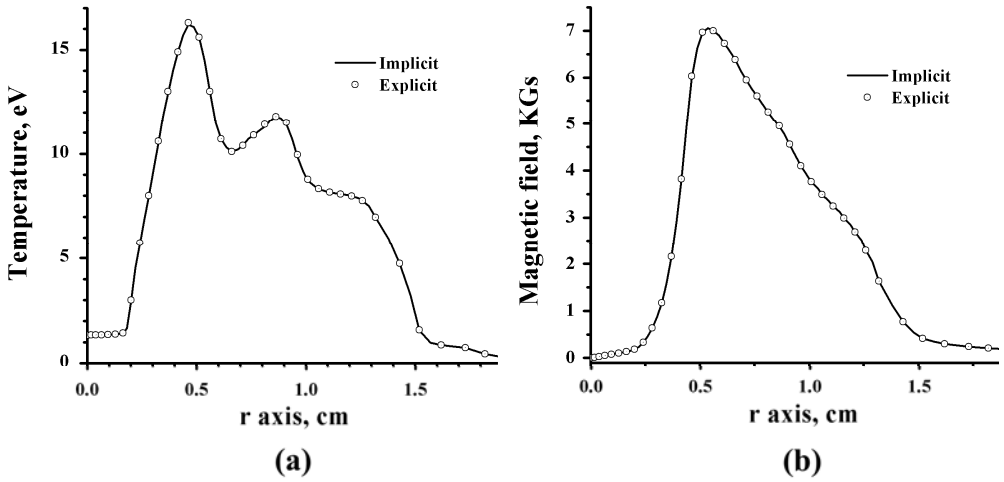

Fig. 22. Plasma parameter distributions along R-axis at t = 200 ns:
(a) temperature field (eV) and (b) magnetic field (kGs).

The explicit scheme works well if the particles arrive and exchange energy in the adjacent cells only during one time step. This scheme is not able to consider energy redistribution in the

next nearest cells. The consecutive energy transport is taken into account. The frequency of particle interactions declines by decreasing of density, and the time of flight through the cell is appreciably shorter. The explicit scheme includes non-useful time steps in the described case. This is related to the physical concept of the Courant-Friedrich-Levy (CFL) conditions. A similar unstable situation takes place by consideration of magnetic diffusion during the stage of plasma compression near the zero point on the radial axis [55]. Additional procedures are needed for damping nonphysical oscillations in the explicit case. However, the explicit method allowed us to simulate plasma motion in discharge-produced plasma devices of several constructions [8]. We note the stability of the numerical algorithm in combination with other processes of energy or magnetic field transport, such as radiation transport, thermomagnetic source, and laser beam interactions.

6.3. Radiation Transport

It is important to test the radiation transport part on a practical application. Simple tests (as a "black body") give a qualitative evaluation only. Hence, we investigated a plasma focus device radiation problem using the HEIGHTS radiation transport block benchmark. We considered convergence and accuracy of solution obtained with a Monte Carlo method and with direct Gauss integration of radiation equation (3.3.5). Figure 23 presents schematically the geometry of the device and initial data from the numerical experiment. The working gas temperature and density fields were saved during plasma focus pinching and were used as initial data for solving the radiation transport problem. Radiation fluxes were calculated with different methods and different accuracy: z-radiation flux along $|AB|$ surface and r-radiation flux along $|BC|$ surface. We used an equidistant mesh along the z-axis and a nonuniform fine mesh near zero point

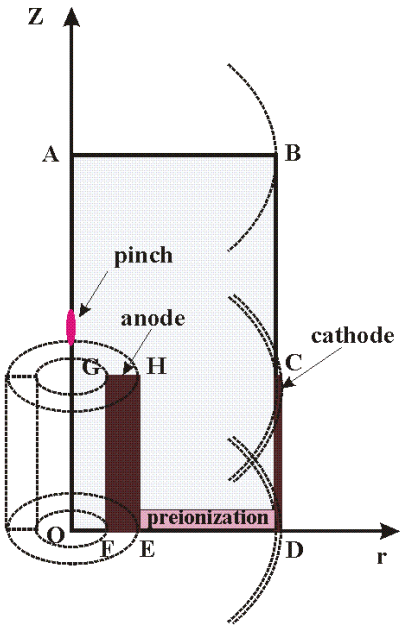

Fig. 23. Plasma focus device geometry. Coordinate system organization.

along the r-axis. Both methods give a bigger deviation of solution near point A: to the smaller calculated cell corresponds a smaller number of particles in MCRT or angles in DRT.

Figure 24 presents convergence of the radiation transport solution with the Monte Carlo method by increasing the total number of used macro-photons (see Section 3.3). One can see that $5 \cdot 10^5$ macro-photons give satisfactory accuracy.

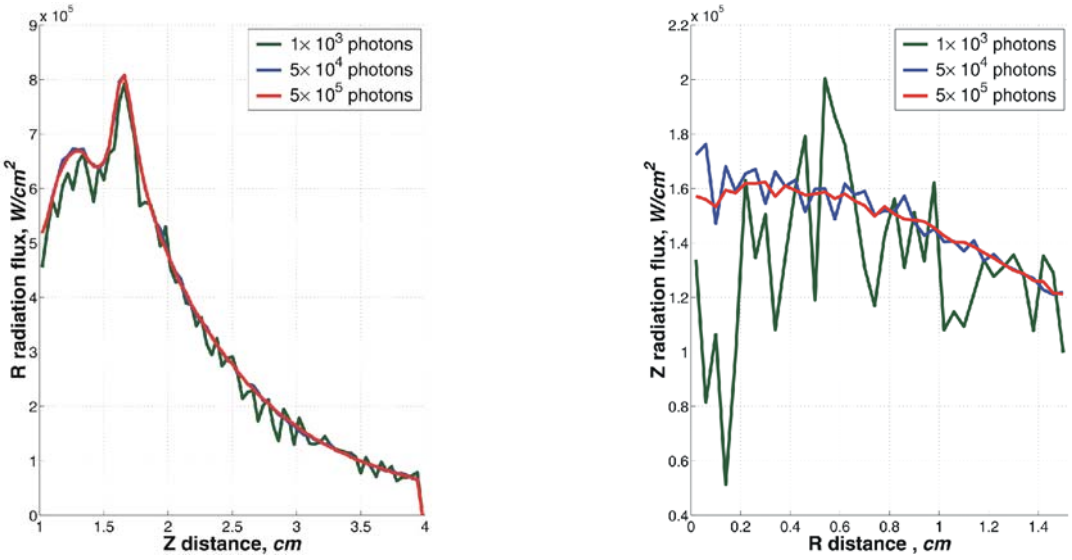

(a) (b)

Fig. 24. Convergence tendency by using the Monte Carlo method for RT calculations: (a) R-flux on |BC| surface; (b) Z-flux on |AB| surface.

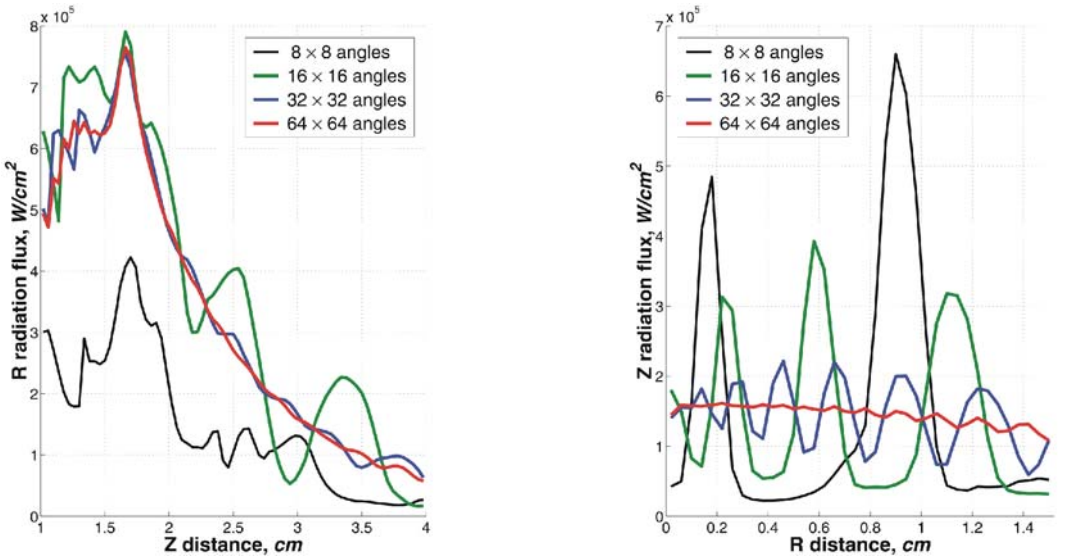

(a) (b)

Fig. 25. Convergence tendency by using Gauss direct integration method for RT calculations: (a) R-flux on |BC| surface; (b) Z-flux on |AB| surface

A similar trend is presented in Fig. 25 for the direct integration scheme. The figure shows that satisfactory results can be obtained with the direct integration method with 64×64 angles. Both methods converge to the same solution, presented in Fig. 26.

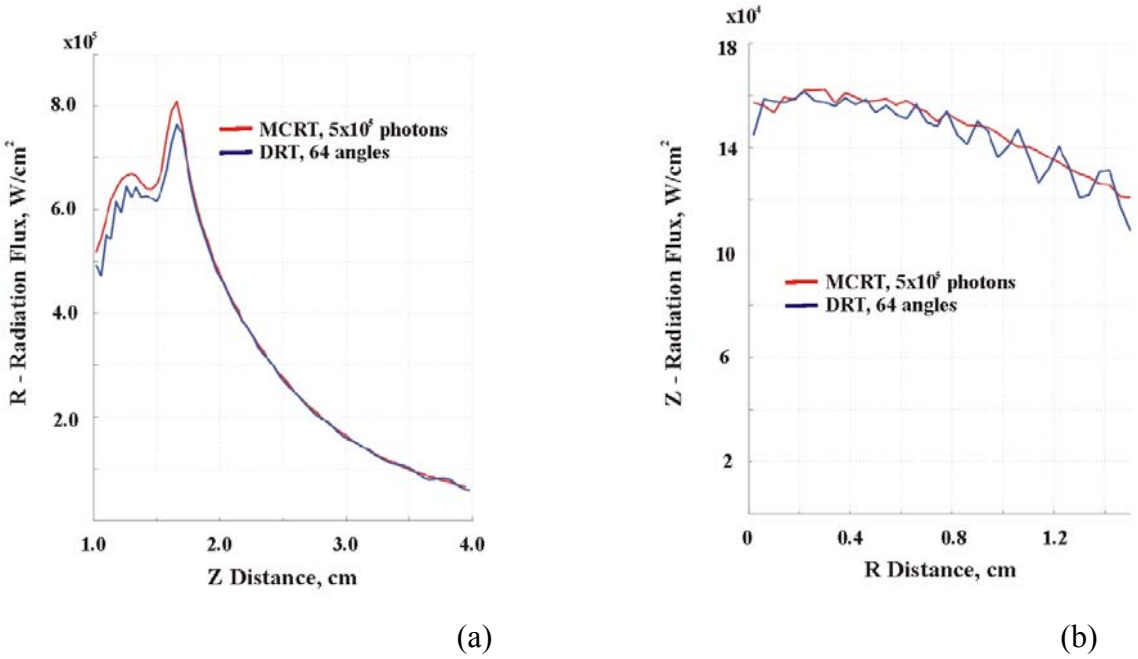

(a) (b)

Fig. 26. Comparison of Monte Carlo and direct integration solutions of the plasma focus RT problem: (a) R-flux on |BC| surface; (b) Z-flux on |AB| surface.

The quantitative and qualitative behaviors of the radiation flux are the same, despite the Monte Carlo method being significantly faster: by approximately a factor 300. This result also confirms the high accuracy and reliability of the implementation of the methods.

6.4. Final Benchmark

Final benchmarking was done for a completely EUV lithography application. The EUV output was calculated from the LPP device with planar geometry of the target and compared to published the data for tin target [56]. The arrangement of the experiment is shown schematically in Fig. 27.

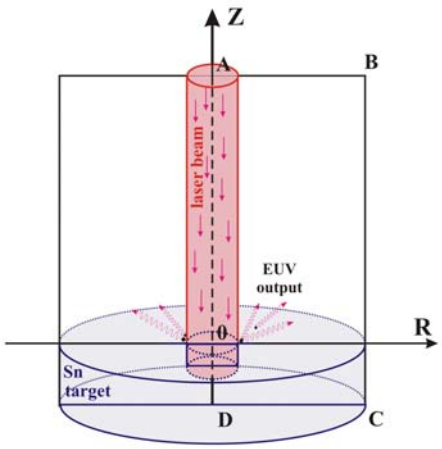

Fig. 27. Design of benchmarked LPP device.

The device used in the assembly and modeled with the HEIGHTS code was an Nd:YAG laser, delivering 0.3J at 1.064 μm in a 7.5 ns pulse. Laser light was focused onto the target surface at normal incidence by an aberration- and chromatic corrected lens with a 20.3 cm focal length. The laser radiation intensity level was controlled by tuning the laser spot radius. The minimum spot size at the target was about 20 μm.

The physical and mathematical model assembled for this problem included all the blocks described in this report: TVD-LF hydrodynamics, implicit sparse matrix solution for parabolic terms, Monte Carlo radiation transport, Monte Carlo laser absorption, and Monte Carlo modeling of EUV output registration. The model was tested with two and three dimension numerical schemes, with equal results. Also were tested several variants of spatial meshes: for 2D 100×250 cells with minimal size of cell in region of interest ~1μm and 65×110 with size ~5μm; for 3D 40×40×45 cells with cell size ~10μm for big spot sizes only. A final parameter that served as a criterion for the code work evaluation was the total EUV output into 2π sr solid angle, that is, the CE of the LPP device:

$$c_{EUV} = \frac{Q_{EUV}^{13.4nm \pm 1.1eV}}{Q_{las} \cdot 2.2eV} \cdot 100\%, \qquad (6.4.1)$$

where $Q_{EUV}^{13.4nm \pm 1.1eV}$ is the amount of EUV radiation energy registered in the 2.2 eV bandwidth centered at 134 Å. The efficiency is normalized on 1 eV. Opacities and atomic data used for radiation transport and EUV calculations are described in detail in [57, 58, 6-8].

Figure 28 presents a comparison of experimental results [56], well-known theoretical data (LASNEX [59]), and results simulated by the HEIGHTS package.

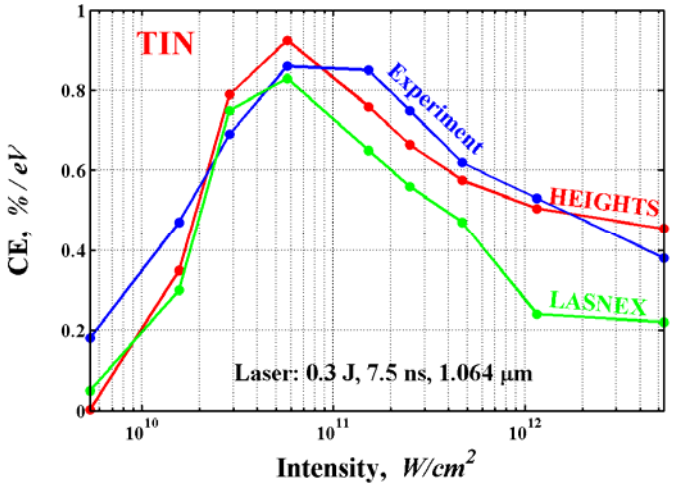

Fig. 28. Efficiency of LPP device with tin planar target. Comparison of experimental and theoretical data [56].

As shown, the HEIGHTS numerical results agree well with the published data. The numerical scheme demonstrated stability of results with changing spatial discretization and with expanding to the full 3D structure. These results indicate that the full 3D HEIGHTS package can be used effectively to study complex three-dimensional magnetohydrodynamics problems.

7. Results and Discussion

We focused our numerical investigations on a tin target because of its current interest as a source for λ=13.5 nm EUV lithography [60-62]. For the final benchmarking test (see Section 6.4), we considered the influence on the CE of three factors: dependence on a wavelength of laser, target geometry, and laser beam geometry. We present here our key results. Initial conditions (laser parameters, target size, etc.) of our numerical simulations were determined to be close to known experimental data [63-66].

To select the most effective laser wavelength for EUV on tin, we simulated the interaction of a single laser beam with a droplet target. Figure 29 schematically shows the geometry of the first numerical experiment.

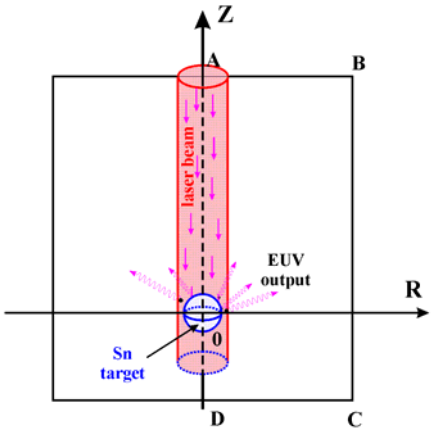

Fig. 29. Single laser beam interaction with the Sn droplet target.

The spherical tin target had a 100 μm diameter and was located at the point of origin of a 2D cylindrical coordinate system. The laser beam coincided with the z-axis. The laser pulse, which is square in time, was simulated with a total energy up to 230 mJ and duration 10 ns. The space Gaussian distribution of the laser beam (see Eq. (3.4.5)) allowed us to achieve laser power density in the laser spot up to $3 \cdot 10^{11}$ W/cm^2 by $\sigma_s = 50$ μm. Three laser wavelengths were tested: 355, 532, and 1064 nm. Typical density, temperature, and velocity of plasma are plotted in Fig. 30. Distributions are shown for the case $\lambda = 1064$ nm, $E_{pulse} = 45$ mJ, time moment 9 ns after the laser pulse start.

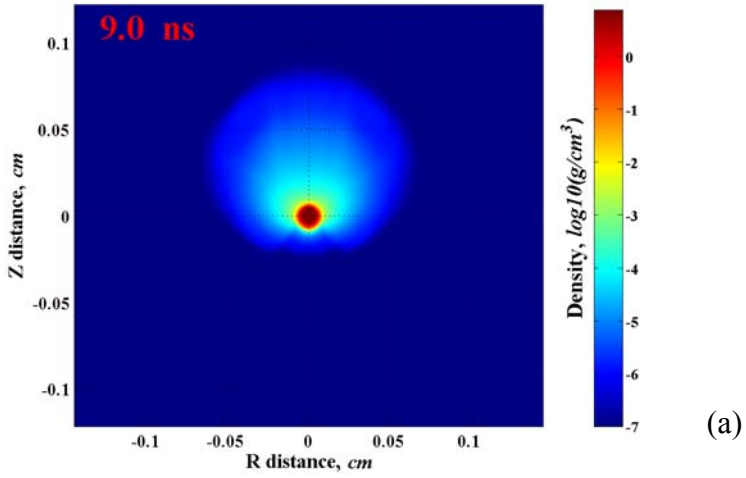

(a)

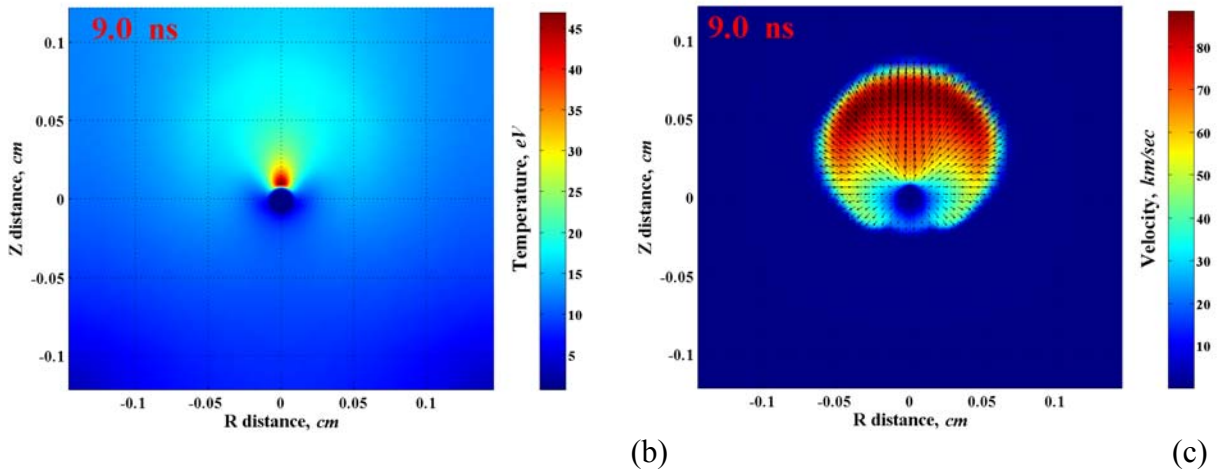

(b) (c)

Fig. 30. (a) Density, (b) temperature, and (c) velocity of tin plasma distributions at 9.0 ns. Single laser case: energy of laser pulse 45 mJ, wavelength 1064 nm.

The efficiency of the simulated EUV device is shown in Fig. 31 as a function of the radiation power density. The CE was calculated as the ratio of total EUV output (13.5±2% nm band) into 2π sr solid angle to the energy of the initial laser pulse.

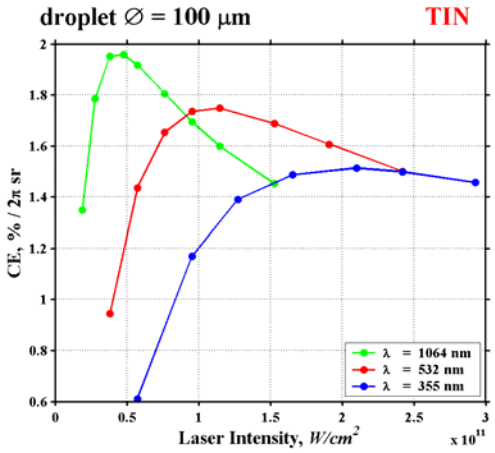

Fig. 31. Efficiency of the LPP device as a function of radiation power density by tin droplet target.

An ideal variant of light source for EUV lithography is a small spherical object with enough density and an optimal temperature for the given material for EUV output. This approach is used in recent investigations [67, 68] for improving EUV output efficiency, that is, the first part of this

problem: possible target materials for effective radiation at the 13.5 nm area on the background of the total spectrum. However, the second part of the problem consists in the formation and efficient confinement of the EUV plasma in these optimal conditions (temperature plus enough density). Typical axial distributions of the temperature, density, and EUV flux are plotted in Fig. 32 for the case of a droplet target and single laser.

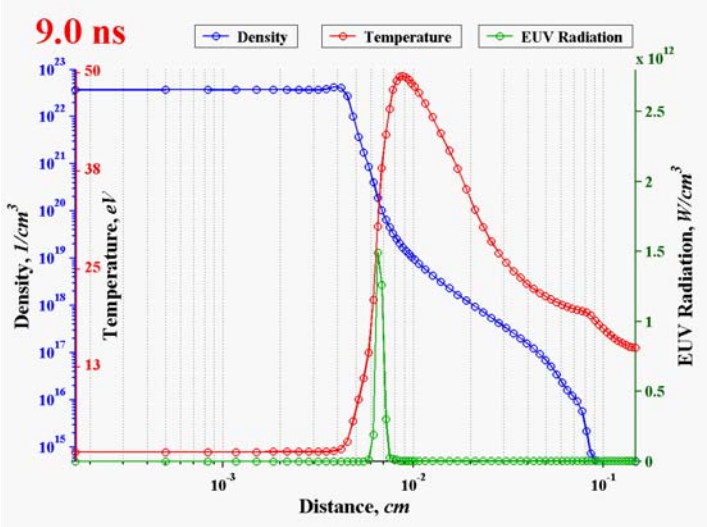

Fig. 32. Distributions of the density, temperature, and EUV flux along the laser beam axis at the 9.0 ns time moment.

As shown, the EUV output region is a thin layer between areas with high temperature but small density and high density but small temperature. Increasing this region thickness enables us to solve the second part of the EUV CE problem. Different target materials have their own EUV region size, which appears in different sizes of EUV source images [69]. Our preliminary calculations show a very thin EUV layer for a lithium target. Laser radiation is absorbed actively by the target surface plasma and overheats the surface because lithium has only three electrons. The greater part of the laser energy is deposited in this overheated area. The remaining part is distributed in the full target because ~1 eV lithium is transparent enough for laser radiation. Moreover, the hot external plasma layer actively absorbs EUV radiation from the thin EUV region. As a result, these negative factors can appreciably decrease the position of the element as a candidate for laser target material. Two approaches can be used to avoid these factors: application of more complex targets where the material combines clusters, and an increase of the heated plasma density. The first approach is actively being investigated [70]. We consider the

second approach in our numerical simulations. The authors of Ref. [71] observed increasing the EUV emission near the wall close to the laser target. In our opinion this effect is concerned with confinement of motion of the heated plasma. The density of the hot plasma increases near the wall, and a new EUV region appears at this area. Reference [71] is not so applicable in the full problem sense: additional wall creates additional shield for EUV output and decreases the final CE. A better way is the produce a transparent (for EUV) wall that can confine plasma.

To achieve these conditions and to examine of our hypothesis, we constructed the space-distributed laser beam assembly shown in Fig. 33.

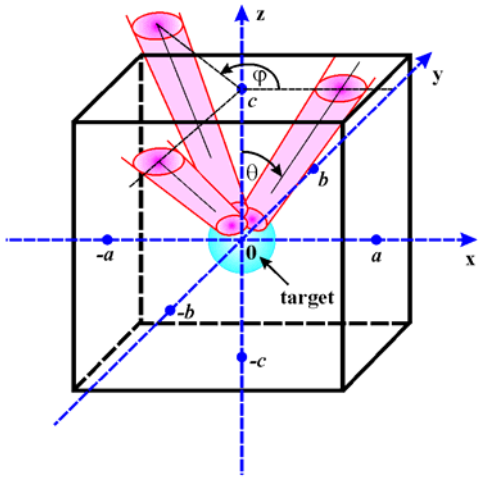

Fig. 33. Three-beam LPP device. φ - radial angle, θ - axial angle

If our hypothesis is correct, the three laser beams in Fig. 33 can effectively confine the plasma density by any optimal axial angle θ. The proposed laser beam configuration should organize along the z-axis the plasma jet confined in the radial direction. The case θ = 0 corresponds to a single-laser device construction. The 3D problem was simulated for a tin droplet with diameter 100 nm. Energy of pulse (45 mJ) was distributed in equal parts between three lasers started at one time. The duration of the pulse was 10 ns. The laser wavelength was 1064 nm. Initial conditions of this numerical experiment correspond to the most optimal single-laser case shown in Fig. 31. The square distribution of laser energy in time and the Gaussian distribution in space were used in this numerical experiment. Influence of the plasma confinement on the efficiency of LPP device is plotted in Fig. 34 as the dependence from the axial angle θ.

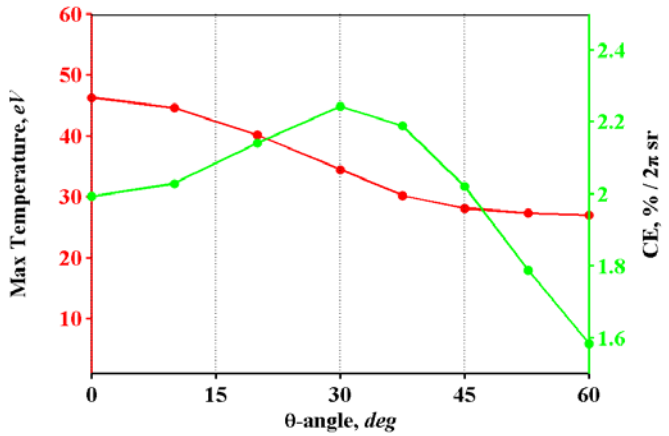

Fig. 34. Efficiency of the three-beam LPP device as a function of axial angle (green line). Maximal temperature of plasma (red line).

The second numerical experiment confirms the existence of the optimal axial angle ($\theta \sim 30^{\circ}$), where plasma confinement gives an advantage in the EUV output CE. As we assumed, a new plasma jet appears and obtains energy in area between the laser beams. The efficiency of the three-beam device should be higher in comparison to the single-beam device only with enough laser pulse energy: optimal plasma temperature and density cannot be achieved in the central jet with an initially cold plasma. We plotted EUV efficiency dependence on the laser pulse energy (Fig. 35) for the optimal axial angle $\theta = 30^{\circ}$ and obtained confirmation of this statement.

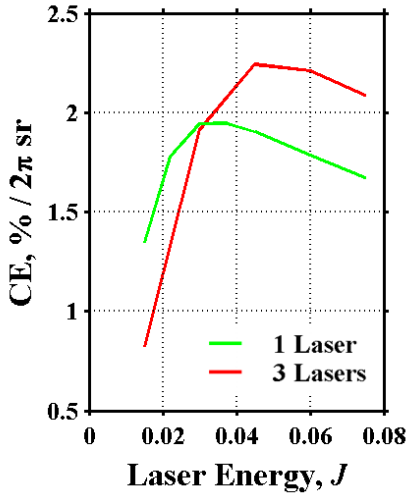

Fig. 35. Efficiency of the three-beam LPP device as a function of the total pulses energy for the axial angle $\theta = 30^{\circ}$.

Figure 36 presents temperature fields in x-y-plane cross-sections that belong to the maximal temperature point (see Fig. 34).

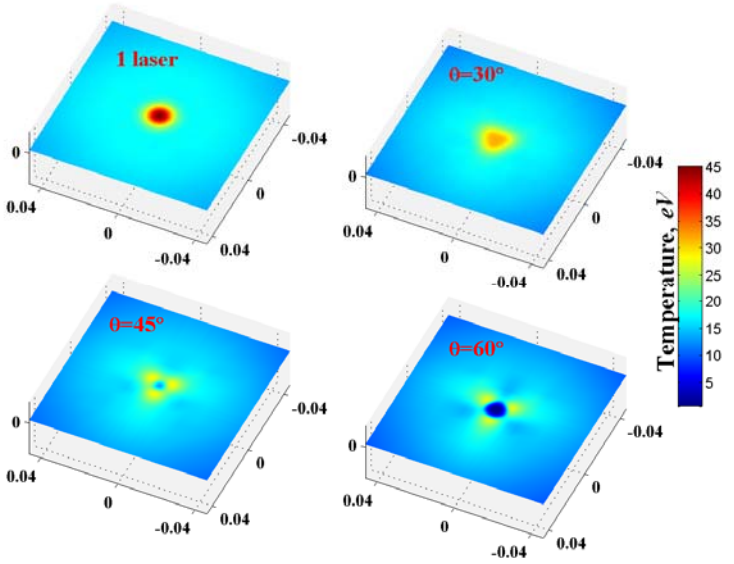

Fig. 36. Temperature fields for (x-y) cross-section in point of maximal temperature at 9 ns. One-laser case corresponds $\theta = 0^{\circ}$.

The plasma motion initiated with three laser beams is illustrated in Fig. 37. Here are presented (z-x) cross-sections of density, temperature, and velocity fields. The black arrow indicates the direction of the formed plasma jet.

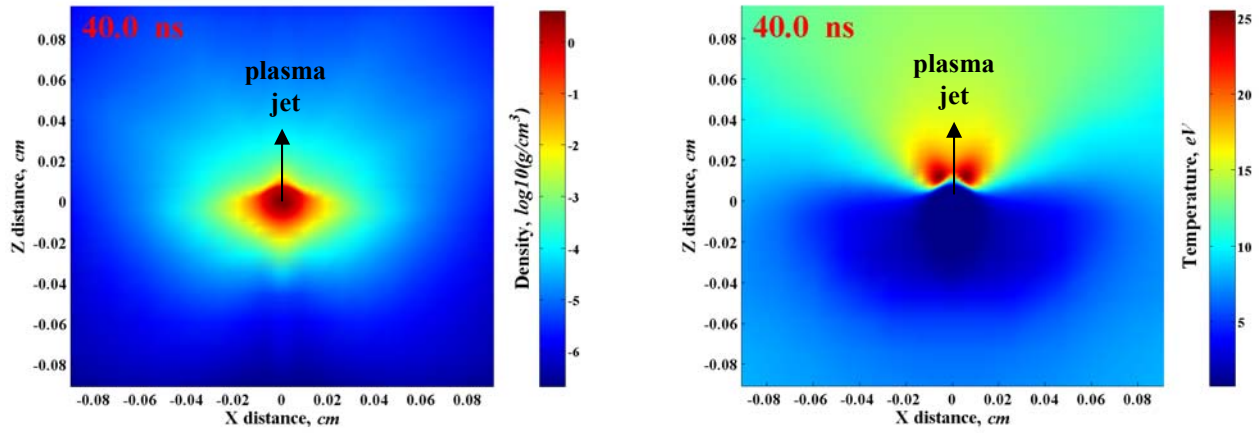

(a) (b)

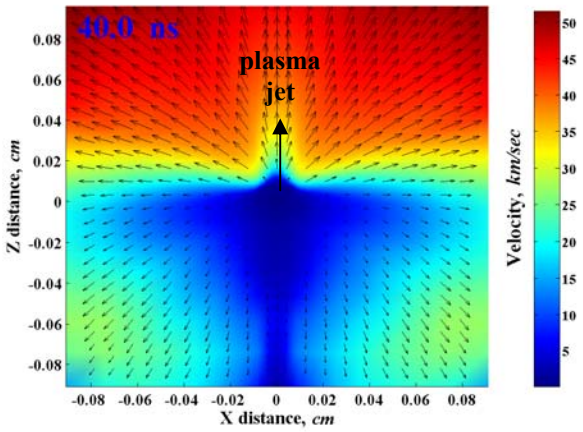

c)

Fig. 37. (a) Density, (b) temperature, and (c) velocity of tin plasma distributions at 40.0 ns in z-x plane. Three-laser case: energy of lasers pulse 45 mJ, wavelength 1064 nm, $\theta = 30^{\circ}$.

The initiation of the plasma jet with this method involved application of three laser beams, precise adjustment, time synchronization, and so on. Moreover, the plasma confinement is not so effective (Fig. 37). Taking into account these disadvantages, we increased CE from ~2.0 to ~2.2 % (Fig. 34).

Modern development of laser instruments has resulted in creation of the hollow laser beams [72-75]. We used the hollow laser beam in our numerical experiment to accelerate of the plasma jet confinement and to avoid the disadvantages noted for the three-laser construction. Figure 38 presents such an LPP device with a planar tin target and with a hollow laser beam as an energy source. We assumed initiation, confinement, and energy supply of the cumulative plasma jet inside the hollow laser beam of the device. Following our hypothesis, the dense plasma jet should be initiated at the target surface with round heating and should be confined with more heated plasma of the cylindrical laser body. In a numerical experiment, we investigated the CE of the new device as a function of the hole and beam ratio, namely, the ratio ξ of the

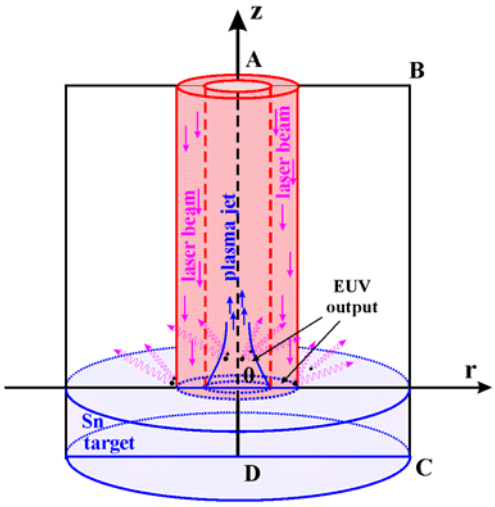

Fig. 38. Hollow beam LPP device.

hole radius to the external radius of the laser beam. In this case, $\xi = 0$ corresponds to the laser beam without a hole, and $\xi = 1$ corresponds to the infinitesimal laser body. We assumed equal laser pulse energy (300 mJ), laser pulse duration (7.5 ns), and radiation power density in the laser body ($5.73 \cdot 10^{10}$ W/cm^2). Square distributions of laser pulse energy were assumed in time and in space. The numerical experiment was conducted with a 2D cylindrical geometry.

As expected, we obtained generation of the plasma jet inside the hollow laser beam. Moreover, we observed pinching of plasma on the laser beam axis. Figure 39 presents the most distinctive density, temperature, and velocity distributions of the hollow-laser-produced plasma in the r-z plane for the radius ratio $\xi = 0.7$.

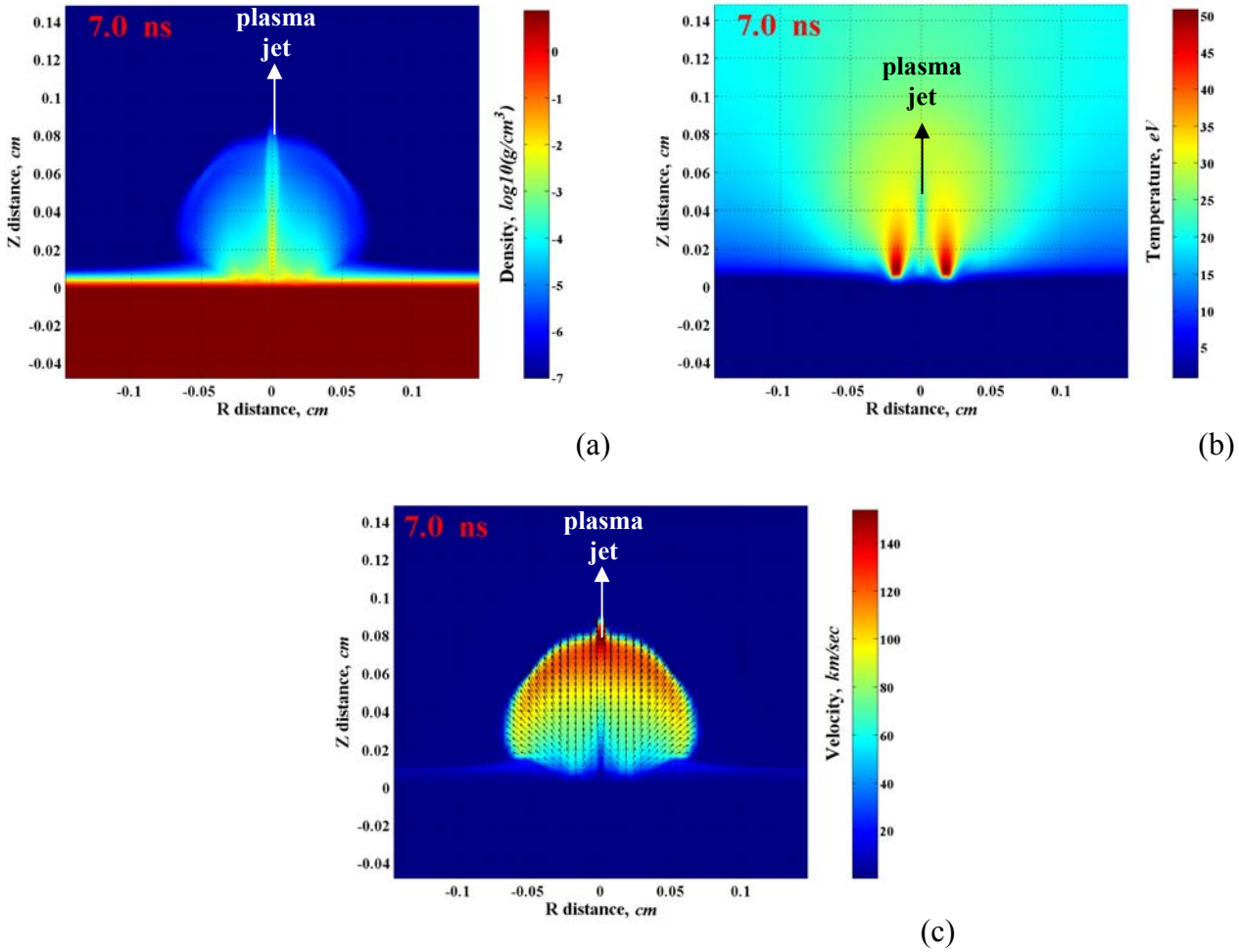

Fig. 39. (a) Density, (b) temperature, and (c) velocity of tin plasma distributions at 7.0 ns in z-r plane. Hollow-laser-beam case: energy of lasers pulse 300 mJ, wavelength 1064 nm, $\xi = 0.7$.

In comparison to three-laser case (Fig. 37), the plasma jet inside the hollow laser beam is well-defined and much more accelerated. To consider cumulative character of the plasma jet inside the laser beam, we carried out numerical experiments with conditions close to those described in Section 6.4, that is, we calculated the EUV output in the 2.2 eV bandwidth centered at 134 Å. The radiation energy distribution in laser beam (Sec. 6.4) was Gaussian in space. The Gaussian space distribution is close to the real experimental laser beam parameters and gives a higher CE in comparison to the simple square distribution. We did not have the space distribution of the laser radiation density for the new hollow laser beams and carried out our numerical experiment with the hollow beam on the square distribution. Hence, the data in the Fig. 28 for the hollow-beam results cannot be compared directly. However, the results show that the hollow-beam laser abruptly increases the EUV output coefficient efficiency. Figure 40 shows an increase of the CE by a factor of 1.16 for the nonoptimized square distribution case. The three-laser case (Fig. 34) has a factor 1.1 increase.

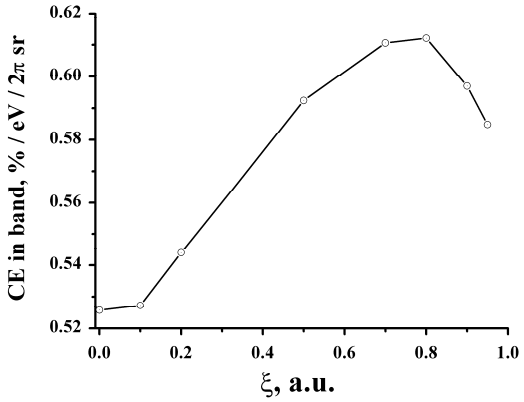

Fig. 40. Efficiency of the hollow beam LPP device as a function of the radius ratio $\xi = r_{hole}/r_{beam}$ for the planar Sn target.

We believe that the obtained effect should be used to increase the CE of industrial LPP sources for EUV lithography.

Summary and Conclusion

The main contributions of this work are as follows:

Theoretical Model: Physical models were developed to simulate the main processes that occur in EUV lithography LPP devices: MHD model of the plasma motion, theoretical models of the magnetic diffusion and thermal conduction in plasma, radiation transport model, and laser absorption model.

Model Implementation: Theoretical models were adopted for numerical solution in the one- and two-temperature approximations. Cylindrical symmetrical two-dimensional and three-dimensional cases were considered.

Numerical Scheme: An algorithm based on separation by physical processes was developed. For each physical process, the most efficient numerical scheme was constructed. Hydrodynamic processes were simulated based on the total variation diminishing scheme in the Lax-Friedrich formulation; an implicit scheme with the sparse matrix solver was developed for magnetic diffusion and heat conduction problems; and Monte Carlo methods were used for simulation of radiation transport and laser absorption processes.

Application: The integrated computer code HEIGHTS was developed for simulating physical processes that occur by interaction of the laser beam with matter. The computer code was optimized for calculations of the EUV output of the LPP devices for lithography purposes. The HEIGHTS code was used to investigate the influence of complex spatial effects of plasma motion on the final coefficient of efficiency of the LPP device.

Benchmarking: The HEIGHTS package was tested and benchmarked with known analytical and experimental data. The separate computation models and the whole code were tested.

We obtained the following results:

1. The LPP device with spatially distributed laser beams was modeled. The optimal spatial location of the three beams was obtained in a 3D numerical experiment to increase the total EUV output from a tin droplet target. The coefficient efficiency was increased as a result of plasma confinement with the laser beam assembly.

2. The effect of the cumulative plasma jet formation inside of hollow laser beam was observed in a computer simulation. The coefficient of efficiency increased by a factor of 1.16 on the planar tin target.

We conclude that the obtained spatial effects should be used to increase the efficiency of industrial LPP sources for EUV lithography. We also note that the theoretical model and integrated code HEIGHTS showed wide capabilities and flexibility. The model and code therefore can be used for: optimization of obtained data, investigation of LPP devices with complex geometry and structure targets, study of the combined influence of spatial effects and target structure on the final EUV output, and registration of the EUV source size and form.

ACKNOWLEDGMENTS

The major part of this work is supported by SEMATECH and the Intel Corporation. Argonne National Laboratory's work was supported by the U.S. Department of Energy, under contract DE-AC02-06CH11357.

Appendix 1

Two-dimensional cylindrical symmetric case of MHD equations. TVD-LF numerical scheme

$\frac{\partial \mathbf{U}}{\partial t}+\frac{1}{r}\frac{\partial}{\partial r}\left[r\mathbf{F}(\mathbf{U})\right]+\frac{\partial \mathbf{P}(\mathbf{U})}{\partial r}+\frac{\partial \mathbf{G}(\mathbf{U})}{\partial z}=\Omega$, where

$$\mathbf{U}=\begin{bmatrix}\rho\\ \rho v^r\\ \rho v^z\\ e_{tot}\\ B\end{bmatrix},\ \mathbf{F}(\mathbf{U})=\begin{bmatrix}\rho v^r\\ \rho v^r v^r\\ \rho v^z v^r\\ v^r\left(e_{tot}+p_{tot}\right)\\ 0\end{bmatrix},\ \mathbf{P}(\mathbf{U})=\begin{bmatrix}0\\ p_{tot}\\ 0\\ 0\\ v^r B\end{bmatrix},\ \mathbf{G}(\mathbf{U})=\begin{bmatrix}\rho v^z\\ \rho v^r v^z\\ \rho v^z v^z+p_{tot}\\ v^z\left[e_{tot}+p_{tot}\right]\\ v^z B\end{bmatrix},\ \Omega=\begin{bmatrix}0\\ -\frac{B^2}{r4\pi\mu}\\ 0\\ 0\\ 0\end{bmatrix},$$

and $e_{tot}=e_h+\frac{B^2}{8\pi\mu}$, $\quad p_{tot}=p_h+\frac{B^2}{8\pi\mu}$.

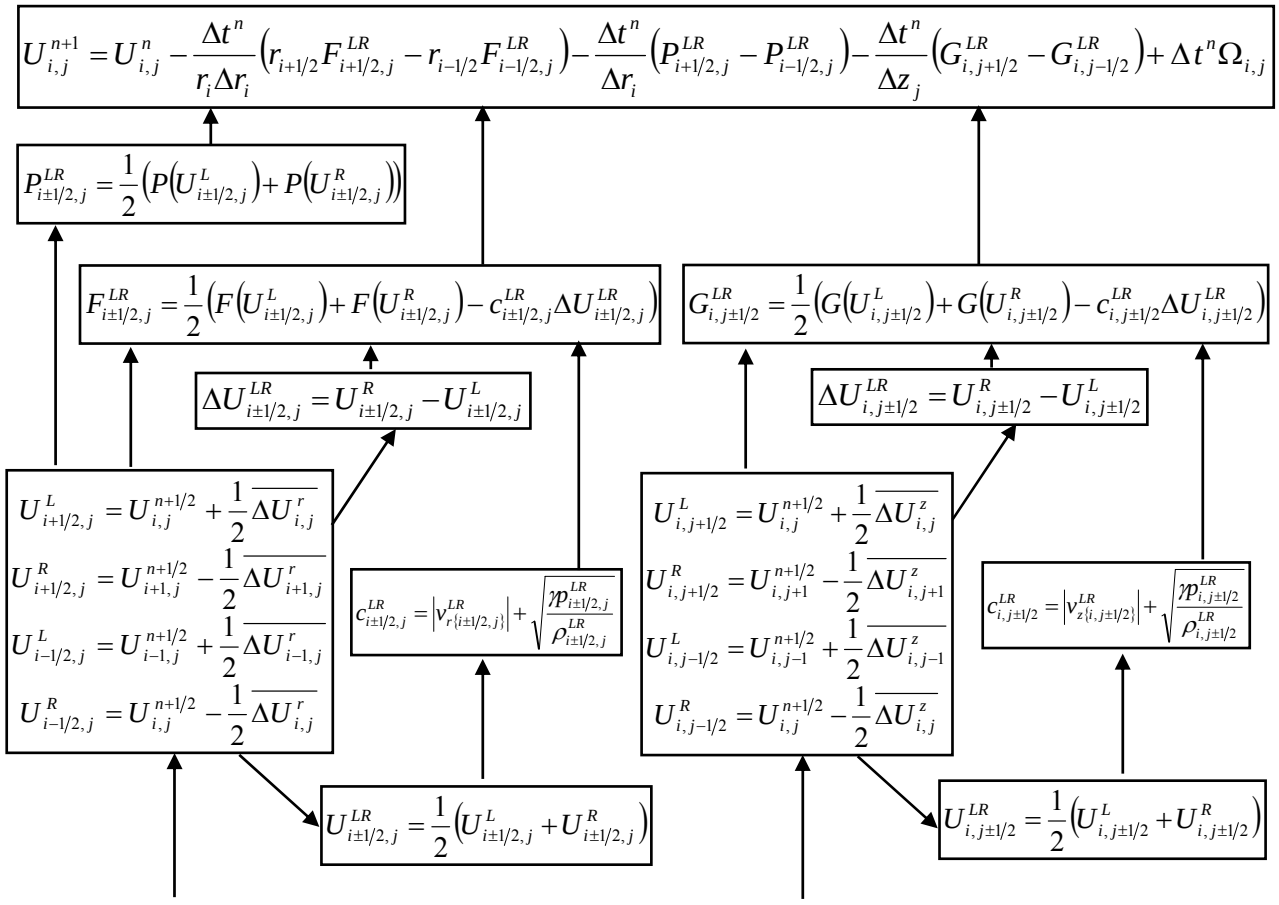

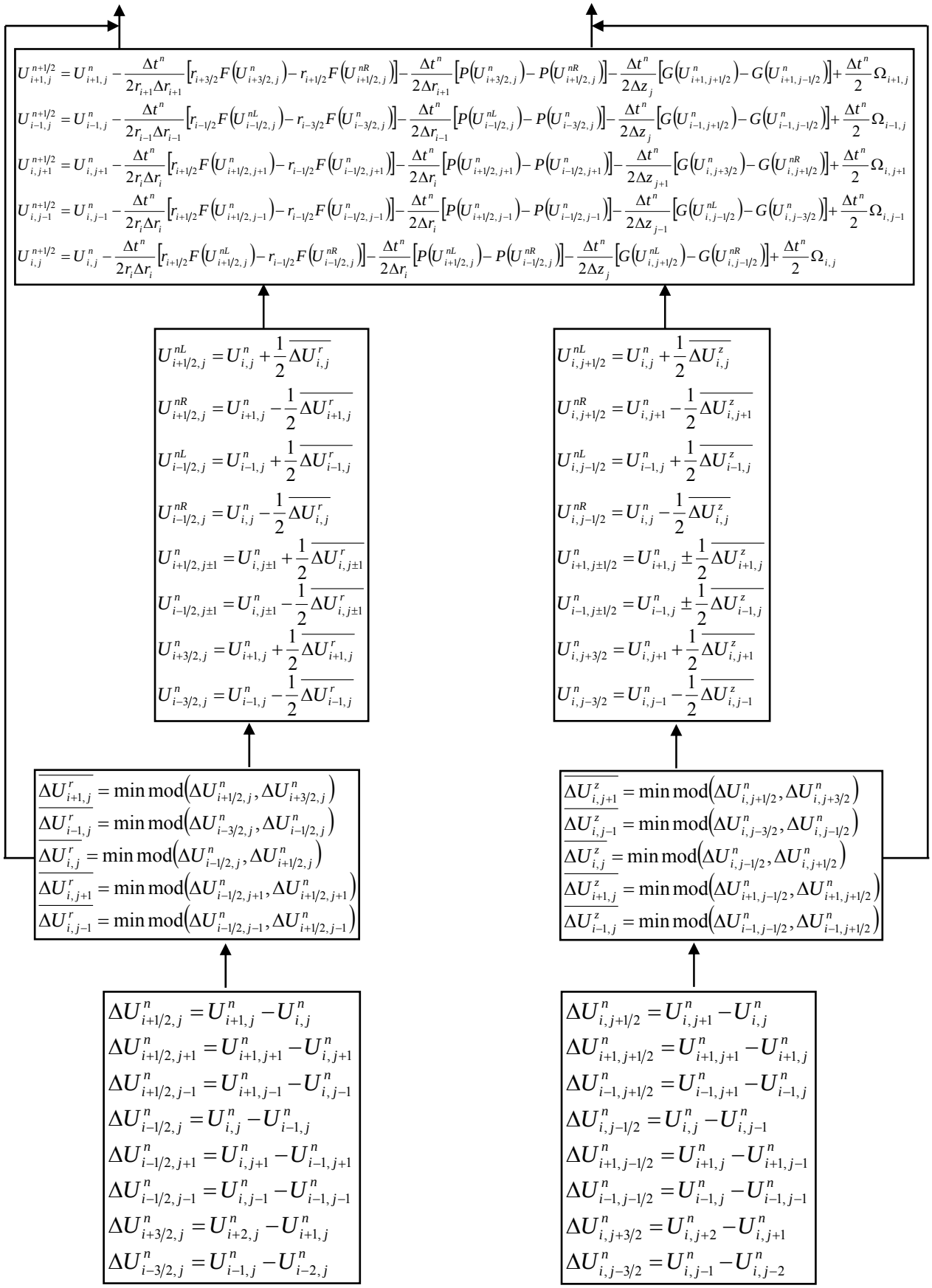
$U_{i+1,j}^{n+1/2} = U_{i+1,j}^{n} - \frac{\Delta t^n}{2r_{i+1}\Delta r_{i+1}}\left[r_{i+3/2}F\left(U_{i+3/2,j}^{n}\right) - r_{i+1/2}F\left(U_{i+1/2,j}^{nR}\right)\right] - \frac{\Delta t^n}{2\Delta r_{i+1}}\left[P\left(U_{i+3/2,j}^{n}\right) - P\left(U_{i+1/2,j}^{nR}\right)\right] - \frac{\Delta t^n}{2\Delta z_j}\left[G\left(U_{i+1,j+1/2}^{n}\right) - G\left(U_{i+1,j-1/2}^{n}\right)\right] + \frac{\Delta t^n}{2}\Omega_{i+1,j}$
$U_{i-1,j}^{n+1/2} = U_{i-1,j}^{n} - \frac{\Delta t^n}{2r_{i-1}\Delta r_{i-1}}\left[r_{i-1/2}F\left(U_{i-1/2,j}^{nL}\right) - r_{i-3/2}F\left(U_{i-3/2,j}^{n}\right)\right] - \frac{\Delta t^n}{2\Delta r_{i-1}}\left[P\left(U_{i-1/2,j}^{nL}\right) - P\left(U_{i-3/2,j}^{n}\right)\right] - \frac{\Delta t^n}{2\Delta z_j}\left[G\left(U_{i-1,j+1/2}^{n}\right) - G\left(U_{i-1,j-1/2}^{n}\right)\right] + \frac{\Delta t^n}{2}\Omega_{i-1,j}$
$U_{i,j+1}^{n+1/2} = U_{i,j+1}^{n} - \frac{\Delta t^n}{2r_i\Delta r_i}\left[r_{i+1/2}F\left(U_{i+1/2,j+1}^{n}\right) - r_{i-1/2}F\left(U_{i-1/2,j+1}^{n}\right)\right] - \frac{\Delta t^n}{2\Delta r_i}\left[P\left(U_{i+1/2,j+1}^{n}\right) - P\left(U_{i-1/2,j+1}^{n}\right)\right] - \frac{\Delta t^n}{2\Delta z_{j+1}}\left[G\left(U_{i,j+3/2}^{n}\right) - G\left(U_{i,j+1/2}^{nR}\right)\right] + \frac{\Delta t^n}{2}\Omega_{i,j+1}$
$U_{i,j-1}^{n+1/2} = U_{i,j-1}^{n} - \frac{\Delta t^n}{2r_i\Delta r_i}\left[r_{i+1/2}F\left(U_{i+1/2,j-1}^{n}\right) - r_{i-1/2}F\left(U_{i-1/2,j-1}^{n}\right)\right] - \frac{\Delta t^n}{2\Delta r_i}\left[P\left(U_{i+1/2,j-1}^{n}\right) - P\left(U_{i-1/2,j-1}^{n}\right)\right] - \frac{\Delta t^n}{2\Delta z_{j-1}}\left[G\left(U_{i,j-1/2}^{nL}\right) - G\left(U_{i,j-3/2}^{n}\right)\right] + \frac{\Delta t^n}{2}\Omega_{i,j-1}$
$U_{i,j}^{n+1/2} = U_{i,j}^{n} - \frac{\Delta t^n}{2r_i\Delta r_i}\left[r_{i+1/2}F\left(U_{i+1/2,j}^{nL}\right) - r_{i-1/2}F\left(U_{i-1/2,j}^{nR}\right)\right] - \frac{\Delta t^n}{2\Delta r_i}\left[P\left(U_{i+1/2,j}^{nL}\right) - P\left(U_{i-1/2,j}^{nR}\right)\right] - \frac{\Delta t^n}{2\Delta z_j}\left[G\left(U_{i,j+1/2}^{nL}\right) - G\left(U_{i,j-1/2}^{nR}\right)\right] + \frac{\Delta t^n}{2}\Omega_{i,j}$
$U_{i+1/2,j}^{nL} = U_{i,j}^{n} + \frac{1}{2}\overline{\Delta U_{i,j}^{r}}$
$U_{i+1/2,j}^{nR} = U_{i+1,j}^{n} - \frac{1}{2}\overline{\Delta U_{i+1,j}^{r}}$
$U_{i-1/2,j}^{nL} = U_{i-1,j}^{n} + \frac{1}{2}\overline{\Delta U_{i-1,j}^{r}}$
$U_{i-1/2,j}^{nR} = U_{i,j}^{n} - \frac{1}{2}\overline{\Delta U_{i,j}^{r}}$
$U_{i+1/2,j\pm1}^{n} = U_{i,j\pm1}^{n} + \frac{1}{2}\overline{\Delta U_{i,j\pm1}^{r}}$
$U_{i-1/2,j\pm1}^{n} = U_{i,j\pm1}^{n} - \frac{1}{2}\overline{\Delta U_{i,j\pm1}^{r}}$
$U_{i+3/2,j}^{n} = U_{i+1,j}^{n} + \frac{1}{2}\overline{\Delta U_{i+1,j}^{r}}$
$U_{i-3/2,j}^{n} = U_{i-1,j}^{n} - \frac{1}{2}\overline{\Delta U_{i-1,j}^{r}}$
$U_{i,j+1/2}^{nL} = U_{i,j}^{n} + \frac{1}{2}\overline{\Delta U_{i,j}^{z}}$
$U_{i,j+1/2}^{nR} = U_{i,j+1}^{n} - \frac{1}{2}\overline{\Delta U_{i,j+1}^{z}}$
$U_{i,j-1/2}^{nL} = U_{i-1,j}^{n} + \frac{1}{2}\overline{\Delta U_{i-1,j}^{z}}$
$U_{i,j-1/2}^{nR} = U_{i,j}^{n} - \frac{1}{2}\overline{\Delta U_{i,j}^{z}}$
$U_{i+1,j\pm1/2}^{n} = U_{i+1,j}^{n} \pm \frac{1}{2}\overline{\Delta U_{i+1,j}^{z}}$
$U_{i-1,j\pm1/2}^{n} = U_{i-1,j}^{n} \pm \frac{1}{2}\overline{\Delta U_{i-1,j}^{z}}$
$U_{i,j+3/2}^{n} = U_{i,j+1}^{n} + \frac{1}{2}\overline{\Delta U_{i,j+1}^{z}}$
$U_{i,j-3/2}^{n} = U_{i,j-1}^{n} - \frac{1}{2}\overline{\Delta U_{i,j-1}^{z}}$
$\overline{\Delta U_{i+1,j}^{r}} = \min\mathrm{mod}\left(\Delta U_{i+1/2,j}^{n}, \Delta U_{i+3/2,j}^{n}\right)$
$\overline{\Delta U_{i-1,j}^{r}} = \min\mathrm{mod}\left(\Delta U_{i-3/2,j}^{n}, \Delta U_{i-1/2,j}^{n}\right)$
$\overline{\Delta U_{i,j}^{r}} = \min\mathrm{mod}\left(\Delta U_{i-1/2,j}^{n}, \Delta U_{i+1/2,j}^{n}\right)$
$\overline{\Delta U_{i,j+1}^{r}} = \min\mathrm{mod}\left(\Delta U_{i-1/2,j+1}^{n}, \Delta U_{i+1/2,j+1}^{n}\right)$
$\overline{\Delta U_{i,j-1}^{r}} = \min\mathrm{mod}\left(\Delta U_{i-1/2,j-1}^{n}, \Delta U_{i+1/2,j-1}^{n}\right)$
$\overline{\Delta U_{i,j+1}^{z}} = \min\mathrm{mod}\left(\Delta U_{i,j+1/2}^{n}, \Delta U_{i,j+3/2}^{n}\right)$
$\overline{\Delta U_{i,j-1}^{z}} = \min\mathrm{mod}\left(\Delta U_{i,j-3/2}^{n}, \Delta U_{i,j-1/2}^{n}\right)$
$\overline{\Delta U_{i,j}^{z}} = \min\mathrm{mod}\left(\Delta U_{i,j-1/2}^{n}, \Delta U_{i,j+1/2}^{n}\right)$
$\overline{\Delta U_{i+1,j}^{z}} = \min\mathrm{mod}\left(\Delta U_{i+1,j-1/2}^{n}, \Delta U_{i+1,j+1/2}^{n}\right)$
$\overline{\Delta U_{i-1,j}^{z}} = \min\mathrm{mod}\left(\Delta U_{i-1,j-1/2}^{n}, \Delta U_{i-1,j+1/2}^{n}\right)$
$\Delta U_{i+1/2,j}^{n} = U_{i+1,j}^{n} - U_{i,j}^{n}$
$\Delta U_{i+1/2,j+1}^{n} = U_{i+1,j+1}^{n} - U_{i,j+1}^{n}$
$\Delta U_{i+1/2,j-1}^{n} = U_{i+1,j-1}^{n} - U_{i,j-1}^{n}$
$\Delta U_{i-1/2,j}^{n} = U_{i,j}^{n} - U_{i-1,j}^{n}$
$\Delta U_{i-1/2,j+1}^{n} = U_{i,j+1}^{n} - U_{i-1,j+1}^{n}$
$\Delta U_{i-1/2,j-1}^{n} = U_{i,j-1}^{n} - U_{i-1,j-1}^{n}$
$\Delta U_{i+3/2,j}^{n} = U_{i+2,j}^{n} - U_{i+1,j}^{n}$
$\Delta U_{i-3/2,j}^{n} = U_{i-1,j}^{n} - U_{i-2,j}^{n}$
$\Delta U_{i,j+1/2}^{n} = U_{i,j+1}^{n} - U_{i,j}^{n}$
$\Delta U_{i+1,j+1/2}^{n} = U_{i+1,j+1}^{n} - U_{i+1,j}^{n}$
$\Delta U_{i-1,j+1/2}^{n} = U_{i-1,j+1}^{n} - U_{i-1,j}^{n}$
$\Delta U_{i,j-1/2}^{n} = U_{i,j}^{n} - U_{i,j-1}^{n}$
$\Delta U_{i+1,j-1/2}^{n} = U_{i+1,j}^{n} - U_{i+1,j-1}^{n}$
$\Delta U_{i-1,j-1/2}^{n} = U_{i-1,j}^{n} - U_{i-1,j-1}^{n}$
$\Delta U_{i,j+3/2}^{n} = U_{i,j+2}^{n} - U_{i,j+1}^{n}$
$\Delta U_{i,j-3/2}^{n} = U_{i,j-1}^{n} - U_{i,j-2}^{n}$

Appendix 2

Three-dimensional case of HD. TVD-LF numerical scheme

$$\frac{\partial \mathbf{U}}{\partial t}+\frac{\partial \mathbf{F}(\mathbf{U})}{\partial x}+\frac{\partial \mathbf{G}(\mathbf{U})}{\partial y}+\frac{\partial \mathbf{H}(\mathbf{U})}{\partial z}=\Omega,\ \text{where}$$

$$U=\begin{bmatrix}\rho\\ \rho v_x\\ \rho v_y\\ \rho v_z\\ e_{tot}\end{bmatrix},\ \mathbf{F}(\mathbf{U})=\begin{bmatrix}\rho v_x\\ \rho v_x^2+p_h\\ \rho v_x v_y\\ \rho v_x v_z\\ v_x(e_{tot}+p_h)\end{bmatrix},\ \mathbf{G}(\mathbf{U})=\begin{bmatrix}\rho v_y\\ \rho v_y v_x\\ \rho v_y^2+p_h\\ \rho v_y v_z\\ v_y(e_{tot}+p_h)\end{bmatrix},\ \mathbf{H}(\mathbf{U})=\begin{bmatrix}\rho v_z\\ \rho v_z v_x\\ \rho v_z v_y\\ \rho v_z^2+p_h\\ v_z(e_{tot}+p_h)\end{bmatrix},\ \mathbf{\Omega}=\begin{bmatrix}0\\ 0\\ 0\\ 0\\ 0\end{bmatrix},$$

and $e_{tot}=e_h=e_i+\dfrac{\rho \mathbf{v}^2}{2}$.

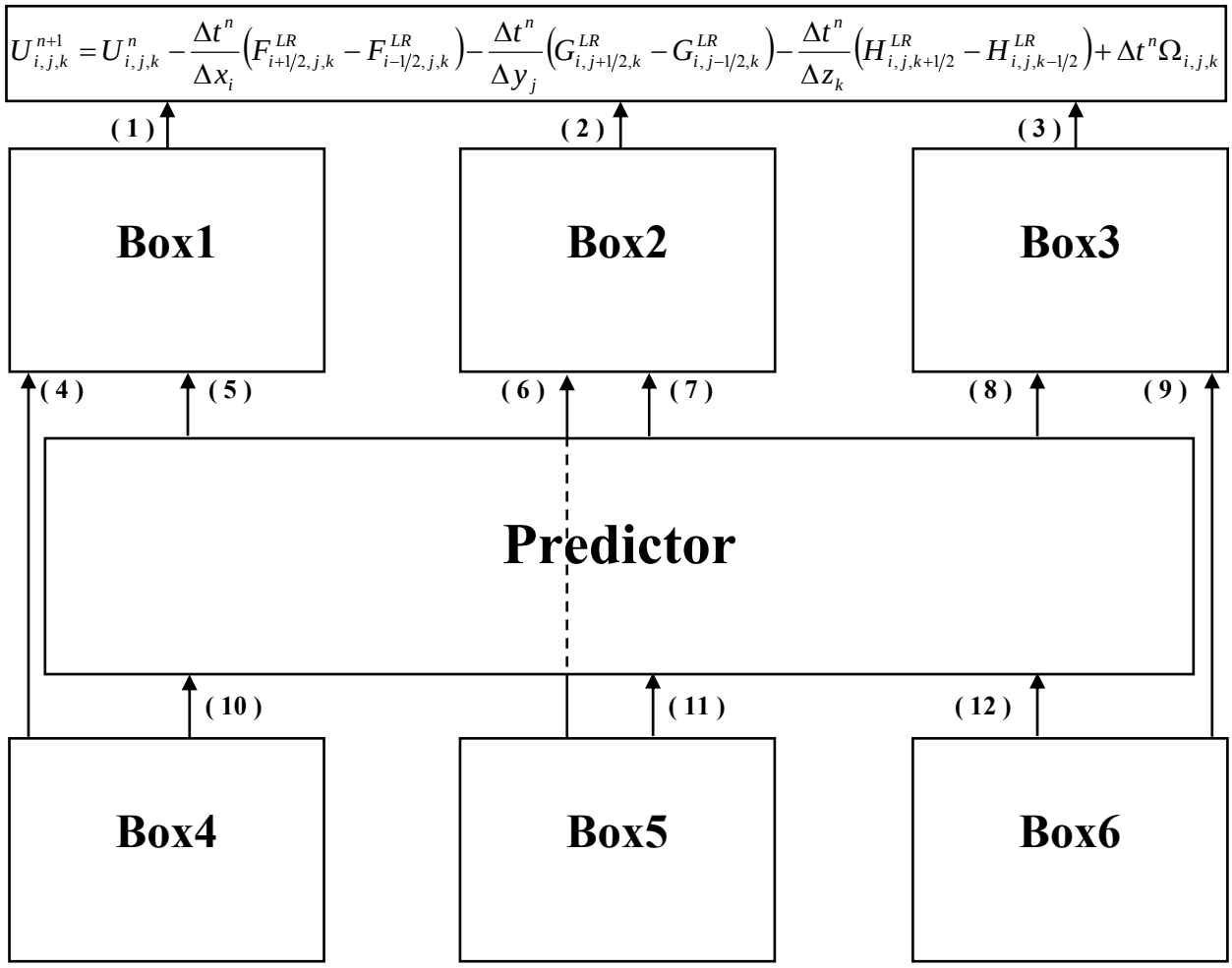

Box1

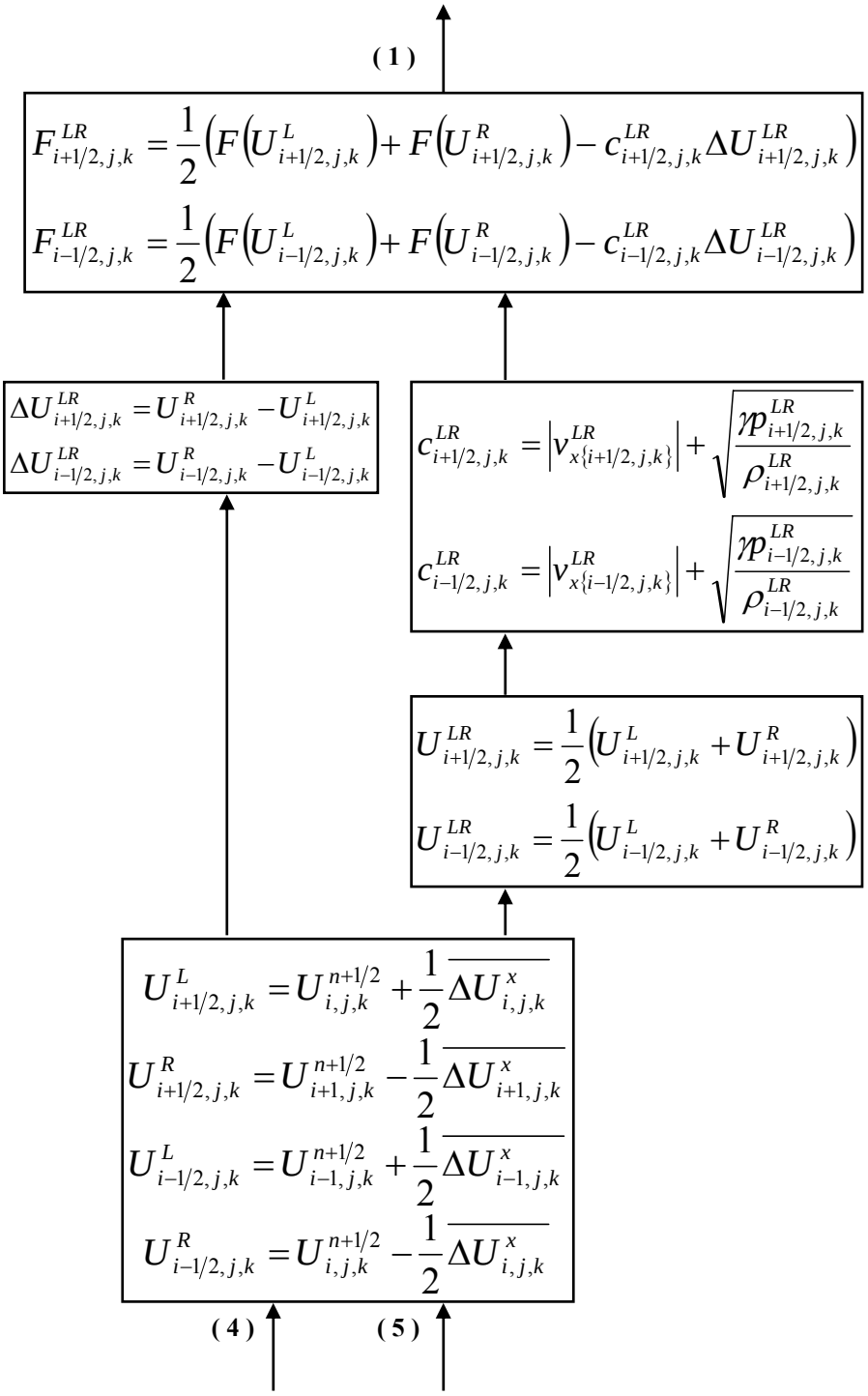
(1)
$F^{LR}_{i+1/2,j,k} = \frac{1}{2}\left(F\left(U^{L}_{i+1/2,j,k}\right) + F\left(U^{R}_{i+1/2,j,k}\right) - c^{LR}_{i+1/2,j,k}\Delta U^{LR}_{i+1/2,j,k}\right)$
$F^{LR}_{i-1/2,j,k} = \frac{1}{2}\left(F\left(U^{L}_{i-1/2,j,k}\right) + F\left(U^{R}_{i-1/2,j,k}\right) - c^{LR}_{i-1/2,j,k}\Delta U^{LR}_{i-1/2,j,k}\right)$
$\Delta U^{LR}_{i+1/2,j,k} = U^{R}_{i+1/2,j,k} - U^{L}_{i+1/2,j,k}$
$\Delta U^{LR}_{i-1/2,j,k} = U^{R}_{i-1/2,j,k} - U^{L}_{i-1/2,j,k}$
$c^{LR}_{i+1/2,j,k} = \left|v^{LR}_{x\{i+1/2,j,k\}}\right| + \sqrt{\frac{\gamma p^{LR}_{i+1/2,j,k}}{\rho^{LR}_{i+1/2,j,k}}}$
$c^{LR}_{i-1/2,j,k} = \left|v^{LR}_{x\{i-1/2,j,k\}}\right| + \sqrt{\frac{\gamma p^{LR}_{i-1/2,j,k}}{\rho^{LR}_{i-1/2,j,k}}}$
$U^{LR}_{i+1/2,j,k} = \frac{1}{2}\left(U^{L}_{i+1/2,j,k} + U^{R}_{i+1/2,j,k}\right)$
$U^{LR}_{i-1/2,j,k} = \frac{1}{2}\left(U^{L}_{i-1/2,j,k} + U^{R}_{i-1/2,j,k}\right)$
$U^{L}_{i+1/2,j,k} = U^{n+1/2}_{i,j,k} + \frac{1}{2}\overline{\Delta U^{x}_{i,j,k}}$
$U^{R}_{i+1/2,j,k} = U^{n+1/2}_{i+1,j,k} - \frac{1}{2}\overline{\Delta U^{x}_{i+1,j,k}}$
$U^{L}_{i-1/2,j,k} = U^{n+1/2}_{i-1,j,k} + \frac{1}{2}\overline{\Delta U^{x}_{i-1,j,k}}$
$U^{R}_{i-1/2,j,k} = U^{n+1/2}_{i,j,k} - \frac{1}{2}\overline{\Delta U^{x}_{i,j,k}}$
(4)
(5)

Box2

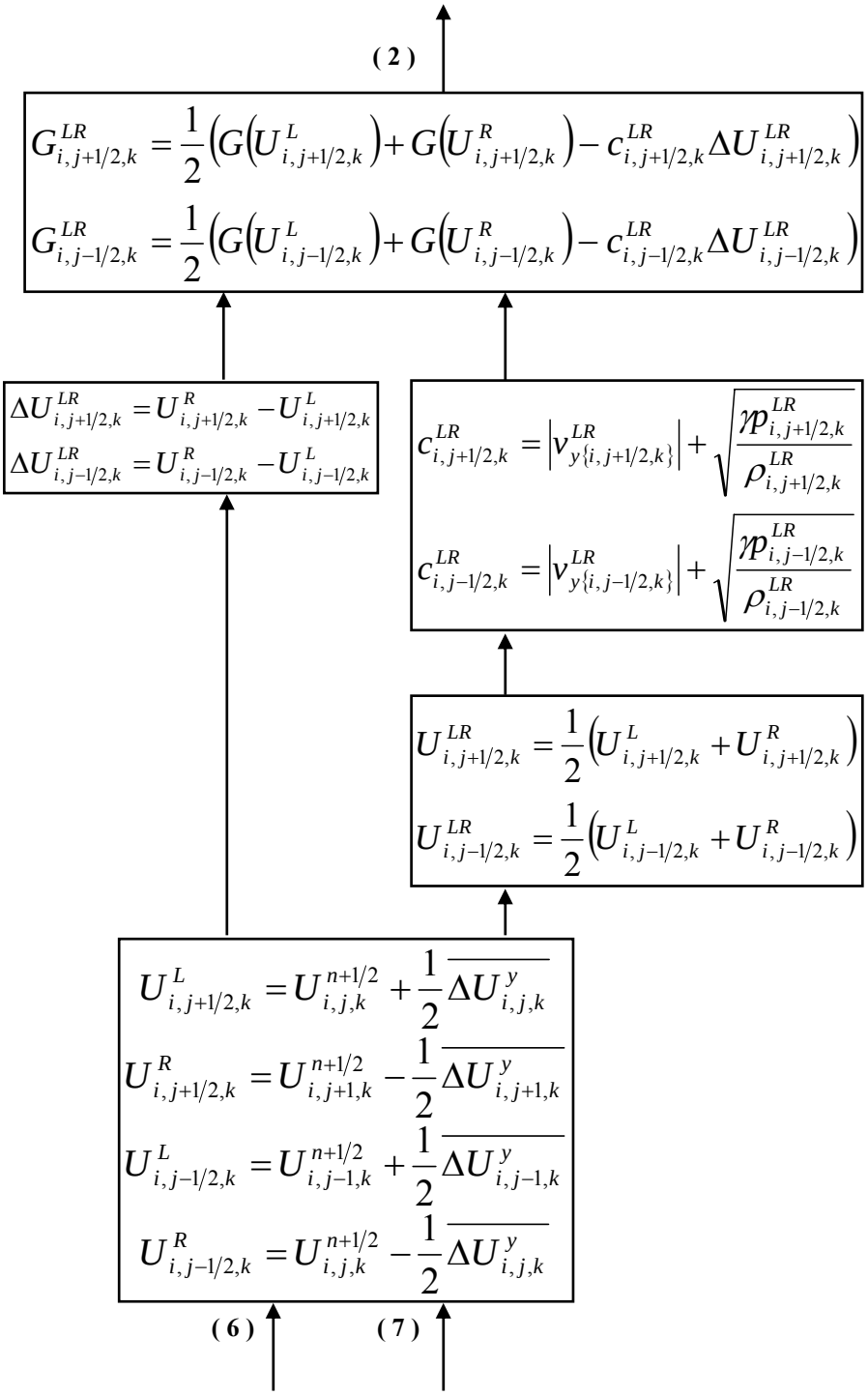
(2)
$G^{LR}_{i,j+1/2,k} = \frac{1}{2}\left(G\left(U^{L}_{i,j+1/2,k}\right) + G\left(U^{R}_{i,j+1/2,k}\right) - c^{LR}_{i,j+1/2,k}\Delta U^{LR}_{i,j+1/2,k}\right)$
$G^{LR}_{i,j-1/2,k} = \frac{1}{2}\left(G\left(U^{L}_{i,j-1/2,k}\right) + G\left(U^{R}_{i,j-1/2,k}\right) - c^{LR}_{i,j-1/2,k}\Delta U^{LR}_{i,j-1/2,k}\right)$
$\Delta U^{LR}_{i,j+1/2,k} = U^{R}_{i,j+1/2,k} - U^{L}_{i,j+1/2,k}$
$\Delta U^{LR}_{i,j-1/2,k} = U^{R}_{i,j-1/2,k} - U^{L}_{i,j-1/2,k}$
$c^{LR}_{i,j+1/2,k} = \left|v^{LR}_{y\{i,j+1/2,k\}}\right| + \sqrt{\frac{\gamma p^{LR}_{i,j+1/2,k}}{\rho^{LR}_{i,j+1/2,k}}}$
$c^{LR}_{i,j-1/2,k} = \left|v^{LR}_{y\{i,j-1/2,k\}}\right| + \sqrt{\frac{\gamma p^{LR}_{i,j-1/2,k}}{\rho^{LR}_{i,j-1/2,k}}}$
$U^{LR}_{i,j+1/2,k} = \frac{1}{2}\left(U^{L}_{i,j+1/2,k} + U^{R}_{i,j+1/2,k}\right)$
$U^{LR}_{i,j-1/2,k} = \frac{1}{2}\left(U^{L}_{i,j-1/2,k} + U^{R}_{i,j-1/2,k}\right)$
$U^{L}_{i,j+1/2,k} = U^{n+1/2}_{i,j,k} + \frac{1}{2}\overline{\Delta U^{y}_{i,j,k}}$
$U^{R}_{i,j+1/2,k} = U^{n+1/2}_{i,j+1,k} - \frac{1}{2}\overline{\Delta U^{y}_{i,j+1,k}}$
$U^{L}_{i,j-1/2,k} = U^{n+1/2}_{i,j-1,k} + \frac{1}{2}\overline{\Delta U^{y}_{i,j-1,k}}$
$U^{R}_{i,j-1/2,k} = U^{n+1/2}_{i,j,k} - \frac{1}{2}\overline{\Delta U^{y}_{i,j,k}}$
(6)
(7)

Box3

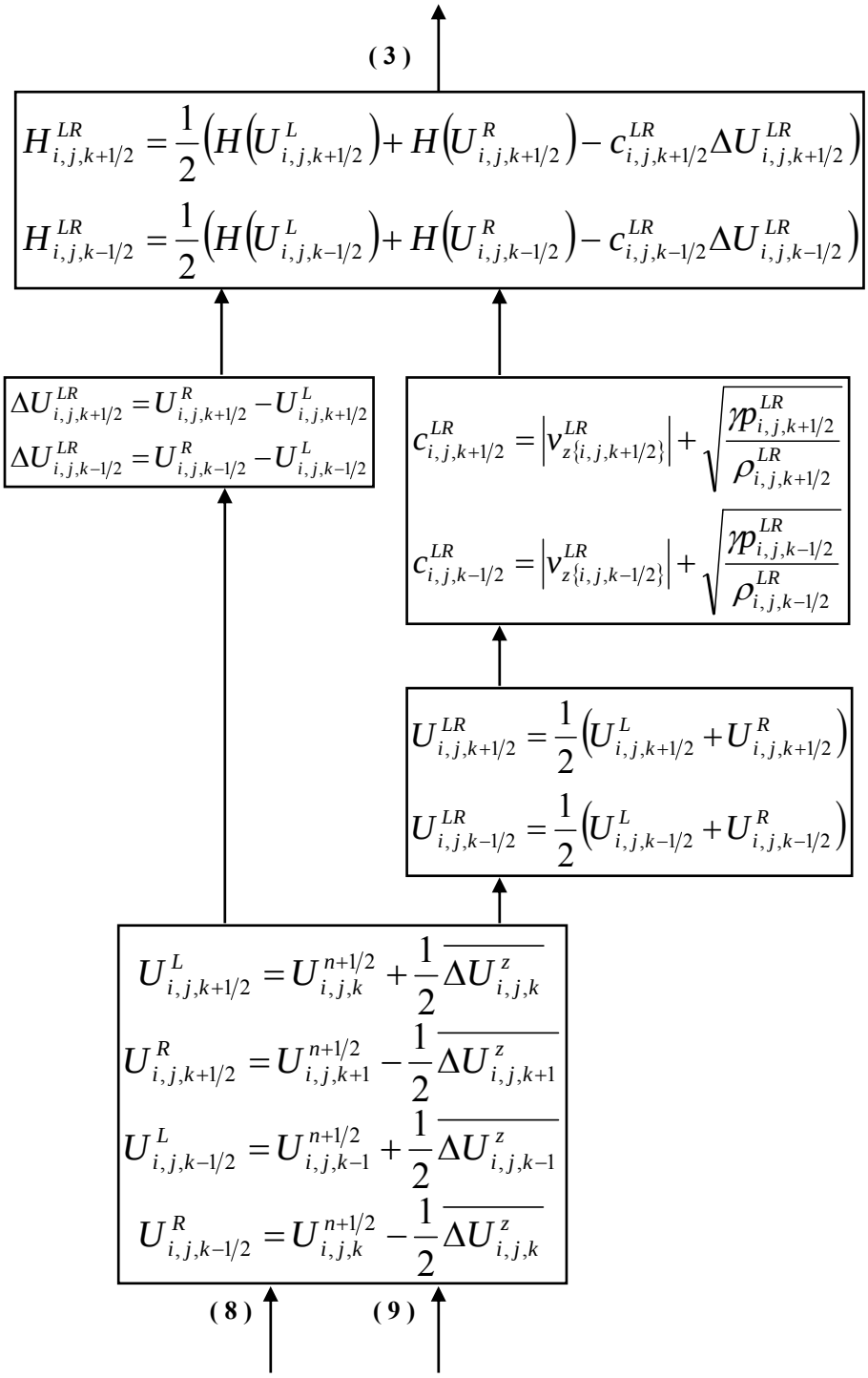
(3)
$H^{LR}_{i,j,k+1/2} = \frac{1}{2}\left(H\left(U^{L}_{i,j,k+1/2}\right) + H\left(U^{R}_{i,j,k+1/2}\right) - c^{LR}_{i,j,k+1/2}\Delta U^{LR}_{i,j,k+1/2}\right)$
$H^{LR}_{i,j,k-1/2} = \frac{1}{2}\left(H\left(U^{L}_{i,j,k-1/2}\right) + H\left(U^{R}_{i,j,k-1/2}\right) - c^{LR}_{i,j,k-1/2}\Delta U^{LR}_{i,j,k-1/2}\right)$
$\Delta U^{LR}_{i,j,k+1/2} = U^{R}_{i,j,k+1/2} - U^{L}_{i,j,k+1/2}$
$\Delta U^{LR}_{i,j,k-1/2} = U^{R}_{i,j,k-1/2} - U^{L}_{i,j,k-1/2}$
$c^{LR}_{i,j,k+1/2} = \left|v^{LR}_{z\{i,j,k+1/2\}}\right| + \sqrt{\frac{\gamma p^{LR}_{i,j,k+1/2}}{\rho^{LR}_{i,j,k+1/2}}}$
$c^{LR}_{i,j,k-1/2} = \left|v^{LR}_{z\{i,j,k-1/2\}}\right| + \sqrt{\frac{\gamma p^{LR}_{i,j,k-1/2}}{\rho^{LR}_{i,j,k-1/2}}}$
$U^{LR}_{i,j,k+1/2} = \frac{1}{2}\left(U^{L}_{i,j,k+1/2} + U^{R}_{i,j,k+1/2}\right)$
$U^{LR}_{i,j,k-1/2} = \frac{1}{2}\left(U^{L}_{i,j,k-1/2} + U^{R}_{i,j,k-1/2}\right)$
$U^{L}_{i,j,k+1/2} = U^{n+1/2}_{i,j,k} + \frac{1}{2}\overline{\Delta U^{z}_{i,j,k}}$
$U^{R}_{i,j,k+1/2} = U^{n+1/2}_{i,j,k+1} - \frac{1}{2}\overline{\Delta U^{z}_{i,j,k+1}}$
$U^{L}_{i,j,k-1/2} = U^{n+1/2}_{i,j,k-1} + \frac{1}{2}\overline{\Delta U^{z}_{i,j,k-1}}$
$U^{R}_{i,j,k-1/2} = U^{n+1/2}_{i,j,k} - \frac{1}{2}\overline{\Delta U^{z}_{i,j,k}}$
(8)
(9)

Predictor

(5) (7) (8)

$$U_{i,j,k}^{n+1/2} = U_{i,j,k}^{n} - \frac{\Delta t^n}{2\Delta x_i}\left[F\left(U_{i+1/2,j,k}^{nL}\right) - F\left(U_{i-1/2,j,k}^{nR}\right)\right] - \frac{\Delta t^n}{2\Delta y_j}\left[G\left(U_{i,j+1/2,k}^{nL}\right) - G\left(U_{i,j-1/2,k}^{nR}\right)\right] -$$

$$- \frac{\Delta t^n}{2\Delta z_k}\left[H\left(U_{i,j,k+1/2}^{nL}\right) - H\left(U_{i,j,k-1/2}^{nR}\right)\right] + \frac{\Delta t^n}{2}\Omega_{i,j,k}$$

$$U_{i-1,j,k}^{n+1/2} = U_{i-1,j,k}^{n} - \frac{\Delta t^n}{2\Delta x_{i-1}}\left[F\left(U_{i-1/2,j,k}^{nL}\right) - F\left(U_{i-3/2,j,k}^{n}\right)\right] - \frac{\Delta t^n}{2\Delta y_j}\left[G\left(U_{i-1,j+1/2,k}^{n}\right) - G\left(U_{i-1,j-1/2,k}^{n}\right)\right] -$$

$$- \frac{\Delta t^n}{2\Delta z_k}\left[H\left(U_{i-1,j,k+1/2}^{n}\right) - H\left(U_{i-1,j,k-1/2}^{n}\right)\right] + \frac{\Delta t^n}{2}\Omega_{i-1,j,k}$$

$$U_{i+1,j,k}^{n+1/2} = U_{i+1,j,k}^{n} - \frac{\Delta t^n}{2\Delta x_{i+1}}\left[F\left(U_{i+3/2,j,k}^{n}\right) - F\left(U_{i+1/2,j,k}^{nR}\right)\right] - \frac{\Delta t^n}{2\Delta y_j}\left[G\left(U_{i+1,j+1/2,k}^{n}\right) - G\left(U_{i+1,j-1/2,k}^{n}\right)\right] -$$

$$- \frac{\Delta t^n}{2\Delta z_k}\left[H\left(U_{i+1,j,k+1/2}^{n}\right) - H\left(U_{i+1,j,k-1/2}^{n}\right)\right] + \frac{\Delta t^n}{2}\Omega_{i+1,j,k}$$

$$U_{i,j-1,k}^{n+1/2} = U_{i,j-1,k}^{n} - \frac{\Delta t^n}{2\Delta x_i}\left[F\left(U_{i+1/2,j-1,k}^{n}\right) - F\left(U_{i-1/2,j-1,k}^{n}\right)\right] - \frac{\Delta t^n}{2\Delta y_{j-1}}\left[G\left(U_{i,j-1/2,k}^{nL}\right) - G\left(U_{i,j-3/2,k}^{n}\right)\right] -$$

$$- \frac{\Delta t^n}{2\Delta z_k}\left[H\left(U_{i,j-1,k+1/2}^{n}\right) - H\left(U_{i,j-1,k-1/2}^{n}\right)\right] + \frac{\Delta t^n}{2}\Omega_{i,j-1,k}$$

$$U_{i,j+1,k}^{n+1/2} = U_{i,j+1,k}^{n} - \frac{\Delta t^n}{2\Delta x_i}\left[F\left(U_{i+1/2,j+1,k}^{n}\right) - F\left(U_{i-1/2,j+1,k}^{n}\right)\right] - \frac{\Delta t^n}{2\Delta y_{j+1}}\left[G\left(U_{i,j+3/2,k}^{n}\right) - G\left(U_{i,j+1/2,k}^{nR}\right)\right] -$$

$$- \frac{\Delta t^n}{2\Delta z_k}\left[H\left(U_{i,j+1,k+1/2}^{n}\right) - H\left(U_{i,j+1,k-1/2}^{n}\right)\right] + \frac{\Delta t^n}{2}\Omega_{i,j+1,k}$$

$$U_{i,j,k-1}^{n+1/2} = U_{i,j,k-1}^{n} - \frac{\Delta t^n}{2\Delta x_i}\left[F\left(U_{i+1/2,j,k-1}^{n}\right) - F\left(U_{i-1/2,j,k-1}^{n}\right)\right] - \frac{\Delta t^n}{2\Delta y_j}\left[G\left(U_{i,j+1/2,k-1}^{n}\right) - G\left(U_{i,j-1/2,k-1}^{n}\right)\right] -$$

$$- \frac{\Delta t^n}{2\Delta z_{k-1}}\left[H\left(U_{i,j,k-1/2}^{nL}\right) - H\left(U_{i,j,k-3/2}^{n}\right)\right] + \frac{\Delta t^n}{2}\Omega_{i,j,k-1}$$

$$U_{i,j,k+1}^{n+1/2} = U_{i,j,k+1}^{n} - \frac{\Delta t^n}{2\Delta x_i}\left[F\left(U_{i+1/2,j,k+1}^{n}\right) - F\left(U_{i-1/2,j,k+1}^{n}\right)\right] - \frac{\Delta t^n}{2\Delta y_j}\left[G\left(U_{i,j+1/2,k+1}^{n}\right) - G\left(U_{i,j-1/2,k+1}^{n}\right)\right] -$$

$$- \frac{\Delta t^n}{2\Delta z_{k+1}}\left[H\left(U_{i,j,k+3/2}^{n}\right) - H\left(U_{i,j,k+1/2}^{nR}\right)\right] + \frac{\Delta t^n}{2}\Omega_{i,j,k+1}$$

(10) (11) (12)

Box4

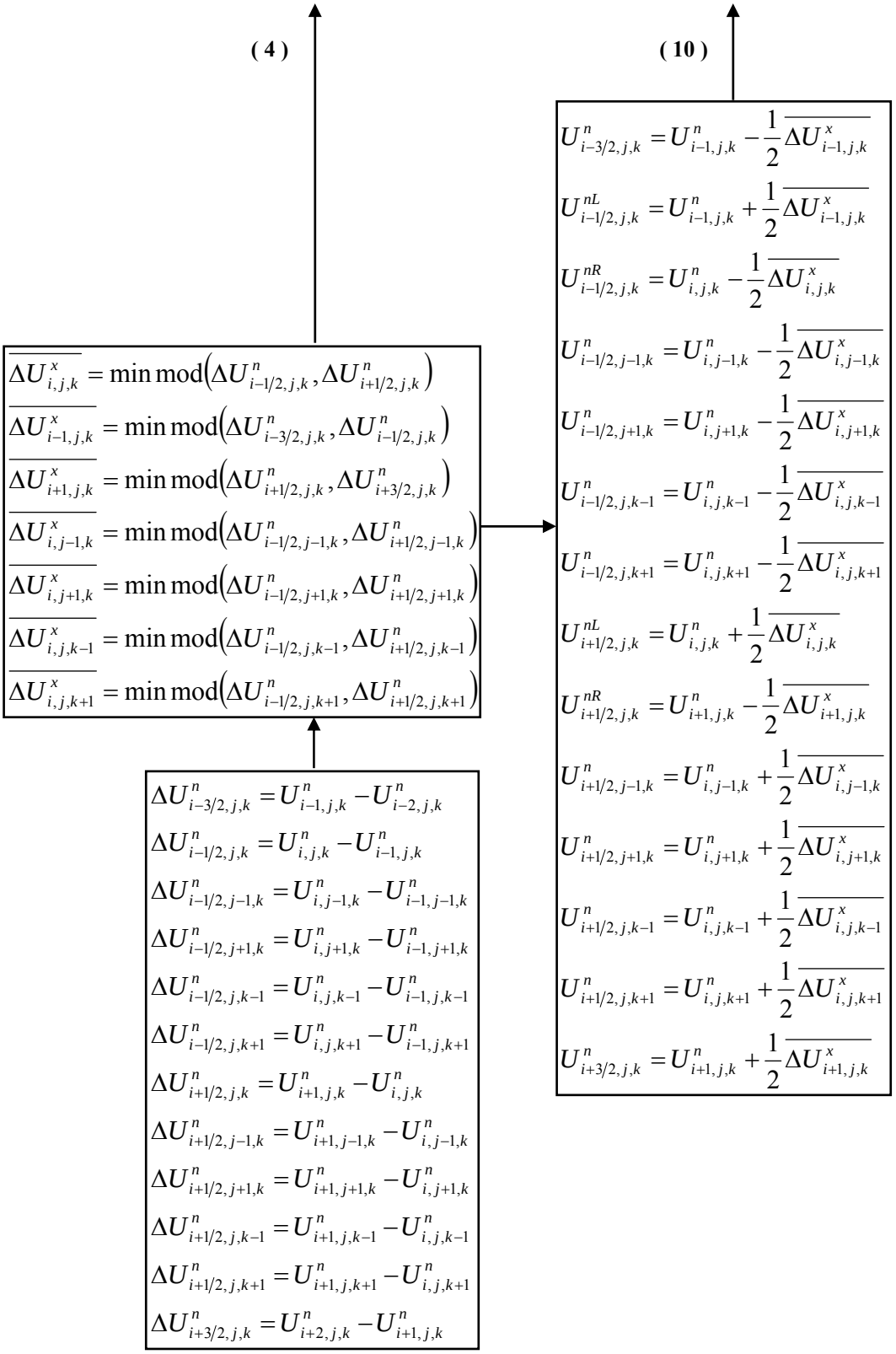
(4)
(10)
$\Delta U^{n}_{i-3/2,j,k} = U^{n}_{i-1,j,k} - U^{n}_{i-2,j,k}$
$\Delta U^{n}_{i-1/2,j,k} = U^{n}_{i,j,k} - U^{n}_{i-1,j,k}$
$\Delta U^{n}_{i-1/2,j-1,k} = U^{n}_{i,j-1,k} - U^{n}_{i-1,j-1,k}$
$\Delta U^{n}_{i-1/2,j+1,k} = U^{n}_{i,j+1,k} - U^{n}_{i-1,j+1,k}$
$\Delta U^{n}_{i-1/2,j,k-1} = U^{n}_{i,j,k-1} - U^{n}_{i-1,j,k-1}$
$\Delta U^{n}_{i-1/2,j,k+1} = U^{n}_{i,j,k+1} - U^{n}_{i-1,j,k+1}$
$\Delta U^{n}_{i+1/2,j,k} = U^{n}_{i+1,j,k} - U^{n}_{i,j,k}$
$\Delta U^{n}_{i+1/2,j-1,k} = U^{n}_{i+1,j-1,k} - U^{n}_{i,j-1,k}$
$\Delta U^{n}_{i+1/2,j+1,k} = U^{n}_{i+1,j+1,k} - U^{n}_{i,j+1,k}$
$\Delta U^{n}_{i+1/2,j,k-1} = U^{n}_{i+1,j,k-1} - U^{n}_{i,j,k-1}$
$\Delta U^{n}_{i+1/2,j,k+1} = U^{n}_{i+1,j,k+1} - U^{n}_{i,j,k+1}$
$\Delta U^{n}_{i+3/2,j,k} = U^{n}_{i+2,j,k} - U^{n}_{i+1,j,k}$
$\overline{\Delta U^{x}_{i,j,k}} = \min\mathrm{mod}\left(\Delta U^{n}_{i-1/2,j,k}, \Delta U^{n}_{i+1/2,j,k}\right)$
$\overline{\Delta U^{x}_{i-1,j,k}} = \min\mathrm{mod}\left(\Delta U^{n}_{i-3/2,j,k}, \Delta U^{n}_{i-1/2,j,k}\right)$
$\overline{\Delta U^{x}_{i+1,j,k}} = \min\mathrm{mod}\left(\Delta U^{n}_{i+1/2,j,k}, \Delta U^{n}_{i+3/2,j,k}\right)$
$\overline{\Delta U^{x}_{i,j-1,k}} = \min\mathrm{mod}\left(\Delta U^{n}_{i-1/2,j-1,k}, \Delta U^{n}_{i+1/2,j-1,k}\right)$
$\overline{\Delta U^{x}_{i,j+1,k}} = \min\mathrm{mod}\left(\Delta U^{n}_{i-1/2,j+1,k}, \Delta U^{n}_{i+1/2,j+1,k}\right)$
$\overline{\Delta U^{x}_{i,j,k-1}} = \min\mathrm{mod}\left(\Delta U^{n}_{i-1/2,j,k-1}, \Delta U^{n}_{i+1/2,j,k-1}\right)$
$\overline{\Delta U^{x}_{i,j,k+1}} = \min\mathrm{mod}\left(\Delta U^{n}_{i-1/2,j,k+1}, \Delta U^{n}_{i+1/2,j,k+1}\right)$
$U^{n}_{i-3/2,j,k} = U^{n}_{i-1,j,k} - \frac{1}{2}\overline{\Delta U^{x}_{i-1,j,k}}$
$U^{nL}_{i-1/2,j,k} = U^{n}_{i-1,j,k} + \frac{1}{2}\overline{\Delta U^{x}_{i-1,j,k}}$
$U^{nR}_{i-1/2,j,k} = U^{n}_{i,j,k} - \frac{1}{2}\overline{\Delta U^{x}_{i,j,k}}$
$U^{n}_{i-1/2,j-1,k} = U^{n}_{i,j-1,k} - \frac{1}{2}\overline{\Delta U^{x}_{i,j-1,k}}$
$U^{n}_{i-1/2,j+1,k} = U^{n}_{i,j+1,k} - \frac{1}{2}\overline{\Delta U^{x}_{i,j+1,k}}$
$U^{n}_{i-1/2,j,k-1} = U^{n}_{i,j,k-1} - \frac{1}{2}\overline{\Delta U^{x}_{i,j,k-1}}$
$U^{n}_{i-1/2,j,k+1} = U^{n}_{i,j,k+1} - \frac{1}{2}\overline{\Delta U^{x}_{i,j,k+1}}$
$U^{nL}_{i+1/2,j,k} = U^{n}_{i,j,k} + \frac{1}{2}\overline{\Delta U^{x}_{i,j,k}}$
$U^{nR}_{i+1/2,j,k} = U^{n}_{i+1,j,k} - \frac{1}{2}\overline{\Delta U^{x}_{i+1,j,k}}$
$U^{n}_{i+1/2,j-1,k} = U^{n}_{i,j-1,k} + \frac{1}{2}\overline{\Delta U^{x}_{i,j-1,k}}$
$U^{n}_{i+1/2,j+1,k} = U^{n}_{i,j+1,k} + \frac{1}{2}\overline{\Delta U^{x}_{i,j+1,k}}$
$U^{n}_{i+1/2,j,k-1} = U^{n}_{i,j,k-1} + \frac{1}{2}\overline{\Delta U^{x}_{i,j,k-1}}$
$U^{n}_{i+1/2,j,k+1} = U^{n}_{i,j,k+1} + \frac{1}{2}\overline{\Delta U^{x}_{i,j,k+1}}$
$U^{n}_{i+3/2,j,k} = U^{n}_{i+1,j,k} + \frac{1}{2}\overline{\Delta U^{x}_{i+1,j,k}}$

Box5

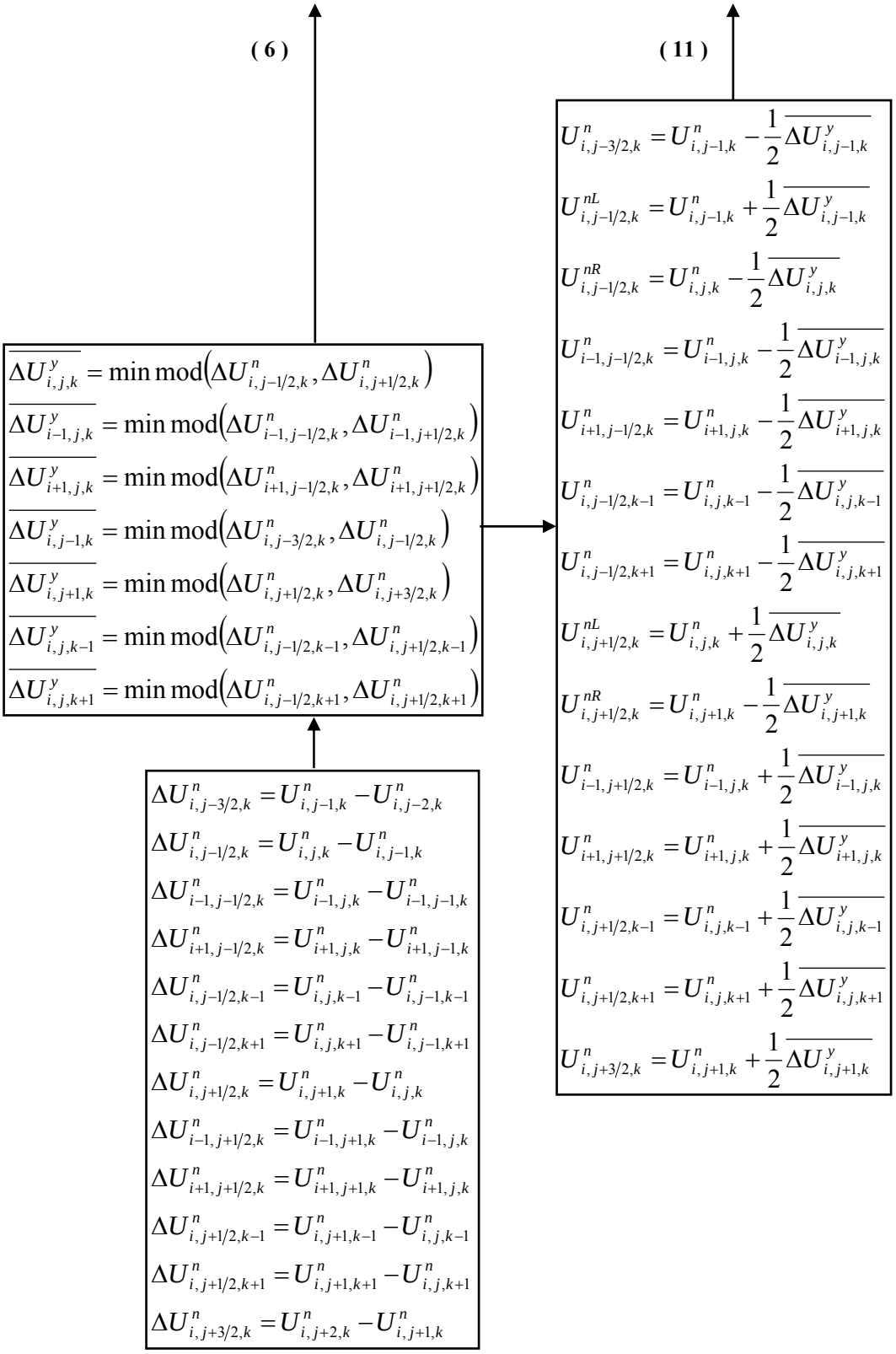
(6)
(11)
$\Delta U^{n}_{i,j-3/2,k} = U^{n}_{i,j-1,k} - U^{n}_{i,j-2,k}$
$\Delta U^{n}_{i,j-1/2,k} = U^{n}_{i,j,k} - U^{n}_{i,j-1,k}$
$\Delta U^{n}_{i-1,j-1/2,k} = U^{n}_{i-1,j,k} - U^{n}_{i-1,j-1,k}$
$\Delta U^{n}_{i+1,j-1/2,k} = U^{n}_{i+1,j,k} - U^{n}_{i+1,j-1,k}$
$\Delta U^{n}_{i,j-1/2,k-1} = U^{n}_{i,j,k-1} - U^{n}_{i,j-1,k-1}$
$\Delta U^{n}_{i,j-1/2,k+1} = U^{n}_{i,j,k+1} - U^{n}_{i,j-1,k+1}$
$\Delta U^{n}_{i,j+1/2,k} = U^{n}_{i,j+1,k} - U^{n}_{i,j,k}$
$\Delta U^{n}_{i-1,j+1/2,k} = U^{n}_{i-1,j+1,k} - U^{n}_{i-1,j,k}$
$\Delta U^{n}_{i+1,j+1/2,k} = U^{n}_{i+1,j+1,k} - U^{n}_{i+1,j,k}$
$\Delta U^{n}_{i,j+1/2,k-1} = U^{n}_{i,j+1,k-1} - U^{n}_{i,j,k-1}$
$\Delta U^{n}_{i,j+1/2,k+1} = U^{n}_{i,j+1,k+1} - U^{n}_{i,j,k+1}$
$\Delta U^{n}_{i,j+3/2,k} = U^{n}_{i,j+2,k} - U^{n}_{i,j+1,k}$
$\overline{\Delta U^{y}_{i,j,k}} = \min\mathrm{mod}\left(\Delta U^{n}_{i,j-1/2,k}, \Delta U^{n}_{i,j+1/2,k}\right)$
$\overline{\Delta U^{y}_{i-1,j,k}} = \min\mathrm{mod}\left(\Delta U^{n}_{i-1,j-1/2,k}, \Delta U^{n}_{i-1,j+1/2,k}\right)$
$\overline{\Delta U^{y}_{i+1,j,k}} = \min\mathrm{mod}\left(\Delta U^{n}_{i+1,j-1/2,k}, \Delta U^{n}_{i+1,j+1/2,k}\right)$
$\overline{\Delta U^{y}_{i,j-1,k}} = \min\mathrm{mod}\left(\Delta U^{n}_{i,j-3/2,k}, \Delta U^{n}_{i,j-1/2,k}\right)$
$\overline{\Delta U^{y}_{i,j+1,k}} = \min\mathrm{mod}\left(\Delta U^{n}_{i,j+1/2,k}, \Delta U^{n}_{i,j+3/2,k}\right)$
$\overline{\Delta U^{y}_{i,j,k-1}} = \min\mathrm{mod}\left(\Delta U^{n}_{i,j-1/2,k-1}, \Delta U^{n}_{i,j+1/2,k-1}\right)$
$\overline{\Delta U^{y}_{i,j,k+1}} = \min\mathrm{mod}\left(\Delta U^{n}_{i,j-1/2,k+1}, \Delta U^{n}_{i,j+1/2,k+1}\right)$
$U^{n}_{i,j-3/2,k} = U^{n}_{i,j-1,k} - \frac{1}{2}\overline{\Delta U^{y}_{i,j-1,k}}$
$U^{nL}_{i,j-1/2,k} = U^{n}_{i,j-1,k} + \frac{1}{2}\overline{\Delta U^{y}_{i,j-1,k}}$
$U^{nR}_{i,j-1/2,k} = U^{n}_{i,j,k} - \frac{1}{2}\overline{\Delta U^{y}_{i,j,k}}$
$U^{n}_{i-1,j-1/2,k} = U^{n}_{i-1,j,k} - \frac{1}{2}\overline{\Delta U^{y}_{i-1,j,k}}$
$U^{n}_{i+1,j-1/2,k} = U^{n}_{i+1,j,k} - \frac{1}{2}\overline{\Delta U^{y}_{i+1,j,k}}$
$U^{n}_{i,j-1/2,k-1} = U^{n}_{i,j,k-1} - \frac{1}{2}\overline{\Delta U^{y}_{i,j,k-1}}$
$U^{n}_{i,j-1/2,k+1} = U^{n}_{i,j,k+1} - \frac{1}{2}\overline{\Delta U^{y}_{i,j,k+1}}$
$U^{nL}_{i,j+1/2,k} = U^{n}_{i,j,k} + \frac{1}{2}\overline{\Delta U^{y}_{i,j,k}}$
$U^{nR}_{i,j+1/2,k} = U^{n}_{i,j+1,k} - \frac{1}{2}\overline{\Delta U^{y}_{i,j+1,k}}$
$U^{n}_{i-1,j+1/2,k} = U^{n}_{i-1,j,k} + \frac{1}{2}\overline{\Delta U^{y}_{i-1,j,k}}$
$U^{n}_{i+1,j+1/2,k} = U^{n}_{i+1,j,k} + \frac{1}{2}\overline{\Delta U^{y}_{i+1,j,k}}$
$U^{n}_{i,j+1/2,k-1} = U^{n}_{i,j,k-1} + \frac{1}{2}\overline{\Delta U^{y}_{i,j,k-1}}$
$U^{n}_{i,j+1/2,k+1} = U^{n}_{i,j,k+1} + \frac{1}{2}\overline{\Delta U^{y}_{i,j,k+1}}$
$U^{n}_{i,j+3/2,k} = U^{n}_{i,j+1,k} + \frac{1}{2}\overline{\Delta U^{y}_{i,j+1,k}}$

Box6

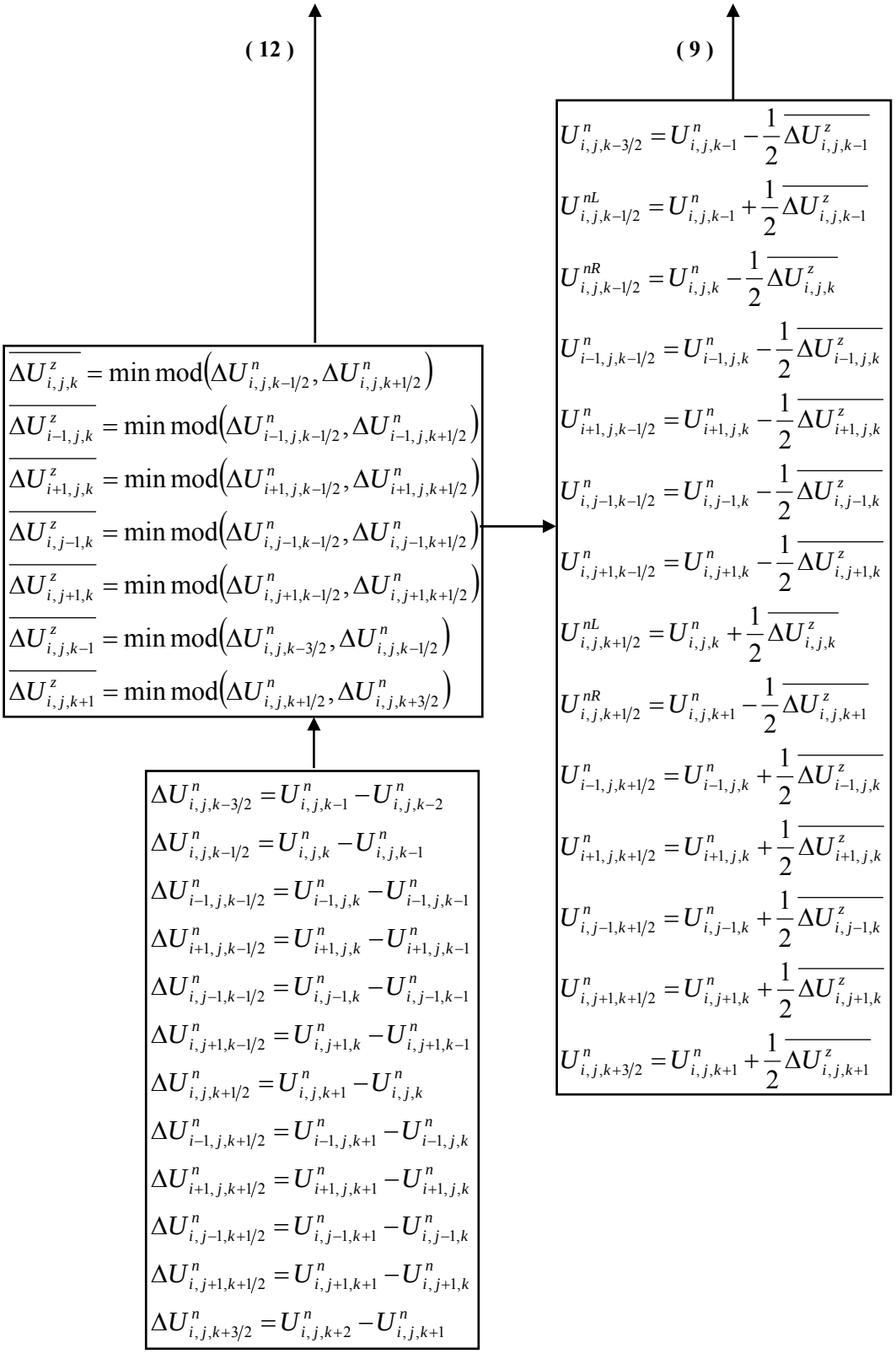
(12)
(9)
$\overline{\Delta U^z_{i,j,k}} = \min\mathrm{mod}\left(\Delta U^n_{i,j,k-1/2}, \Delta U^n_{i,j,k+1/2}\right)$
$\overline{\Delta U^z_{i-1,j,k}} = \min\mathrm{mod}\left(\Delta U^n_{i-1,j,k-1/2}, \Delta U^n_{i-1,j,k+1/2}\right)$
$\overline{\Delta U^z_{i+1,j,k}} = \min\mathrm{mod}\left(\Delta U^n_{i+1,j,k-1/2}, \Delta U^n_{i+1,j,k+1/2}\right)$
$\overline{\Delta U^z_{i,j-1,k}} = \min\mathrm{mod}\left(\Delta U^n_{i,j-1,k-1/2}, \Delta U^n_{i,j-1,k+1/2}\right)$
$\overline{\Delta U^z_{i,j+1,k}} = \min\mathrm{mod}\left(\Delta U^n_{i,j+1,k-1/2}, \Delta U^n_{i,j+1,k+1/2}\right)$
$\overline{\Delta U^z_{i,j,k-1}} = \min\mathrm{mod}\left(\Delta U^n_{i,j,k-3/2}, \Delta U^n_{i,j,k-1/2}\right)$
$\overline{\Delta U^z_{i,j,k+1}} = \min\mathrm{mod}\left(\Delta U^n_{i,j,k+1/2}, \Delta U^n_{i,j,k+3/2}\right)$
$\Delta U^n_{i,j,k-3/2} = U^n_{i,j,k-1} - U^n_{i,j,k-2}$
$\Delta U^n_{i,j,k-1/2} = U^n_{i,j,k} - U^n_{i,j,k-1}$
$\Delta U^n_{i-1,j,k-1/2} = U^n_{i-1,j,k} - U^n_{i-1,j,k-1}$
$\Delta U^n_{i+1,j,k-1/2} = U^n_{i+1,j,k} - U^n_{i+1,j,k-1}$
$\Delta U^n_{i,j-1,k-1/2} = U^n_{i,j-1,k} - U^n_{i,j-1,k-1}$
$\Delta U^n_{i,j+1,k-1/2} = U^n_{i,j+1,k} - U^n_{i,j+1,k-1}$
$\Delta U^n_{i,j,k+1/2} = U^n_{i,j,k+1} - U^n_{i,j,k}$
$\Delta U^n_{i-1,j,k+1/2} = U^n_{i-1,j,k+1} - U^n_{i-1,j,k}$
$\Delta U^n_{i+1,j,k+1/2} = U^n_{i+1,j,k+1} - U^n_{i+1,j,k}$
$\Delta U^n_{i,j-1,k+1/2} = U^n_{i,j-1,k+1} - U^n_{i,j-1,k}$
$\Delta U^n_{i,j+1,k+1/2} = U^n_{i,j+1,k+1} - U^n_{i,j+1,k}$
$\Delta U^n_{i,j,k+3/2} = U^n_{i,j,k+2} - U^n_{i,j,k+1}$
$U^n_{i,j,k-3/2} = U^n_{i,j,k-1} - \frac{1}{2}\overline{\Delta U^z_{i,j,k-1}}$
$U^{nL}_{i,j,k-1/2} = U^n_{i,j,k-1} + \frac{1}{2}\overline{\Delta U^z_{i,j,k-1}}$
$U^{nR}_{i,j,k-1/2} = U^n_{i,j,k} - \frac{1}{2}\overline{\Delta U^z_{i,j,k}}$
$U^n_{i-1,j,k-1/2} = U^n_{i-1,j,k} - \frac{1}{2}\overline{\Delta U^z_{i-1,j,k}}$
$U^n_{i+1,j,k-1/2} = U^n_{i+1,j,k} - \frac{1}{2}\overline{\Delta U^z_{i+1,j,k}}$
$U^n_{i,j-1,k-1/2} = U^n_{i,j-1,k} - \frac{1}{2}\overline{\Delta U^z_{i,j-1,k}}$
$U^n_{i,j+1,k-1/2} = U^n_{i,j+1,k} - \frac{1}{2}\overline{\Delta U^z_{i,j+1,k}}$
$U^{nL}_{i,j,k+1/2} = U^n_{i,j,k} + \frac{1}{2}\overline{\Delta U^z_{i,j,k}}$
$U^{nR}_{i,j,k+1/2} = U^n_{i,j,k+1} - \frac{1}{2}\overline{\Delta U^z_{i,j,k+1}}$
$U^n_{i-1,j,k+1/2} = U^n_{i-1,j,k} + \frac{1}{2}\overline{\Delta U^z_{i-1,j,k}}$
$U^n_{i+1,j,k+1/2} = U^n_{i+1,j,k} + \frac{1}{2}\overline{\Delta U^z_{i+1,j,k}}$
$U^n_{i,j-1,k+1/2} = U^n_{i,j-1,k} + \frac{1}{2}\overline{\Delta U^z_{i,j-1,k}}$
$U^n_{i,j+1,k+1/2} = U^n_{i,j+1,k} + \frac{1}{2}\overline{\Delta U^z_{i,j+1,k}}$
$U^n_{i,j,k+3/2} = U^n_{i,j,k+1} + \frac{1}{2}\overline{\Delta U^z_{i,j,k+1}}$

Appendix 3

Full MHD equations set for 2D cylindrical symmetry in two temperature approximation

$$\begin{cases} \dfrac{\partial \rho}{\partial t}+\dfrac{1}{r}\dfrac{\partial}{\partial r}\left(r\rho v^r\right)+\dfrac{\partial}{\partial z}\left(\rho v^z\right)=0 \\ \dfrac{\partial \rho v^r}{\partial t}+\dfrac{1}{r}\dfrac{\partial}{\partial r}r\left(\rho v^r v^r\right)+\dfrac{\partial p_{tot}}{\partial r}+\dfrac{\partial}{\partial z}\left(\rho v^r v^z\right)=-\dfrac{B^2}{4\pi r} \\ \dfrac{\partial \rho v^z}{\partial t}+\dfrac{1}{r}\dfrac{\partial}{\partial r}r\left(\rho v^z v^r\right)+\dfrac{\partial}{\partial z}\left(\rho v^z v^z+p_{tot}\right)=0 \\ \dfrac{\partial e_{tot}}{\partial t}+\dfrac{1}{r}\dfrac{\partial}{\partial r}\left\{r\left[v^r\left(e_{tot}+p_{tot}\right)\right]\right\}+\dfrac{\partial}{\partial z}\left[v^z\left(e_{tot}+p_{tot}\right)\right]=Q_{las}+Q_J+Q_{th,e}+Q_{th,i}+Q_{rad} \\ \dfrac{\partial e_i}{\partial t}+\dfrac{1}{r}\dfrac{\partial}{\partial r}\left\{r\left[v^r\left(e_i+p_i\right)\right]\right\}+\dfrac{\partial}{\partial z}\left[v^z\left(e_i+p_i\right)\right]=Q_{ei}+Q_{th,i} \\ \dfrac{\partial B}{\partial t}+\dfrac{\partial}{\partial r}v^r B+\dfrac{\partial}{\partial z}v^z B=Q_{mdif}+Q_{ms} \end{cases} \quad \text{(A3.1)}$$

Here for the plasma is assumed the magnetic permeability μ = 1. Total energy is given by $e_{tot}=e_i+e_e+e_{ioniz}+e_{kin}+e_{mag}$, where e_i is the ions internal energy; e_e is the electrons internal energy; e_{ioniz} is the energy of ionization; $e_{kin}=\dfrac{\rho v^2}{2}$ is the kinetic energy; $e_{mag}=\dfrac{B^2}{8\pi}$ is the magnetic energy; $p_{tot}=p_h+p_{mag}=p_i+p_e+p_{mag}$ is the total pressure; p_h is the hydrodynamic pressure; p_i is the ions pressure; p_e is the electrons pressure; $p_{mag}=\dfrac{B^2}{8\pi}$ is the magnetic pressure; Q_{las} is the laser radiation heating term (see Section 3.4); Q_{rad} is the radiation transport term, discussed in Section 3.3; and $Q_{th,e}$ and $Q_{th,i}$ are the heat conduction terms of electrons and ions correspondingly (Sections 3.1 and 5). Magnetic diffusion term for energy equation is Joule heat is given

$$Q_J=\frac{c^2\eta}{16\pi^2}\left[\frac{1}{r^2}\left(\frac{\partial rB}{\partial r}\right)^2+\left(\frac{\partial B}{\partial z}\right)^2\right]. \quad \text{(A3.2)}$$

Magnetic diffusion term for Faraday equation Q_{mdif} and magnetic source term Q_{ms} is discussed in Section 3.2. Expression for the electron-ion energy interchange Q_{ei} can be found in Section 5 (see equation 5.7).

The full MHD equations set (A3.1) presented in short matrix form for TVD-LF numerical scheme (see Appendix 1) are

$$\frac{\partial \mathbf{U}}{\partial t}+\frac{1}{r}\frac{\partial}{\partial r}\left[r\mathbf{F}(\mathbf{U})\right]+\frac{\partial \mathbf{P}(\mathbf{U})}{\partial r}+\frac{\partial \mathbf{G}(\mathbf{U})}{\partial z}=\mathbf{\Omega}, \tag{A3.3}$$

where

$$\mathbf{U}=\begin{bmatrix}\rho\\ \rho v^r\\ \rho v^z\\ e_{tot}\\ e_i\\ B\end{bmatrix},\ \mathbf{F}(\mathbf{U})=\begin{bmatrix}\rho v^r\\ \rho v^r v^r\\ \rho v^z v^r\\ v^r\left(e_{tot}+p_{tot}\right)\\ v^r\left(e_i+p_i\right)\\ 0\end{bmatrix},\ \mathbf{P}(\mathbf{U})=\begin{bmatrix}0\\ p_{tot}\\ 0\\ 0\\ 0\\ v^r B\end{bmatrix},\ \mathbf{G}(\mathbf{U})=\begin{bmatrix}\rho v^z\\ \rho v^r v^z\\ \rho v^z v^z+p_{tot}\\ v^z\left[e_{tot}+p_{tot}\right]\\ v^z\left[e_i+p_i\right]\\ v^z B\end{bmatrix},$$

$$\mathbf{\Omega}=\begin{bmatrix}0\\ -\dfrac{B^2}{4\pi r}\\ 0\\ Q_{las}+Q_J+Q_{th,e}+Q_{th,i}+Q_{rad}\\ Q_{ei}+Q_{th,i}\\ Q_{mdif}+Q_{ms}\end{bmatrix}. \tag{A3.4}$$

Appendix 4

HD equations set for 2D cylindrical symmetry in two temperature approximation. No magnetic field

$$\begin{cases} \frac{\partial \rho}{\partial t}+\frac{1}{r}\frac{\partial}{\partial r}\left(r\rho v^{r}\right)+\frac{\partial}{\partial z}\left(\rho v^{z}\right)=0 \\ \frac{\partial \rho v^{r}}{\partial t}+\frac{1}{r}\frac{\partial}{\partial r}r\left(\rho v^{r}v^{r}\right)+\frac{\partial p_{tot}}{\partial r}+\frac{\partial}{\partial z}\left(\rho v^{r}v^{z}\right)=0 \\ \frac{\partial \rho v^{z}}{\partial t}+\frac{1}{r}\frac{\partial}{\partial r}r\left(\rho v^{z}v^{r}\right)+\frac{\partial}{\partial z}\left(\rho v^{z}v^{z}+p_{tot}\right)=0 \\ \frac{\partial e_{tot}}{\partial t}+\frac{1}{r}\frac{\partial}{\partial r}\left\{r\left[v^{r}\left(e_{tot}+p_{tot}\right)\right]\right\}+\frac{\partial}{\partial z}\left[v^{z}\left(e_{tot}+p_{tot}\right)\right]=Q_{las}+Q_{th,e}+Q_{th,i}+Q_{rad} \\ \frac{\partial e_{i}}{\partial t}+\frac{1}{r}\frac{\partial}{\partial r}\left\{r\left[v^{r}\left(e_{i}+p_{i}\right)\right]\right\}+\frac{\partial}{\partial z}\left[v^{z}\left(e_{i}+p_{i}\right)\right]=Q_{ei}+Q_{th,i} \end{cases} \qquad \text{(A4.1)}$$

The total energy does not include magnetic field part $e_{tot}=e_i+e_e+e_{ioniz}+e_{kin}$, where e_i is the ions internal energy; e_e is the electrons internal energy; e_{ioniz} is the energy of ionization; $e_{kin}=\frac{\rho v^2}{2}$ is the kinetic energy; $p_{tot}=p_h=p_i+p_e$ is the total pressure; p_h is the hydrodynamic pressure; p_i is the ions pressure; p_e is the electrons pressure; Q_{las} is the laser radiation heating term (see Section 3.4); Q_{rad} is the radiation transport term, discussed in Section 3.3; and $Q_{th,e}$ and $Q_{th,i}$ are the heat conduction terms of electrons and ions correspondingly (Sections 3.1 and 5). Expression for the electron-ion energy interchange Q_{ei} is presented in Section 5 (see equation 5.7).

The full MHD equations set (A4.1) presented in short matrix form for TVD-LF numerical scheme (see Appendix 1) is given

$$\frac{\partial \mathbf{U}}{\partial t}+\frac{1}{r}\frac{\partial}{\partial r}\left[r\mathbf{F}\left(\mathbf{U}\right)\right]+\frac{\partial \mathbf{P}\left(\mathbf{U}\right)}{\partial r}+\frac{\partial \mathbf{G}\left(\mathbf{U}\right)}{\partial z}=\mathbf{\Omega}, \qquad \text{(A4.2)}$$

where

$$\mathbf{U}=\begin{bmatrix}\rho\\ \rho v^{r}\\ \rho v^{z}\\ e_{tot}\\ e_{i}\end{bmatrix},\ \mathbf{F}(\mathbf{U})=\begin{bmatrix}\rho v^{r}\\ \rho v^{r}v^{r}\\ \rho v^{z}v^{r}\\ v^{r}\left(e_{tot}+p_{tot}\right)\\ v^{r}\left(e_{i}+p_{i}\right)\end{bmatrix},\ \mathbf{P}(\mathbf{U})=\begin{bmatrix}0\\ p_{tot}\\ 0\\ 0\\ 0\end{bmatrix},\ \mathbf{G}(\mathbf{U})=\begin{bmatrix}\rho v^{z}\\ \rho v^{r}v^{z}\\ \rho v^{z}v^{z}+p_{tot}\\ v^{z}\left[e_{tot}+p_{tot}\right]\\ v^{z}\left[e_{i}+p_{i}\right]\end{bmatrix},$$

$$\mathbf{\Omega}=\begin{bmatrix}0\\ 0\\ 0\\ Q_{las}+Q_{th,e}+Q_{th,i}+Q_{rad}\\ Q_{ei}+Q_{th,i}\end{bmatrix}. \qquad \text{(A4.3)}$$

Appendix 5

HD equations set for full 3D geometry in two temperature approximation. No magnetic field

$$\begin{cases} \frac{\partial \rho}{\partial t}+\frac{\partial \rho v_x}{\partial x}+\frac{\partial \rho v_y}{\partial y}+\frac{\partial \rho v_z}{\partial z}=0 \\ \frac{\partial \rho v_x}{\partial t}+\frac{\partial}{\partial x}\left(\rho v_x^2+p_{tot}\right)+\frac{\partial \rho v_x v_y}{\partial y}+\frac{\partial \rho v_x v_z}{\partial z}=0 \\ \frac{\partial \rho v_y}{\partial t}+\frac{\partial \rho v_y v_x}{\partial x}+\frac{\partial}{\partial y}\left(\rho v_y^2+p_{tot}\right)+\frac{\partial \rho v_y v_z}{\partial z}=0 \\ \frac{\partial \rho v_z}{\partial t}+\frac{\partial \rho v_z v_x}{\partial x}+\frac{\partial \rho v_z v_y}{\partial y}+\frac{\partial}{\partial z}\left(\rho v_z^2+p_{tot}\right)=0 \\ \frac{\partial e_{tot}}{\partial t}+\frac{\partial}{\partial x}\left(v_x\left[e_{tot}+p_{tot}\right]\right)+\frac{\partial}{\partial y}\left(v_y\left[e_{tot}+p_{tot}\right]\right)+\frac{\partial}{\partial z}\left(v_z\left[e_{tot}+p_{tot}\right]\right)=Q_{las}+Q_{th,e}+Q_{th,i}+Q_{rad} \\ \frac{\partial e_i}{\partial t}+\frac{\partial}{\partial x}\left(v_x\left[e_i+p_i\right]\right)+\frac{\partial}{\partial y}\left(v_y\left[e_i+p_i\right]\right)+\frac{\partial}{\partial z}\left(v_z\left[e_i+p_i\right]\right)=Q_{ei}+Q_{th,i} \end{cases} \quad \text{(A5.1)}$$

The total energy does not include magnetic field part: $e_{tot}=e_i+e_e+e_{ioniz}+e_{kin}$, where e_i is the ions internal energy; e_e is the electrons internal energy; e_{ioniz} is the energy of ionization; $e_{kin}=\frac{\rho v^2}{2}$ is the kinetic energy; $p_{tot}=p_h=p_i+p_e$ is the total pressure; p_h is the hydrodynamic pressure; p_i is the ions pressure; p_e is the electrons pressure; Q_{las} is the laser radiation heating term (see Section 3.4); Q_{rad} is the radiation transport term, discussed in Section 3.3; and $Q_{th,e}$ and $Q_{th,i}$ are the heat conduction terms of electrons and ions correspondingly (Sections 3.1 and 5). Expression for the electron-ion energy interchange Q_{ei} is presented in Section 5 (see equation 5.7).

The full MHD equations set (A5.1) presented in short matrix form for TVD-LF numerical scheme (see Appendix 2) is given

$$\frac{\partial \mathbf{U}}{\partial t}+\frac{\partial \mathbf{F}(\mathbf{U})}{\partial x}+\frac{\partial \mathbf{G}(\mathbf{U})}{\partial y}+\frac{\partial \mathbf{H}(\mathbf{U})}{\partial z}=\mathbf{\Omega}\,, \tag{A4.2}$$

where

$$\mathbf{U}=\begin{bmatrix}\rho\\ \rho v_x\\ \rho v_y\\ \rho v_z\\ e_{tot}\\ e_i\end{bmatrix},\mathbf{F}=\begin{bmatrix}\rho v_x\\ \rho v_x^2+p_{tot}\\ \rho v_x v_y\\ \rho v_x v_z\\ v_x(e_{tot}+p_{tot})\\ v_x(e_i+p_i)\end{bmatrix},\ \mathbf{G}=\begin{bmatrix}\rho v_y\\ \rho v_y v_x\\ \rho v_y^2+p_{tot}\\ \rho v_y v_z\\ v_y(e_{tot}+p_{tot})\\ v_y(e_i+p_i)\end{bmatrix},\ \mathbf{H}=\begin{bmatrix}\rho v_z\\ \rho v_z v_x\\ \rho v_z v_y\\ \rho v_z^2+p_{tot}\\ v_z(e_{tot}+p_{tot})\\ v_z(e_i+p_i)\end{bmatrix},$$

$$\mathbf{\Omega}=\begin{bmatrix}0\\ 0\\ 0\\ 0\\ Q_{las}+Q_{th,e}+Q_{th,i}+Q_{rad}\\ Q_{ei}+Q_{th,i}\end{bmatrix}. \tag{A5.3}$$

REFERENCES

1. G. E. Moore, "Cramming More Components Onto Integrated Circuits," *Electronics*, **38 (**8), 114 (1965).
2. H. J. Levinson, *Principles of Lithography*, SPIE PRESS, Bellinham, Washington (2001).
3. B. Fay, " Advanced optical lithography development, from UV to EUV ," *Microelectron. Eng.*, **61-62**, 11 (2002).
4. P. J. Silverman, "The Intel Lithography Roadmap," *Intel Technology Journal*, **6** (2), 55 (2002).
5. V. Bakshi, "Welcome and Introduction," *International SEMATECH EUV Source Workshop*, Santa Clara, CA, February 22, (2004).
6. A. Hassanein, V. Sizyuk, V. Tolkach, V. Morozov, and B. J .Rice, "HEIGHTS initial simulation of discharge-produced plasma hydrodynamics and radiation transport for EUV lithography," *Proceedings of SPIE, Emerging Lithographic Technologies VII*, **5037** (2), 714 (2003).
7. A. Hassanein, V. Sizyuk, V. Tolkach, V. Morozov, and B. J. Rice, "HEIGHTS initial simulation of discharge produced plasma hydrodynamics and radiation transport for extreme ultraviolet lithography," *Journal of Microlithography, Microfabrication, and Microsystems*, **3** (1), 130 (2004).
8. A. Hassanein, V. Sizyuk, V. Tolkach, V. Morozov, T. Sizyuk, B. J. Rice, and V. Bakshi, "Simulation and optimization of DPP hydrodynamics and radiation transport for EUV lithography devices," *Proceedings of SPIE, Emerging Lithographic Technologies VIII*, **5374** (1), 413 (2004).
9. G. Toth, "The $\nabla \cdot \mathbf{B}$ Constraint in Shock-Capturing Magnetohydrodynamics Codes," *J. Comp. Phys.*, **161**, 605 (2000).
10. P. Yanhunden, "A Positive Conservative Method for Magnetohydrodynamics Based on HLL and Roe Methods," *J. Comp. Phys.*, **160**, 649 (2000).
11. V. Sizyuk, A. Hassanein, V. Morozov, V. Tolkach, T. Sizyuk, and B. Rice, "Numerical simulation of laser-produced plasma devices for EUV lithography using the HEIGHTS integrated model," *Numerical Heat Transfer, Part A*, **49**, 215 (2006).

12. J.H. Heinbockel, *Introduction to Tensor Calculus and Continuum Mechanics*, Trafford Pub., (2001)
13. J. Abram, *Tensor Calculus through Differential Geometry*, London, (1965).
14. J. M. Stone and M. Norman, "ZEUS-2D: A radiation magnetohydrodynamics code for astrophysical flows in two space dimensions. The magnetohydrodynamic algorithms and tests," *The Astrophysical Journal*, **80**, 791 (1992).
15. P. F. Peyrard and P. Villedieu, "A Roe scheme for ideal MHD equations on 2D adaptively refined triangular grids," *J. Comp. Phys.*, **150**, 373 (1999).
16. J. P. Goedbloed, "Introduction to MHD Instabilities," *Fusion Science and Technology*, **45**, 85 (2004)
17. L. F. Wanex, V. I. Sotnikov, and J. N. Leboeuf, "Linear analysis of magnetic and flow shear stabilization of Z-pinch instabilities," *Phys. Plasmas*, **12**, 042101 (2005).
18. A. H. Khater, S. M. Moawad, and D. K. Callebaut, "Linear and nonlinear stability analysis for two-dimensional ideal magnetohydrodynamics with incompressible flows," *Phys. Plasmas*, **12,** 012316 (2005).
19. R. P. Golingo, U. Shumlak, and B. A. Nelson, "Formation of a sheared flow Z pinch," *Phys. Plasmas*, **12,** 062505 (2005).
20. P. G. Eltgroth, "Comparison of plasma focus calculations," *Phys. Fluids*, 25, 2408 (1982).
21. G. Tóth and D. Odstrčil "Comparison of some Flux Corrected Transport and Total Variation Diminishing Numerical Schemes for Hydrodynamic and Magnetohydrodynamic Problems," *J. Comp. Phys.*, **128**, 82 (1996).
22. V. M. Kovenya, S. G. Cherny, and A. S. Lebedev, "Numerical methods for solving the gas dynamics and Navier-Stokes equation on the basic of the splitting up-method," *Comput. Fluid Dynamics*, Ed. G.V. Davis, C. Fletcher.- North-Holland, (1988).
23. R. J. Leveque, *Finite volume methods for hyperbolic problems*, Cambridge University Press, (2002).
24. V. M. Kovenya, S. G. Cherny, and V. I. Pinchukov "Numerical modeling of stationary separation flows," *Proc. of the IV Intern. Conf. on Boundared and Intern. or Layers*, Boole Press, 117 (1986).
25. V. Venkatakrishnan and D. J. Mavriplis, "Implicit solvers for unstructured meshes," *J. Comp. Phys.*, **105**, 83 (1993).

26. P. J. Roach, *Computational fluid dynamics*, Hermosa Publishers, Albuquerque, NM, (1976).
27. O. V. Diyankov, I. V. Glazurin, and S. V. Koshelev, "MAG – two-dimensional resistive MHD code using an arbitrary moving coordinate system," *Comp. Phys. Commun.*, **106**, 76 (1997).
28. P. R. Amestoy et al., "Analysis and comparison of two general sparse solvers for distributed memory computers," *ACM Transactions on Mathematical Software*, **27**(4), 388 (2001).
29. G. Tóth, R. Keppens, and M.A. Botchev, "Implicit and semi-implicit schemes in the Versatile Advection Code: numerical tests," *Astronomy and Astrophysics*, **332**, 1159 (1998).
30. M. M. Widner, "Self-generated magnetic fields in laser plasmas," *Phys.Fluid.*, **16**(10), 1778 (1973).
31. D. G. Colombant and N. K. Winsor, "Thermal-force terms and self-generated magnetic fields in laser-produced plasmas," *Phys. Rev. Let.*, **38**(13), 697 (1977).
32. P. Mora and R. Pellat, "Magnetic field generation in the underdense plasma," *Phys. Fluid.*, **24**(12), 2219 (1981).
33. A. Unsöld, *Physik der Sternatmosphären*, Springer-Verlag, Berlin, (1938). (in Germany)
34. Ya. Zeldovich and Yu. Raizer, *Physics of Shock Waves and High-Temperature Hydrodynamics Phenomena*, Vol. 1, Academic Press, New York and London, (1966).
35. G. Mihailov, *Some problems of Monte Carlo methods theory*, Moscow (1974). (in Russian)
36. R. Siegel and J. Howell, *Thermal Radiation Heat Transfer*, Hemisphere Publishing Corp., Washington, New York, London (1981).
37. G. Korn and T. Korn, *Mathematical handbook*, McGraw-Hill Book Company (1968).
38. M. Richardson et al. "High conversion efficiency mass-limited Sn-based laser plasma source for extreme ultraviolet lithography," *J. Vac. Sci. Technol. B*, **22**(2), 785 (2004).
39. I. Choi et al. "Detailed space-resolved characterization of a laser-plasma soft-x-ray source at 13.5-nm wavelength with tin and its oxides," *J. Opt. Soc. Am. B*, **17**(9), 1616 (2000).
40. G. Schriever, K. Bergman, and R. Lebert, "Narrowband laser produced extreme ultraviolet sources adapted to silicon/molybdenum multilayer optics," *J. Appl. Phys*, **83**(9), 4566 (1998).
41. F. Jin and M. Richardson, "New laser plasma source for extreme-ultraviolet lithography," *Appl. Opt.*, **34**(25), 5750 (1995).
42. G. Ferrante, M. Zarcone, and S. Urypin, "Inverse bremsstrahlung in a plasma with electron temperature anisotropy," *Physics of Plasma*, **8**(11), 4745 (2001).

43. D. Colombant et al. "Laser target model," *Physics of Fluids*, **18**(12), 1687 (1975).
44. M. von Allmen and A. Blatter, *Laser-Beam Interactions with Materials*, Springer Series in Material Science, V.2, 2th Edition, Springer, Berlin, (1995).
45. I. Olhovsky, *Course of engineering mechanics for physicists*, Moscow University, Moscow, (1978). (in Russian)
46. V. M. Ivastchenko and V. V. Mitin, *Simulation of Transport Phenomena in Semiconductors. Method Monte Carlo*, Naukova Dumka, Kiev, (1990). (in Russian)
47. T. W. Johnston, J. M. Dawson, "Correct value for high-frequency power absorption by inverse bremsstrahlung in plasmas," *Phys. Fluid.*, **16**(5), 722 (1973).
48. L. Spitzer, *Physics of fully ionized gases*, 2th edition, Interscience Publishers, New York, (1962).
49. G. Strang, "On the construction and comparison of difference schemes," *SIAM J. Numer. Anal.*, **5**, 506 (1968).
50. L.D. Landau, E.M. Lifshits, *The classical theory of fields*, Butterworth Heinemann, Oxford (England) (1995).
51. D. Düchs and H. R. Griem, "Computer study of the dynamic phase of a small θ-pinch," *Phys. Fluids*, **9**(6), 1099 (1966).
52. A.N. Lubimov and V. V. Rusanov, *Gas Flows around Obtuse Bodies* (Part I, Calculation method and analysis of flows and Part II, Tables of gasdynamics functions), Moscow (1970). (in Russian)
53. M. Van Dyke, *An album of fluid motion*, The Parabolic Press, Stanford, California (1982).
54. A. . Samarskii and Yu.P. Popov, *Difference methods of the gasdynamics problems solution,* Nauka, Moscow (1980). (in Russian)
55. S. Maxon and J. Eddleman, *2D MHD calculations of the plasma focus, Lawrence Livermore Laboratory*, Preprint 79067, 10 (1977).
56. R.C. Spitzer et al, "Conversion efficiencies from laser-produced plasmas in the extreme ultraviolet regime," *J. Appl. Phys.*, **79**(5), 2251 (1996)
57. V. Morozov, V. Tolkach, and A. Hassanein, *Calculation of tin atomic data and plasma properties*, ANL Report ANL-ET-04/24, Argonne National Laboratory, Argonne, IL (2004).

58. V. Morozov, V. Sizyuk, A. Hassanein, and V. Tolkach, *Simulation of discharge produced plasma and EUV radiation in various Z-pinch devices*, ANL Report ANL-ET-04/31, Argonne National Laboratory, Argonne, IL (2004).
59. G. B. Zimmerman and W. L. Kruer, "Numerical simulation of laser-initiated fusion," *Comm. Plasm. Phys. Cont. Fusion*, **2**(2), 51 (1975).
60. T. Aota and T. Tomie, "Ultimate efficiency of extreme ultraviolet radiation from a laser-produced plasma," *Phys. Rev. Lett.*, **94**(1), 015004 (2005).
61. M. Richardson, C.-S. Koay, K. Takenoshita, C. Keyser, and M. Al-Rabban, "High conversion efficiency mass-limited Sn-based plasma source for extreme ultraviolet lithography," *J. Vac. Sci. Technol. B*, **22**(2), 785 (2004).
62. I.W. Choi, H. Daido, S. Yamagami, K. Nagai, T. Norimatsu, H. Takabe, M. Suzuki, T. Nakayama, and T. Matsui, "Detailed space-resolved characterization of a laser-plasma soft-x-ray source at 13.5-nm wavelength with tin and its oxides," *J. Opt. Soc. Am. B*, **17**(9), 1616 (2000).
63. D. W. Myers, I. V. Fomenkov, B.A.M. Hansson, B. C. Klene, and D. C. Brandt, "EUV source system development update: advancing along the path to HVM," *Proceedings of SPIE, Emerging Lithographic Technologies IX*, **5751**(1), 248 (2005).
64. D.J.W. Klunder, M.M.J.W. van Herpen, V. Y. Banine, and K. Gielissen, "Debris mitigation and cleaning strategies for Sn-based sources for EUV lithography," *Proceedings of SPIE, Emerging Lithographic Technologies IX*, **5751**, 943 (2005).
65. M. C. Richardson, C.-S. Koay, C. Keyser, K. Takenoshita, E. Fujiwara, and M. M. Al-Rabban, "High-efficiency Tin-Based EUV Sources," *Proceedings of SPIE, Laser-Generated and Other Laboratory X-Ray and EUV Sources, Optics, and Applications*, **5196**, 119 (2004).
66. P.A.C. Jansson, B.A.M. Hansson, O. Hemberg, M. Otendal, A. Holmberg, J. de Groot, and H.M. Hertz, "Liquid-tin-jet laser-plasma extreme ultraviolet generation," *Appl. Phys. Lett.*, **84**(13), 2256 (2004).
67. M. Richardson, C.-S. Koay, K. Takenoshita, C. Keyser, S. George, S. Teerawattansook, M. Al-Rabban, H. Scott, "Laser plasma EUVL sources – progress and challenges," *Proceedings of SPIE. Emerging Lithographic Technologies VIII*, **5374** (1), 447 (2004).

68. T. Krücken, K. Bergmann, L. Juschkin, and R. Lebert, "Fundamentals and limits for the EUV emission of pinch plasma sources for EUV lithography," *J. Phys. D., Appl. Phys.*, **37**(23), 3213 (2004).
69. U. Stamm, "EUV source development at XTREME technologies – an update," *3rd International Symposium on EUVL*, 02 November 2004, Miyazaki, Japan.
70. G. D. Kubiak, L. J. Bernardez II, K. D. Krenz, and W. C. Sweatt, "Scale-up of a cluster jet laser plasma source for extreme ultraviolet lithography," *Proceedings of SPIE. Emerging Lithographic Technologies III*, **3676**, 669 (1999).
71. S. Miyamoto, S. Amano, T. Inoue, A. Shimoura, K. Kaku, P.-E. Nica, H. Kinugasa, and T. Mochizuki, "EUV source developments on laser-produced plasmas using Xe cryogenic target and Li new scheme target," *EUV Source Workshop*, 27 February 2005, San Jose, CA, http://www.sematech.org/meetings/archives.htm .
72. M. Padgett and L. Allen, "Light with a twist in its tail," *Contemp. Phys.*, **41**(5), 275 (2000).
73. J. Courtial, K. Dholakia, L. Allen, and M. Padgett, "Second-harmonic generation and the conservation of orbital angular momentum with high-order Laguerre-Gaussian modes," *Phys. Rev. A.*, **56**(5), 4193 (1997).
74. N. R. Heckenberg, R. McDuff, C. P. Smith, and A. G. White, "Generation of optical phase singularities by computer-generated holograms," *Opt. Lett.*, **17**(3), 221 (1992).
75. Hollow laser beams http://grad.physics.sunysb.edu/~meardley/hollow/ .

Distribution List for ANL-MCS-CPH-06/56

Internal:

J.P. Allain
J.N. Brooks
A. Foley
D. Gruen
A. Hassanein (10)
Z. Insepov
J. Jung
I. Konkashbaev
V. Morozov (5)
E. Lusk
J. Nolen
J. Norem
G. Pieper
A. Sattelburger
T. Sizyuk (5)
V. Sizyuk (5)
R. Stevens
MCS Files (2)
TIS Files

External:

DOE-SC (5)

ANL Libraries:

ANL-E

Main Library:

Lawrence Berkeley National Laboratory
Lawrence Livermore National Laboratory
Los Alamos National Laboratory
Naval National Laboratory
Sandia National Laboratory

External:

M. Al-Rabban, Physics Department, Qatar University, Doha, Qatar
R. Anderson, Sandia National Laboratory, Albuquerque, NM
V. Bakshi, SEMATECH Corp., Austin, TX
D. Bolshukhin, XTREME technologies GmbH, Jena, Germany
R. Bristol, Intel Corporation, Santa Clara, CA
G. Derra, Philips GmbH, Forschungslaboratorien, Aachen, Germany

A. Egbert, Laser Zentrum Hannover, Hannover, Germany

A. Endo, Extreme Ultraviolet Lithography System Development Association, Kanagawa, Japan

S. Ellwi, PowerLaser Limited, West Sussex, UK

B. Fay, Alcatel Vacuum Technology, Annecy, France

I. Fomenkov, Cymer, Inc., San Diego, CA

K. Gäbel, XTREME technologies GmbH, Jena, Germany

Y. Izawa, Institute of Laser Engineering, Osaka University, Suita, Osaka, Japan

C-S. Koay, University of Central Florida, Orlando, FL

T. Kawamura, Institute for Laser Technology, Osaka, Japan

R. Lebert, AIXUV GmbH, Aachen, Germany

K. Mann, Laser-Laboratorium Gottingen, Gottingen, Germany

P. Marczuk, Carl Zeiss Laser Optics GmbH, Oberkochen, Germany

M. McGeoch, PLEX LLC, Brookline, MA

K. Nishihara, Institute of Laser Engineering, Osaka University, Suita, Osaka, Japan

J. Pankert, Philips Extreme UV GmbH, Aachen, Germany

C. Rettig, Cymer, Inc., San Diego, CA

B. Rice, Technology Development, Intel Corp., Hillsboro, OR

M. Schuermann, JENOPTIK Mikrotechnik GmbH, Jena, Germany

U. Stamm, XTREME technology GmbH, Jena, Germany

K. Takenoshita, University of Central Florida, Orlando, FL

Y. Teramoto, EUVA, Gotenba, Shizuoka, Japan

I. Tralle, Institut Fizyki WSP, Rzeszow, Poland

Y. Watanabe, Canon Inc., Utsunomiya-city, Japan

Bibliothek, Max-Planck-Institute für Plasmaphysik, Germany

C.E.A. Library, Fontenay-aux-Roses, France

Librarian, Culham Laboratory, England

Thermonuclear Library, Japan Atomic Energy Research Institute, Japan

University of Wisconsin Library

Mathematics and Computer Science Division
Argonne National Laboratory
9700 South Cass Avenue, Bldg. 308
Argonne, IL 60439-4825

www.anl.gov

UChicago ▶ Argonne LLC

A U.S. Department of Energy laboratory managed by UChicago Argonne, LLC